Determining Analytical Potential Energy Functions of Diatomic Molecules by Direct Fitting

by

Yiye Huang

A thesis
presented to the University of Waterloo
in fulfilment of the
thesis requirement for the degree of
Master of Science
in
Chemistry

Waterloo, Ontario, Canada, 2001

I hereby declare that I am the sole author of this thesis.

This is a true copy of the thesis, including any required final revisions, as accepted by my examiners.

I understand that my thesis may be made electronically available to the public.

Abstract

The fully quantum mechanical "direct-potential-fit" (DPF) method has become increasingly widely used in the reduction of diatomic spectra. The central problem of this method is the representation of the potential energy and Born-Oppenheimer breakdown (BOB) correction functions. There are a number of problems associated with the existing method and potential forms. This thesis delineates these problems and finds solutions to some of them. In particular, it is shown that use of a different expansion variable and a new treatment of some of the expansions resolves most of the problems. These techniques have been successfully tested on the ground electronic states of the coinage metal hydrides and the Rb_2 molecule. To address the problem of representing "barrier" potential curves, a flexible new functional form, the "double-exponential long-range" (DELR) potential function, is introduced and applied to the $B\,^1\Pi_u$ barrier state of Li_2. In addition, the Λ-doubling level splitting which occurs for $^1\Pi$ electronic states has been taken into account by extending the effective Schrödinger equation. The computer program DSPotFit developed in our laboratory for performing DPF analyses has been extended to incorporate the ability to fit the analytical potential energy functions to tunneling predissociation line widths for quasibound levels. Finally, an attempt is made to investigate whether there exists a hump in the ground state rotationless potential curve of beryllium hydride.

Acknowledgements

The first person I wish to thank is my supervisor **Dr. Robert J. Le Roy**. Without his **patient** guidance, I wouldn't have made such progress during my two-year graduate work. More importantly, he has given me lots of constructive suggestions. He shared his time and information with people; we had many helpful discussions, especially in the Graduate House on Friday.

I must also thank **Dr. Frederick R. McCourt** who has been a great help to me. I was deeply impressed by his solid and profound knowledge of Chemistry and Mathematics theories. Attending his lectures is a pleasurable experience. Most importantly, from him I learned what a gentleman is.

I thank **Professor Peter Bernath** for his helpful discussion regarding the BeH molecule. Amazingly, this experimental spectroscopist seems to know quantum theory much better than many theoreticians.

I would also like to express my gratitude to **Jenning Seto**, **Douglas Weir**, **Dr. Carey Bissonnette** and **Dr. Hua Wei** who provided me with a lot of help in my research.

My parents actually played an important role in this work. They were the ones who encouraged me to pursue science in my early childhood. I wish express my deep gratitude to them.

Finally, I need to mention my wife, the one who cooks for me. Though she complained occasionally, she still cooked. I am very grateful for her support in these years.

Contents

List of Tables

List of Figures

Chapter 1

Introduction

Molecular spectra provide the most useful data for determining molecular structures and bond energies, and are a key means of verifying the presence of various elements or molecules and monitoring the concentrations of chemical species in laboratory, industrial, atmospheric and interstellar environments. The conventional method of analyzing diatomic molecule spectra consists of a two-step procedure in which the observed transition frequencies are first fitted to empirical expressions such as Dunham expansions for level energy differences, and these expressions are then used in the semiclassical Rydberg-Klein-Rees (RKR) method to determine the internuclear potential energy functions for the upper and lower states of the transition. However, this method has significant drawbacks. Firstly, of the relatively large numbers of empirical molecular constants required to represent the energy levels giving rise to the thousands of observed transitions, most have little physical significance. Secondly, the RKR potentials are approximate, and for many species they don't represent the data to quantum-mechanical accuracy. Thirdly, this approach breaks down for molecular states whose potential energy curves have an "irregular" shape, such as a "barrier", a "shelf" or a second minimum.

A more efficient and promising approach for extracting molecular information from spectra is the direct-potential-fit (DPF) procedure in which the observed data are compared to synthetic spectra generated quantum-mechanically from chosen analytical potential energy functions, and a

least-squares fitting procedure is used to optimize the parameters defining those potentials. This approach requires far fewer empirical parameters to represent data sets within the experimental uncertainties, and the potentials obtained in this way are quantum-mechanically exact. The DPF approach has been successfully applied to the reduction of diatomic spectra by a number of groups [11, 12, 13, 14, 15]. An important step of this method involves developing a well-behaved analytical potential model. To date, a variety of analytical potential function forms have been introduced and applied to particular molecular systems [8, 11, 12, 13, 14, 15]. In our group, a general-purpose computer program DSPotFit [16] for performing DPF analyses of arbitrarily large multi-isotopomer data sets has been developed and successfully applied to a number of systems which have conventional single-well potential energy curves [15, 17, 18]. In addition, some flexible Morse-type potential forms such as the "extended Morse Oscillator" (EMO) [17] and "Morse-Lennard-Jones" (MLJ) [8] potentials have been developed. However, there were a number of problems associated with the existing potential forms, with the extant DSPotFit computer program, and with the DPF method:

1. Although potentials determined by the DPF method tend to be more reliable in extrapolation than conventional RKR potentials, unphysical behaviour in one or both of the short-range or long-range regions occurs occasionally with the existing analytical potential functions.

2. The MLJ form does incorporate the theoretically-predicted asymptotic inverse-power behaviour, but only takes account of the leading long-range term. To have the correct limiting behaviour at long range, an *ad hoc* switching function has been required in practical application of the MLJ model; this is quite undesirable.

3. The existing version of the DSPotFit program could not take Λ-doubling effects into account, and was unable to fit to tunneling predissociation line widths for quasibound levels.

4. Tellinghuisen [19] treated the potential barrier of the $B\,0^+(^3\Pi)$ state of BrCl as arising from an avoided crossing between a Morse potential and an inverse-power repulsion term, with the resulting potential being defined by a diagonalization involving a 3-parameter off-diagonal

coupling function. This method uses a fit to three analytical functions to determine a single effective potential, thereby complicating the fitting process. No other analytical potential model has been proposed for describing states with rotationless potential energy barriers.

5. The Morse-type potentials could treat shelf states or double-minimum potentials, in principle. However, there is no successful case to date of representing these irregular potential energy functions using the existing models.

This thesis addresses a number of these problems. An important objective is to develop appropriate models for the potential energy and Born-Oppenheimer break-down (BOB) correction functions such that both will accurately represent the experimental data, and will extrapolate plausibly beyond the observed data regions in a way that avoids pathological behaviour. In particular, new versions of EMO and MLJ potential models are introduced to address the short-range and long-range extrapolation problems. These models are successfully applied to the ground electronic states of the coinage metal hydrides and the rubidium dimer. In addition, the $B\,^1\Pi_u$ state of Li_2 is of interest in this thesis, not only because it is a barrier state, but also because it is a prototype case involving both Λ-doubling splitting and tunneling predissociation data. A new potential form, the "double-exponential long-range" (DELR) model, is introduced to represent the barrier potential energy curve of the B-state of Li_2. The DELR potential can include multiple inverse-power contributions to a long-range potential, and even a repulsive electron exchange interaction term, when necessary.

In a measurement of the transitions to the levels above the asymptote (quasibound levels), the spectra obtained are broadened due to tunneling predissociation through the barrier. The ability to fit to the tunneling predissociation line widths of the quasibound levels when optimizing the potential energy functions has been incorporated into the computer program DSPotFit, and applied to the B-state of Li_2.

In addition to addressing a number of challenging and interesting problems in the practical analysis of spectroscopic data for particular molecules, the central objective of this work is to produce a well documented, robust and effective computational tool that can be freely distributed to experimentalists, to allow them to undertake such analyses on their own.

Chapter 2

Nature of The Problem

One of the most important objectives of spectroscopic data reduction is to represent the many hundreds or thousands of spectroscopic lines within the experimental uncertainties in a compact manner. There are two commonly-used methods to accomplish this goal. The first one is the conventional parameter-fit/RKR method, and the second one is the direct-potential-fit (DPF) approach. The present work contributes to the enhancement and further development of the latter method. This chapter begins with a brief discussion of the nature of the potential energy functions for diatomic molecules, and is followed by a description of the parameter-fit/RKR approach and its drawbacks. Finally, a discussion of the DPF method is given.

2.1 The Schrödinger Equation for Diatomic Molecules

A diatomic molecule can be regarded as a vibrating rotor in which the nuclei execute combined vibrational and rotational motions which are followed almost instantaneously by a "sea" of electrons, while the entire molecular system undergoes translational motion. After the motion of the centre-of-mass has been separated from the total diatomic Schrödinger equation, the nuclear motions remain coupled with the electron motions [20].

To further simplify the Schrödinger equation, three facts are taken into account:

1. The potential energy function is the same for different isotopomers in a given state of a molecule.

2. Nuclei move much slower than electrons, so the nuclei may be assumed to be frozen in a fixed configuration when treating the electronic motions. [1]

3. Electrons move so rapidly that the nuclei are assumed to experience a force that is an average over the electronic motions.

Based on these assumptions, with some coupling terms being neglected, the relative nuclear motions are separated from the electron motions, and the resulting rovibrational Schrödinger equation for $^1\Sigma$ states is written as

$$\left[-\frac{\hbar^2}{2\mu R^2}\frac{\partial}{\partial R}R^2\frac{\partial}{\partial R}+\frac{\hbar^2\hat{J}^2}{2\mu R^2}+V(R)\right]\Phi = E_{vJ}\,\Phi \quad , \tag{2.1}$$

in which $\hat{J}^2$ is the operator for the square of the rotational angular momentum, and $V(R)$ is the locus of values of the electronic energy $E_{el}(R)$ which acts as the potential energy for nuclear motions, and can be obtained by solving the Schrödinger equation for the electronic wave function ψ_{el},

$$\hat{H}_{el}\,\psi_{el} = E_{el}\,\psi_{el} \quad , \tag{2.2}$$

for different fixed internuclear distances R. This is the approximate Born-Oppenheimer separation of the electronic and nuclear motions [21]. Finally, because the angular and radial motions in a diatomic molecule are exactly separable, Eq. (2.1) can be simplified to yield the diatomic radial Schrödinger equation for $^1\Sigma$ states

$$\left[-\frac{\hbar^2}{2\mu}\frac{d^2}{dR^2}+\frac{\hbar^2 J(J+1)}{2\mu R^2}+V(R)\right]\psi_{vJ} = E_{vJ}\,\psi_{vJ} \quad , \tag{2.3}$$

where ψ_{vJ} is the rovibrational wave function.

[1] The nuclei are said to be "clamped".

At this stage, the central problem is how to determine the internuclear potential energy function $V(R)$. Once the potential energy function is known, the Schrödinger equation can be solved readily using a standard numerical method [7] to yield the eigenvalues and wave functions, which in turn are useful for predicting other molecular properties of interest. In principle, $V(R)$ (or E_{el}) may be obtained by solving the electronic Schrödinger equation Eq.(2.2). However, there is no simple analytical solution for $V(R)$, and the necessary computations are tedious. In practice, the potential energy functions $V(R)$ are usually obtained from the reduction of spectroscopic data. This is not only a way to test the results of *ab initio* calculations, but the potentials $V(R)$ obtained from accurate measurements are also more reliable.

The conventional method for constructing potential energy functions from spectroscopic data consists of two steps. The first step is to fit empirical expressions for the upper and lower level energies to the observed transition frequencies; the second step is to construct an RKR potential from those empirical expressions. A more direct approach is the DPF procedure, which involves fitting the observed spectroscopic data directly to the calculated energies generated from a chosen potential function by a least-squares fitting procedure [22]. The following sections describe and compare these approaches.

2.2 The Conventional Approach

2.2.1 The Empirical Parameter-Fitting/RKR Method

Parameter Fitting

The observed transition frequencies of diatomic molecules are usually represented by simple analytical functions of the vibrational and rotational quantum numbers v and J for the upper and lower vibration-rotation levels. The most commonly used empirical expressions for the level energies are "band-constant" expressions [23, 24]:

$$E^{\alpha}_{vJ} \quad = \quad G^{\alpha}_{v} + B^{\alpha}_{v}[J(J+1)] - D^{\alpha}_{v}[J(J+1)]^2 + H^{\alpha}_{v}[J(J+1)]^3 + \ldots$$

$$= \sum_{m=0} K_m^\alpha(v)[J(J+1)]^m \quad , \tag{2.4}$$

in which E_{vJ}^α is the vibration-rotation level energy for isotopomer-α, J is the rotational quantum number, v the vibrational quantum number, G_v^α the vibrational energy of isotopomer-α, B_v^α the inertial rotational constant, D_v^α, H_v^α, etc., the centrifugal distortion constants (CDC's), or Dunham expansions [23, 25]

$$E_{vJ}^\alpha = \sum_{l,m} Y_{l,m}^\alpha \, (v+\tfrac{1}{2})^l \, [J(J+1)]^m \quad , \tag{2.5}$$

where the $\{Y_{l,m}^\alpha\}$ are known as Dunham coefficients. By comparing Eqs.(2.4) and (2.5) and incorporating the simple first-order semiclassical mass-scaling relation [25]

$$Y_{l,m}^\alpha = Y_{l,m}^1 (\mu_1/\mu_\alpha)^{m+l/2} \quad , \tag{2.6}$$

the G_v^α and B_v^α expressions can be written as

$$G_v^\alpha = K_0^\alpha(v) = \sum_{l=1} Y_{l,0}^\alpha \, (v+\tfrac{1}{2})^l = \sum_{l=1} Y_{l,0}^1 \left(\frac{\mu_1}{\mu_\alpha}\right)^{l/2} (v+\tfrac{1}{2})^l \quad , \tag{2.7}$$

and

$$B_v^\alpha = K_1^\alpha(v) = \sum_{l=0} Y_{l,1}^\alpha \, (v+\tfrac{1}{2})^l = \sum_{l=0} Y_{l,1}^1 \left(\frac{\mu_1}{\mu_\alpha}\right)^{1+l/2} (v+\tfrac{1}{2})^l \quad , \tag{2.8}$$

where μ_α is the reduced mass of isotopomer-α, and the chosen reference isotopomer is given the label $\alpha = 1$. In these expressions, only the expansion coefficients $\{Y_{l,m}^1\}$ for the selected reference isotopomer-1 are independent parameters. The band constants or the Dunham parameters $\{Y_{l,m}^1\}$ are obtained by fitting the set of observed transition frequencies to the above expressions. Since the observables are linear functions of the expansion parameters, this is a simple linear least-squares fit which does not require iteration to achieve convergence [5].

For non-Σ singlet electronic states, the projection Λ of the electronic orbital angular momentum on the internuclear axis does not equal 0, and the $[J(J+1)]$ factor in Eqs.(2.4) and (2.5)

should be replaced by $[J(J+1)-\Omega^2]$ to take account of the coupling of the electronic and rotational angular momenta [21, 23, 26], where $\Omega = |\Lambda + \Sigma|$ is the projection of the total electronic angular momentum along the internuclear axis, in which Σ is the projection of the total electronic spin angular momentum onto the internuclear axis. For $\Omega \neq 0$, every rotational level splits into a doublet of e and f parity states. The associated splitting energy in the Dunham-type form is conventionally expressed as [27]

$$\delta E^{\alpha}_{\Lambda}(v,J) = \pm\frac{1}{2}\sum_{l,m} q^{\alpha}_{l,m}\,(v+\tfrac{1}{2})^l\,[J(J+1)-\Omega^2]^m \quad , \tag{2.9}$$

$$= \pm\frac{1}{2}\sum_{l,m} q^{1}_{l,m}\left(\frac{\mu_1}{\mu_\alpha}\right)^{m+l/2}(v+\tfrac{1}{2})^l\,[J(J+1)-\Omega^2]^m \quad , \tag{2.10}$$

where the + and − signs correspond to e and f parity levels, respectively. Again, only the parameters for isotopomer-1 are independent, with those for the other isotopomers being determined by the usual mass-scaling relation.

The semiclassical mass-scaling relation of Eq.(2.6) has been assumed to be exact in the above discussion. While this is a fairly good approximation, the mass-scaling relation is not completely valid, and it breaks down for small reduced-mass molecular systems, since this relation is derived from the assumptions that different isotopomers in a given state have exactly the same internuclear potential energy function, and that the first-order semiclassical quantization condition [2] is exact. With decreasing reduced mass, neither of these assumptions is valid. Theory has shown that the corrections to these assumptions are proportional to the inverse of the atomic masses $M_{\rm A}$ and $M_{\rm B}$ of the two atoms A and B [25, 29, 30, 31]. In the present work these two types of correction to the level energy expressions are collectively called "Born-Oppenheimer breakdown" (BOB) corrections. [3]

In a Dunham-type representation of the level energies, the BOB corrections may be written

[2] Derived from the first-order Wentzel-Kramers-Brillouin (WKB) approximation [28].

[3] Born-Oppenheimer breakdown effects are further discussed in section 3.2.

as [32]

$$\delta^{\alpha}_{\rm BOB}(v,J) \;=\; \sum_{l,m}\left\{\frac{\Delta M^{\alpha}_{\rm A}}{M^{\alpha}_{\rm A}}\delta^{\rm A}_{l,m}+\frac{\Delta M^{\alpha}_{\rm B}}{M^{\alpha}_{\rm B}}\delta^{\rm B}_{l,m}\right\}\left(\frac{\mu_1}{\mu_\alpha}\right)^{m+l/2}(v+\tfrac{1}{2})^l\,[J(J+1)-\Omega^2]^m \quad , \quad (2.11)$$

where $\Delta M^{\alpha}_{\rm A} = M^{\alpha}_{\rm A} - M^{1}_{\rm A}$ is the mass difference between isotope-α and isotope-1 of atom A, and the term $\delta^{\rm A}_{l,m}$ includes the corrections for both BOB and WKB breakdown effects for atom A. Combining all these correction terms, the overall Dunham expansion representation of the level energies is written as

$$E^{\alpha}_{vJ} = \sum_{l,m}\left\{Y^1_{l,m}+\frac{\Delta M^{\alpha}_{\rm A}}{M^{\alpha}_{\rm A}}\delta^{\rm A}_{l,m}+\frac{\Delta M^{\alpha}_{\rm B}}{M^{\alpha}_{\rm B}}\delta^{\rm B}_{l,m}\pm\frac{1}{2}q^1_{l,m}\right\}\left(\frac{\mu_1}{\mu_\alpha}\right)^{m+l/2}(v+\tfrac{1}{2})^l\,[J(J+1)-\Omega^2]^m \quad . \quad (2.12)$$

Note that for $^1\Sigma$ electronic states, $\Omega = 0$ and all of the $q^1_{l,m} = 0$.

The RKR Potential

With the expressions for the vibrational energy G_v and the inertial rotational constant B_v obtained from the empirical fits, the potential energy curves may be determined through the Rydberg-Klein-Rees (RKR) inversion procedure [6, 33, 34, 35], which is based on the first-order Wentzel-Kramers-Brillouin (WKB) approximation [28]. The RKR method begins with the approximate first-order semiclassical quantization condition

$$v+\frac{1}{2} = \left(\frac{\sqrt{2\mu/\hbar^2}}{\pi}\right)\int_{R_1}^{R_2} dR[E_{vJ}-V_J(R)]^{\frac{1}{2}} \quad , \quad (2.13)$$

where $R_1(v)$ and $R_2(v)$ are the inner and outer turning points defined by the requirement that $E_{vJ} = V_J(R_1(v)) = V_J(R_2(v))$, and $V_J(R)$ is the effective potential. For a rotating diatomic molecule, $V_J(R)$ is composed of two terms, a rotationless potential energy term, $V(R)$, plus a centrifugal potential term $J(J+1)\hbar^2/2\mu R^2$, i.e.,

$$V_J(R) \;=\; V(R)+\frac{J(J+1)\hbar^2}{2\mu R^2} \quad . \quad (2.14)$$

If v is treated as a continuous function of energy, then Eq.(2.13) may be differentiated with respect to E and $[J(J+1)]$, and the resulting equations inverted to yield [36]

$$R_1(v) - R_2(v) \;=\; 2\sqrt{\frac{\hbar^2}{2\mu}} \int_{v_0}^{v} \frac{dv'}{[G_v - G_{v'}]^{\frac{1}{2}}} \;\equiv\; 2f(v) \quad , \tag{2.15}$$

and

$$\frac{1}{R_1(v)} - \frac{1}{R_2(v)} \;=\; 2\sqrt{\frac{2\mu}{\hbar^2}} \int_{v_0}^{v} \frac{B_{v'}}{[G_v - G_{v'}]^{\frac{1}{2}}}\, dv' \;\equiv\; 2g(v) \quad , \tag{2.16}$$

where v_0 is the extrapolated value of the vibrational quantum number at the potential minimum, $B_v = \partial E(v,J)/\partial[J(J+1)]|_{J=0}$.

For any given smooth functions for G_v and B_v, the $f(v)$ and $g(v)$ integrals may be readily evaluated numerically. Rearrangement of Eqs.(2.15) and (2.16) then gives the desired potential function turning points:

$$R_1(v) \quad = \quad \sqrt{f^2 + f/g} - f \quad , \tag{2.17}$$

$$R_2(v) \quad = \quad \sqrt{f^2 + f/g} + f \quad . \tag{2.18}$$

2.2.2 Iterative Constrained-Parameter Fitting

In the empirical parameter-fitting/RKR method described above, the centrifugal distortion constants (CDC's) are often treated as independent parameters to be determined from the fit. When this is the case, the CDC's may not be consistent with the RKR potentials, since a knowledge of the vibrational energies G_v and inertial rotational constants B_v is sufficient to calculate the RKR potential function, which in turn can be used to calculate the CDC's. This means that the CDC's are not independent parameters. Unfortunately, the centrifugal distortion constants determined from empirical fits are often not consistent with those calculated from RKR potential functions. This would mean that the G_v and B_v functions used to generate the RKR potential will be slightly in error, since they are not "mechanically-consistent" with the CDC's combined with them to represent the data. On the other hand, inter-parameter correlation always accompanies a least-squares fit, which means that even with a good quality fit, the effect of neglecting high-order

CDC terms could be compensated for by the errors in lower-order constants. Thus, the G_v and B_v obtained from the fit may not be ideal, and the empirical CDC's may not be "true" values.

An iterative "constrained-parameter fitting" procedure can solve this problem. The RKR potential curve generated from preliminary G_v and B_v functions may be used in solving the Schrödinger equation and in the calculation of accurate CDC's [37]. Then, by holding the CDC's fixed at those calculated values, a new fit to experimental data gives improved G_v and B_v functions, and the resulting G_v and B_v values are then used to construct an improved RKR potential, which in turn yields further-improved CDC's. This iterative approach converges quite rapidly [37] to yield a self-consistent set of vibrational, rotational and centrifugal distortion constants. The iterative constrained-parameter fitting procedure yields much more physically meaningful values of higher-order CDC's than does the one-step parameter-fitting procedure. The results therefrom should be more reliable for extrapolation to high-J levels that lie beyond the range of available data, and are most sensitive to the higher-order CDC values. A schematic outline of this procedure is shown in Fig. 2.1.

A qualitative comparison of the molecular constants obtained from empirical parameter fitting and iterative constrained parameter fitting was performed for the $F\,^1\Sigma_g^+ \leftarrow A\,^1\Sigma_u^+$ electronic spectrum of Li_2, using data reported by Bernheim *et al.* [38] [4] and Antonova *et al.* [39] [5] for levels up to $v' = 30$. First of all, the Dunham expression of Eq. (2.5) was fitted to the observed transition frequencies using the computer program "Diatomic Singlet Parameter Fit" (DSParFit) [5] to obtain Dunham expansions for the vibrational energy G_v^{fit}, inertial rotational constant B_v^{fit}, and centrifugal distortion constants D_v^{fit}, H_v^{fit}, etc. The G_v^{fit} and B_v^{fit} functions were then used to construct an RKR potential curve [6], which in turn was used in program LEVEL [7] to generate accurate quantal centrifugal distortion constants, D_v^{calc}, H_v^{calc}, etc. Finally, those calculated CDC's were held fixed, and a new fit to the experimental data was performed to obtain improved Dunham expressions for the vibrational energy G_v^{calc} and the inertial rotational constant B_v^{calc}.

This iterative procedure achieved full convergence after 2 cycles. Fig. 2.2 compares the con-

[4] Experimental uncertainty of the observed data is $0.2\,cm^{-1}$.

[5] Experimental uncertainty of the observed data is $0.01\,cm^{-1}$.

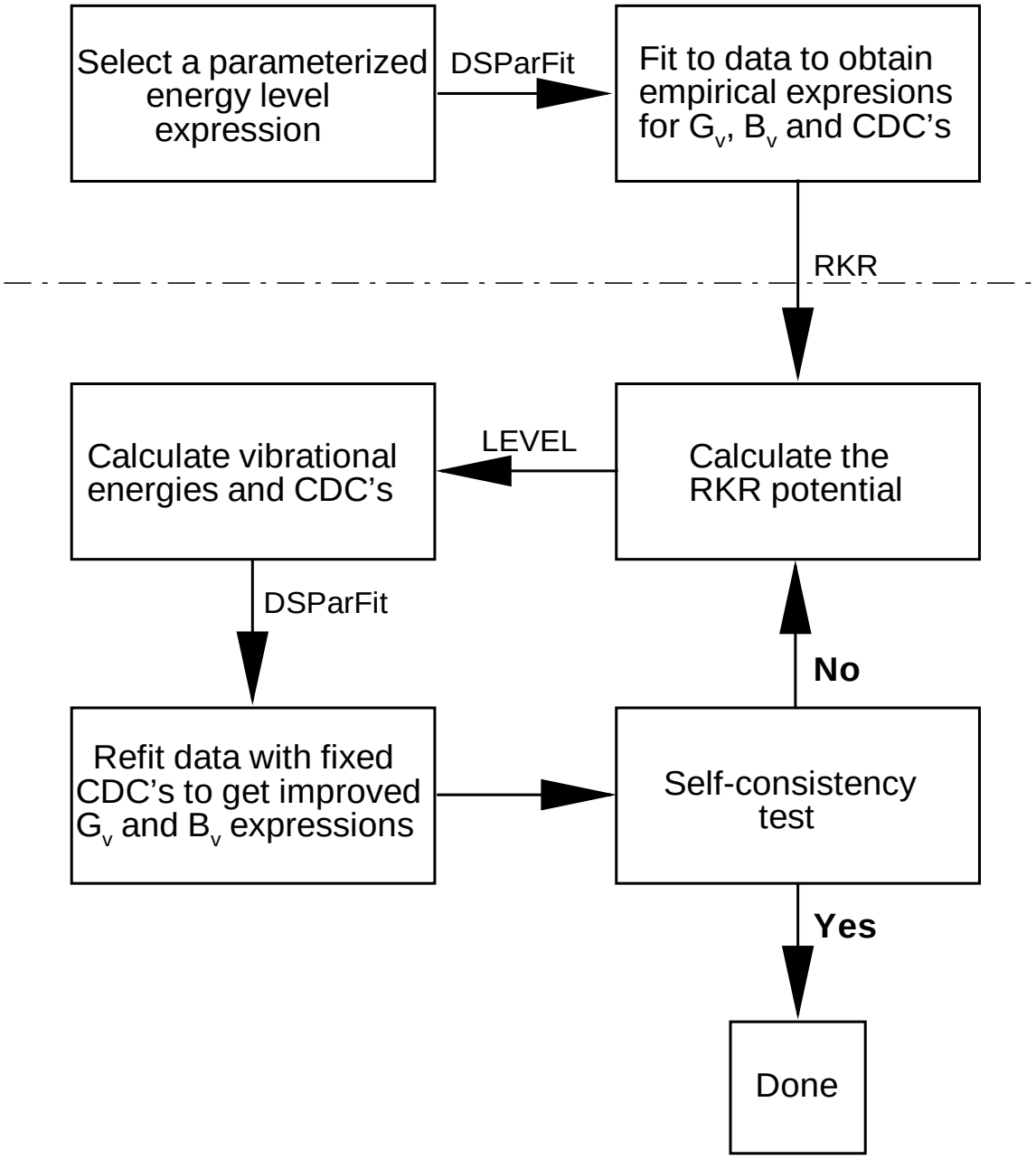

Figure 2.1: Outline of the iterative constrained-parameter fitting procedure. DSParFit [5], RKR [6] and LEVEL [7] are computer programs that, respectively, perform parameter fitting, determine potential energy curves by the RKR inversion procedure, and solve the radial Schrödinger equation.

tribution to the total energy of the highest observed J value ($J_{max} = 51$) for vibrational energies and rotational constants (G_v^{calc},B_v^{calc},D_v^{calc} and H_v^{calc}) calculated from the final RKR potential, to those (G_v^{fit},B_v^{fit},D_v^{fit} and H_v^{fit}) obtained from the initial empirical fit to the data for $F\,^1\Sigma_g^+$ state of Li_2. In these plots, the energy differences are scaled by the experimental uncertainty (Unc.) so that on any of these plots an ordinate value of (say) 5.4 means that this parameter discrepancy (e.g. $D_v^{calc} - D_v^{fit}$) would shift the $J = J_{max}$ level energy by 5.4 times the experimental uncertainty.

Figs. 2.2a and 2.2b show that the deviations between the values of G_v^{calc} and B_v^{calc} computed from the RKR potential, and the G_v^{fit} and B_v^{fit} values obtained from an empirical fit are quite large, especially for high-v levels. This illustrates the fact that the final RKR potential is not a very accurate representation of the true potential, since the quantal calculation using that potential does not exactly reproduce the molecular constants used as input to the RKR potential calculation. Figs. 2.2c and 2.2d indicate that the centrifugal distortion constants (D_v^{fit} and H_v^{fit}) obtained from the empirical fit are not consistent with D_v^{calc} and H_v^{calc} calculated from the RKR potential.

2.3 Problems with the Parameter-fit/RKR Method

As has been shown above, the parameter-fit/RKR method is not an ideal approach. Firstly, the RKR procedure is based on the first-order WKB approximation, which is accurate only for heavy molecules; thus, its inherent deficiencies are unacceptable in situations in which the first-order WKB condition is inadequate. This has been shown by Figs. 2.2a and 2.2b. Secondly, this method produces a pointwise potential which inherently does not contain any information about how to extrapolate beyond the experimental data regions. In addition, this method cannot be applied to molecular potential curves with an irregular shape such as a barrier, a shelf or a second minimum. In particular, the RKR method cannot construct an outer repulsive wall for the barrier, and thus this approach cannot properly account for the energy shifts of quasibound levels that undergo tunneling predissociation. Moreover, the numerical integration used to obtain the RKR potential

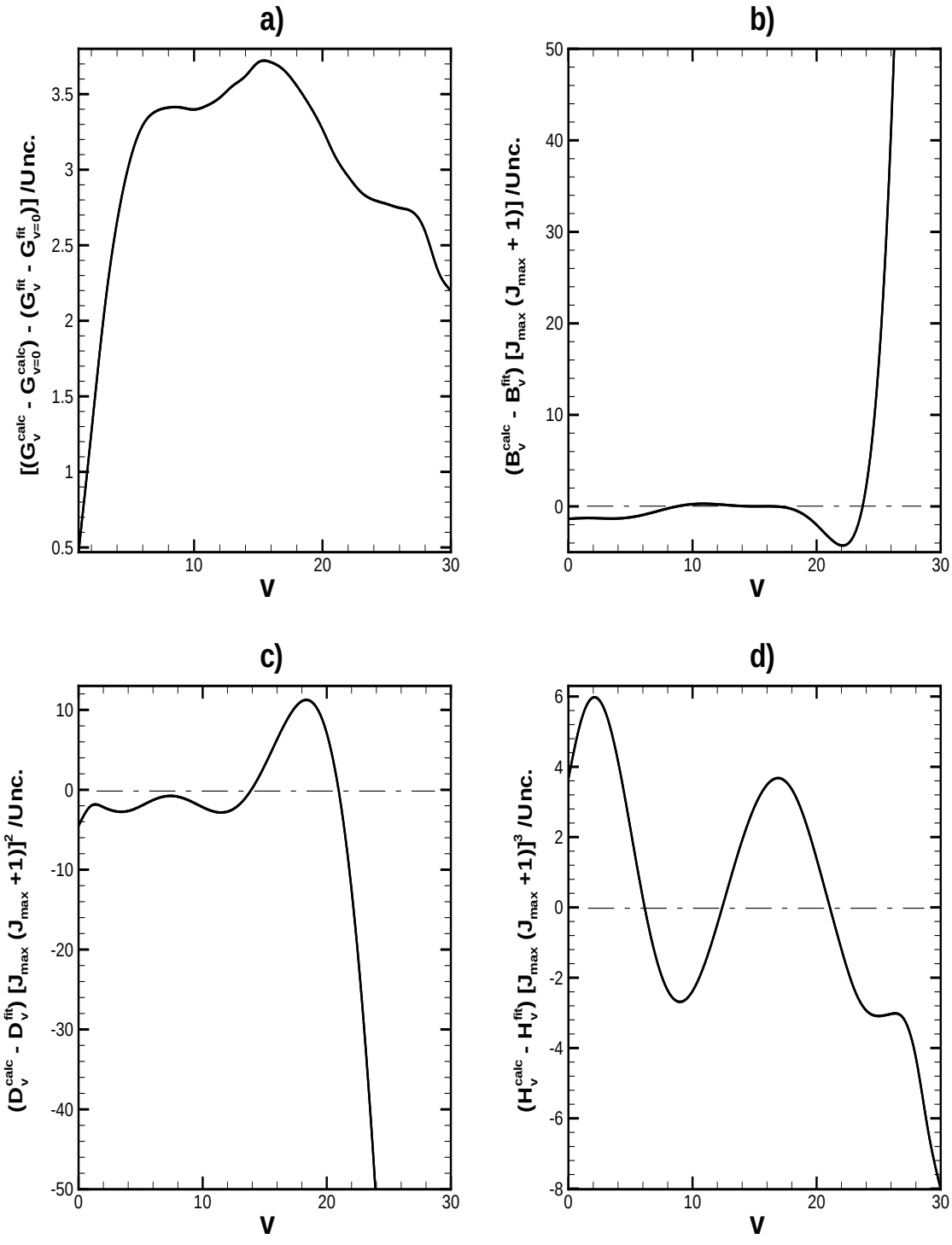

Figure 2.2: Differences between the values of G_v, B_v, D_v and H_v calculated from the RKR potential and those obtained from the empirical fit to the data for the $F\,^1\Sigma_g^+$ state of Li_2.

curve requires that G_v and B_v be mathematically smooth functions of v, while the discontinuities of the G_v and B_v functions due to the existence of a shelf or double minima in a potential curve may create computational problems. An example of such behaviour is shown in Fig. 2.3 using data reported by Antonova *et al.* [39]. Because of the shelf in the $F\,^1\Sigma_g^+$ state potential curve, G_v and B_v are not smooth monotonic functions of v, and the precise position of the "cusp" in the curve is difficult to determine to incorporate into the RKR integrals of Eqs. (2.15) and (2.16). For potential curves with double or multiple minima, there are more than two classical turning points at a given energy, while the RKR method assumes a simple two-turning-point potential.

Finally, the conventional approach cannot properly handle Born-Oppenheimer breakdown effects for light molecules with multiple isotopomers. It could treat different isotopomer as distinct chemical species; however, the correlation uncertainties make it very difficult, if not impossible, to determine BOB corrections. In the combined-isotopomer representation of the level energies by the empirical parameter fit, even though BOB correction terms $\delta^{\rm A}_{l,m}$ and $\delta^{\rm B}_{l,m}$ are incorporated, it includes corrections for both Born-Oppenheimer breakdown and breakdown of the first-order semi-classical quantization condition. This means that the correction is valid only in the observed data region and is not reliable for extrapolation because the BOB and WKB breakdown corrections are not independent terms in the expression. Moreover, the empirical parameter-fit/RKR approach cannot determine the "non-adiabatic" correction to the centrifugal potential. This further limits its utility.

2.4 The Direct-Potential-Fit (DPF) Approach

2.4.1 Overview of the DPF Method

In view of the limitations of the parameter-fit/RKR method, fully quantum mechanical direct-fitting approaches have become increasingly widely used in recent years [11, 12, 13, 14, 15]. Initial work of this type was done by Le Roy and van Kranendonk in 1974 [22]. They applied a direct-fit approach to atom-diatom Van der Waals systems, and obtained three-dimensional analytical potential energy surfaces for H_2- and D_2-inert gas complexes. In the following year, a direct-

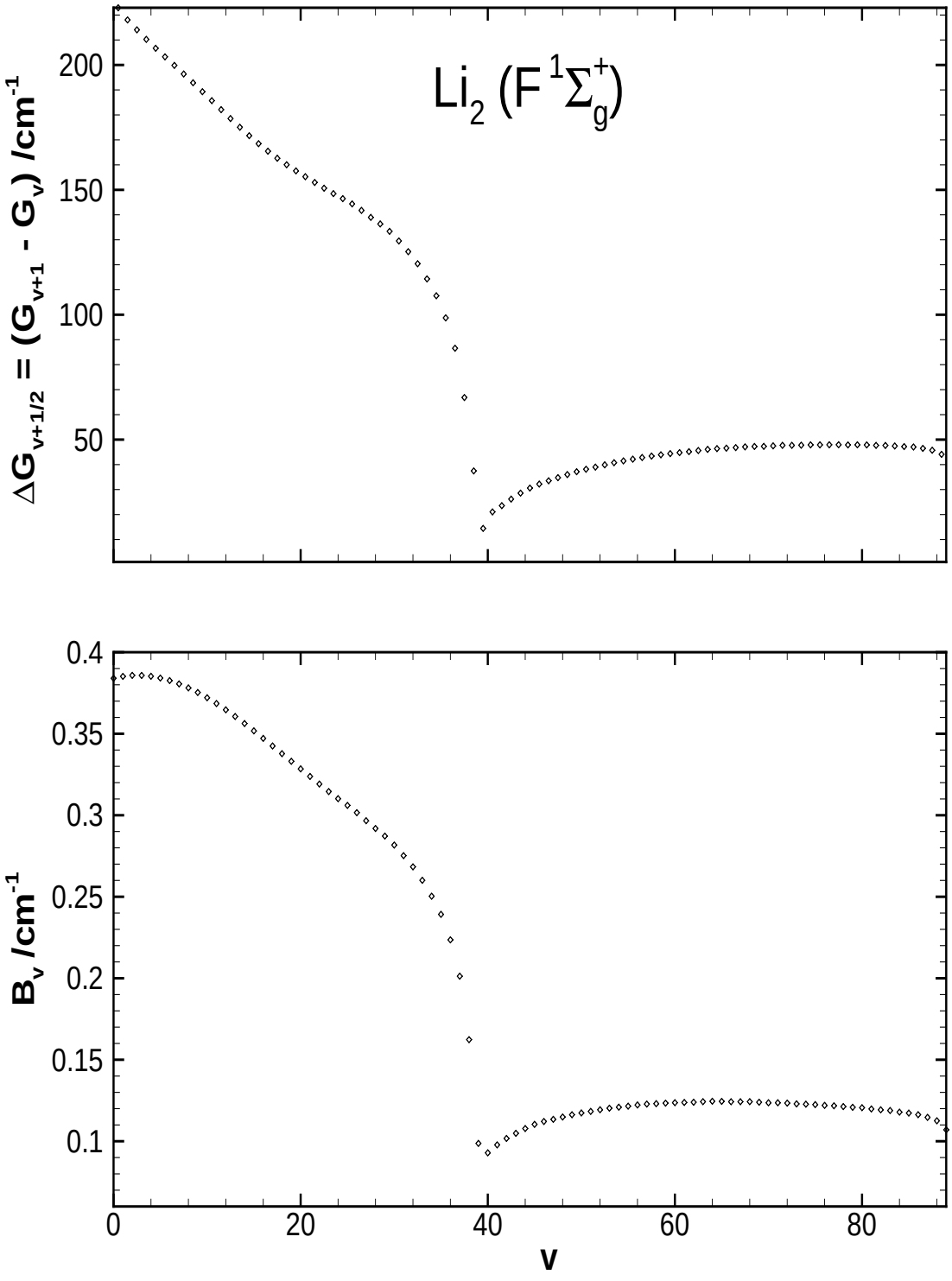

Figure 2.3: G_v and B_v functions of $F\,^1\Sigma_g^+$ state of Li_2.

fit approach was applied to diatomic molecules by Kosman and Hinze [40], who introduced an influential technique which they called Inverse Perturbation Analysis (IPA), to determine the potential energy functions for diatomic molecules. This method starts by choosing an approximate numerical potential function (RKR or *ab initio* points). The pointwise potential is optimized by finding the potential correction $\Delta V(R)$ which is expanded in terms of a set of suitable basis functions, such that the eigenvalue differences $\{E_{v',J'} - E_{v'',J''}\}$ obtained by solving the Schrödinger equation with potential $V(R) + \Delta V(R)$ agree with the experimental transition frequencies by a least-squares fitting procedure. The fitted parameters are the coefficients of the basis functions. The first practical application of this approach was by Vidal and Scheingraber [41], who used it to analyze the $A\,^1\Sigma_u^+ - X\,^1\Sigma_g^+$ band system of the Mg_2 molecule, and obtained a molecular potential and an extrapolated dissociation energy which were more accurate than those obtained from previous conventional analysis.

A strength of the IPA method lies in its model-free feature. It can treat any shape of potential energy curve without the limitation of any particular potential model. This method has seen further applications by a number of groups [2, 3, 42, 43] in recent years. In particular, Pashov *et al.* [44] developed a new IPA computer program based on the previous IPA method. To distinguish it from the original method, this modified IPA approach is denoted as "spline-pointwise IPA", and the original one as "polynomial-corrected IPA". The spline-pointwise IPA method also starts from an initial RKR potential, with the overall potential defined by a cubic spline function through those points. In the least-squares fit to the observed transition energies, the potential parameters are the energies of those potential points defining the spline functions. The possible unphysical behaviour of particular basis functions used in the polynomial-corrected IPA can be avoided by using this approach. The spline-pointwise IPA method has been applied to a number of molecular systems [2, 42, 45, 46, 47]. In particular, potential curves of the $F\,^1\Sigma_g^+$ shelf state and $B\,^1\Pi_u$ barrier state of the Li_2 dimer have been constructed by Pashov *et al.* [42] and Bouloufa *et al.* [2], respectively, using this approach.

The IPA approach described above focuses upon improving semiclassical pointwise RKR potential curves. Following the basic principle of IPA, Coxon made a breakthrough with this method

by also fitting to determine the adiabatic and non-adiabatic Born-Oppenheimer breakdown corrections for potential energy functions [48]. Coxon and Hajigeorgiou then adopted a model potential function based on a generalization of the familiar Morse oscillator [6] as the "clamped-nuclei" potential, [7] and included the adiabatic and non-adiabatic correction terms [8] explicitly in the Schrödinger equation[11]. They then fitted spectroscopic line positions for the $X\,^1\Sigma^+$ states of the isotopic HI and HBr molecular systems to the effective radial Hamiltonians by a least-squares fit procedure. Optimization is carried out on the parameters of the analytical potential functions, instead of the potential points themselves. The calculated eigenvalues of the Schrödinger equation reproduced observed line positions within the uncertainties of the experimental measurements. This was the first DPF treatment of diatomic molecules using a fully analytical potential function. The direct-potential-fit method using an analytical potential model and/or incorporating BOB correction functions is herein denoted as the "analytical DPF" approach.

Since that time, a number of groups have successfully performed analytical DPF analyses for a variety of diatomic molecules [12, 14, 49, 50]. The applications have focused on modifying the analytical forms of potential functions and the models of Born-Oppenheimer breakdown corrections. Dulick and Bernath and co-workers [13, 51, 52] introduced another Morse-type potential model, expressed the Born-Oppenheimer breakdown correction functions as a power series in $(R - R_e)$, and applied the DPF method to three molecular systems to obtain potentials which yield accurate predictions of line positions for high v and J levels. Šurkus [14, 53, 54] worked on the molecular ion ArH^+ using a flexible "generalized potential energy function", and also included adiabatic and non-adiabatic corrections which he expressed as expansions in powers of a flexible variable. [9] His results reproduced the spectra of ArH^+ within experimental accuracy, and incorporated a qualitatively correct long-range part of the diatomic potential curve.

A new type of analytical potential function, the "Morse-Lennard-Jones" (MLJ) function pro-

[6] A detailed description of this model is found in Chapter 3.

[7] The "clamped nuclei" version of the Born-Oppenheimer approximation assumes the nuclei are much more massive than electrons, and are regarded as fixed while the electrons move.

[8] Adiabatic and non-adiabatic correction terms correct the clamped-nuclei potential to take account of Born-Oppenheimer breakdown effects.

[9] This variable is discussed in Section 3.1.

posed by Hajigeorgiou and Le Roy [8] was adopted by Coxon and co-workers [55, 56] to study the $X\,^1\Sigma^+$ ground states of HeH^+ and BeH^+, and to determine potential functions with correct inverse-power long-range behavior. More recently, Seto and Le Roy applied the analytical DPF approach to the diatomic molecules GeO [17], CuH, AgH, AuH [15] and Rb_2 [10] using computer program DSPotFit [16] which allows for a variety of analytical potential functional models. The results yield much more reliable extrapolations to higher-J states than do analyses using the conventional RKR method.

2.4.2 The Nature of DPF Method

The DPF Procedure

The previous section has discussed three different DPF methods: polynomial-corrected IPA, spline-pointwise IPA and analytical DPF. The fundamental methodology of these approaches is essentially the same. The DPF approach is a single-step procedure which fits the observed transition frequencies directly to eigenvalue differences numerically generated from a Hamiltonian containing a parameterized potential energy function and/or other appropriate correction functions. It consists of the following steps:

1. Choose an initial trial potential function for the specific molecular system.
2. Calculate the transition frequencies $\nu(i) = E_{v'J'} - E_{v''J''}$ by solving the Schrödinger equation to determine the eigenvalues $E_{v'J'}$ and $E_{v''J''}$ of the upper and lower states of the transitions.
3. Compare the calculated frequencies with the observed spectra, and adjust parameters defining the corrected potential energy function by a least-squares fit procedure.
4. Go to step 3, and iterate until convergence is achieved.

A flowchart overview of the DPF method is given in Fig. 2.4. The heart of DPF method lies in the least-squares fitting procedure which is briefly discussed below.

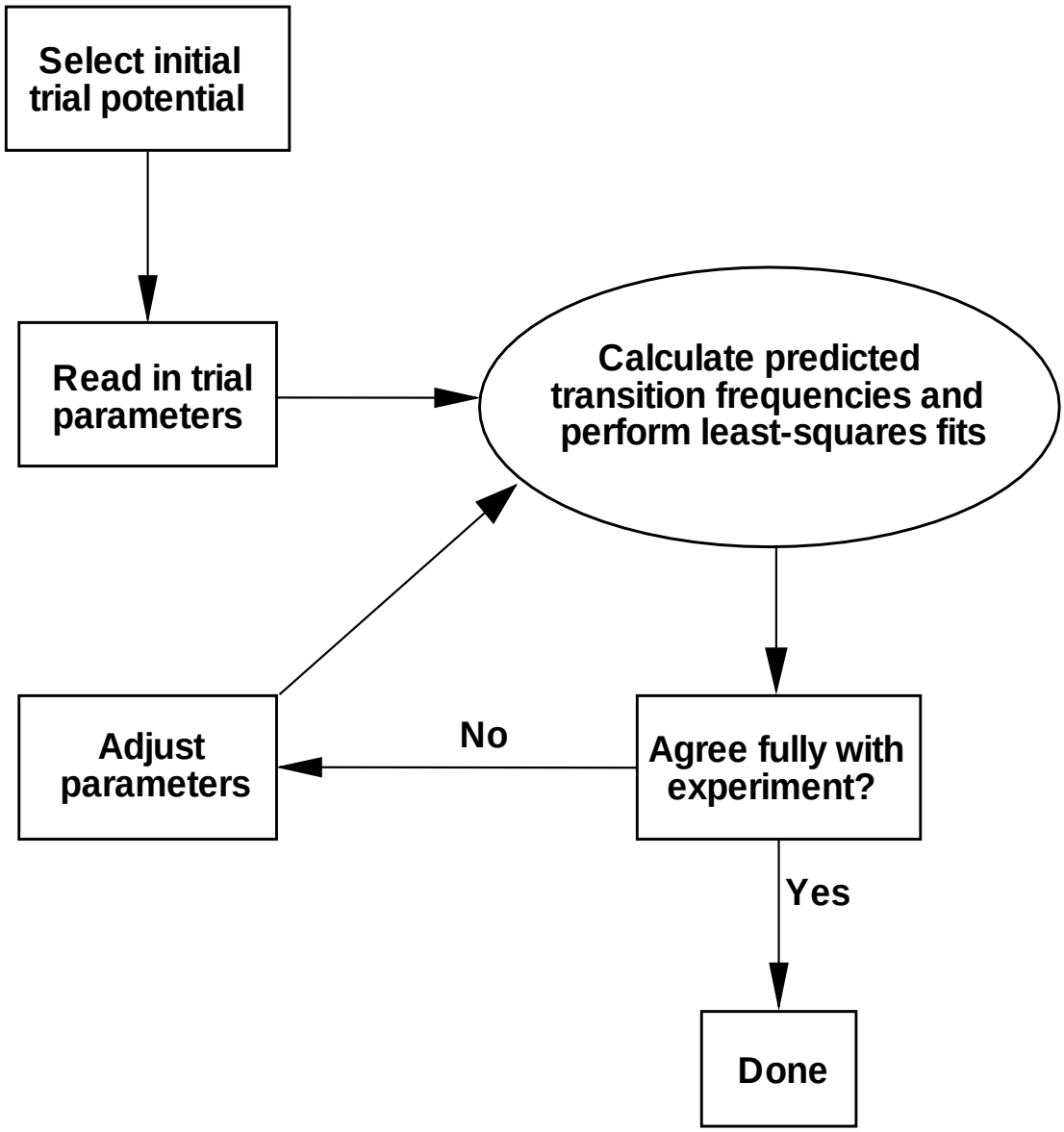

Figure 2.4: Schematic outline of the direct-potential-fit (DPF) procedure.

Non-Linear Least-Squares Fitting

Since the eigenvalues calculated from the Schrödinger equation are not linearly dependent on the parameters of the potential functions, a non-linear least-squares fitting procedure [22] has to be applied to find the optimal potential parameters. It involves an iterative approach that requires solving the Schrödinger equation with the chosen potential function, then fitting the observed frequencies to the calculated eigenvalue differences.

The "dimensionless sum of squares of deviations" (DSSD) between the observed and calculated values can be written as:

$$\text{DSSD} \;=\; \sum_{i=1}^{N} \left[\frac{\nu_o(i) - \nu_c(i)}{u_i} \right]^2 \quad , \tag{2.19}$$

with $\nu_o(i)$ representing the observed frequency, $\nu_c(i)$ representing the calculated frequency, N being the number of experimental data, and u_i the experimental uncertainty. The optimization is carried out by minimizing the DSSD to obtain a better fit. To achieve this goal, its partial derivatives with respect to each potential parameter are set to zero simultaneously, to yield the set of coupled linear inhomogeneous equations [22]

$$\sum_{i=1}^{N} \left[\nu_o(i) - \nu_c(i)\right] \frac{\partial \nu_c(i)}{\partial p_k} \frac{1}{{u_i}^2} \;=\; \sum_{j=1}^{M} \Delta p_j \left(\sum_{i=1}^{N} \frac{\partial \nu_c(i)}{\partial p_j} \frac{\partial \nu_c(i)}{\partial p_k} \frac{1}{{u_i}^2} \right) \tag{2.20}$$

for $k = 1$ to M, where M is the number of potential parameters, p_j and p_k are particular potential parameters, and $\{\Delta p_j\}$ are the desired corrections to the initial trial parameters. For non-linear least-squares fitting, a set of initial trial parameters $\{p_j\}$ has to be found in order to calculate the observables and their partial derivatives. The calculation of the partial derivatives $\frac{\partial \nu_c(i)}{\partial p_j}$ is straightforward, since the transition frequencies $\nu(i)$ are just the differences between the upper and lower state eigenvalues $\{E_{v'J'} - E_{v''J''}\}$, and the partial derivatives of the eigenvalues can be evaluated by the Hellmann-Feynman theorem,

$$\frac{\partial E_{v,J}}{\partial p_j} = \langle \psi_{vJ} \left| \frac{\partial V_J(R)}{\partial p_j} \right| \psi_{vJ} \rangle \quad . \tag{2.21}$$

The wave function for a particular state has been generated by solving the Schrödinger equation,

and the partial derivatives of $V_J(R)$ with respect to p_j can be calculated analytically. Solving the set of equations Eq. (2.20) will yield estimates of the changes $\{\Delta p_j\}$ in the parameters. The parameters are then updated $p_j(new) = p_j(trial) + \Delta p_j$, and the procedure is repeated.

2.4.3 The Analytical DPF Approach

The common steps of the three DPF methods have been discussed above. In particular, this thesis contributes to further development of the analytical DPF approach. Some specific details regarding this method are described below.

Choice of Analytical Potential Energy Function Models

The first step in the analytical DPF method is to select an appropriate analytical potential functional form. Different analytical potential function models exhibit different behaviour in fitting to experimental data. Which form is chosen depends on the specific molecular system being studied. The chosen potential function is required to reproduce the observed spectroscopic data within the experimental uncertainties, and to be robust enough to extrapolate reasonably beyond the range of available experimental data. Various analytical potential function models and their advantages and disadvantages are described in Chapter 3.

Determination of Trial Parameters

After selection of an analytical potential form, the next step is to determine the initial trial parameters for the analytical potential function. This is also one of the most important steps of the DPF approach, since the efficiency of non-linear least-squares fitting heavily depends on having a realistic set of trial parameters. The simplest way to obtain the set of trial potential parameters is to fit a preliminary RKR or *ab initio* potential to the chosen potential model. These fitted values roughly define the shape of the potential curve, and thus are fairly good parameters to start with. In practice, one can freeze most of the trial parameters obtained in the above manner and optimize one or more of them at each round of fit, then gradually free more parameters in subsequent fits. Some small programs to determine the trial parameters in this manner have been

written; they are separated from the main data-fitting program DSPotFit.

An alternative way to estimate the initial trial potential parameters utilizes the Dunham theory [21, 25, 29]. Dunham obtained the analytical level energy expression Eq.(2.5) by applying the semiclassical quantization condition Eq.(2.13) with the Dunham potential

$$V(\xi) = a_0\xi^2(1 + a_1\xi + a_2\xi^2 + \ldots) \quad , \tag{2.22}$$

in which $\xi = \frac{(R-R_e)}{R_e}$. Then he related the parameters $\{Y_{l,m}\}$ to the potential energy coefficients $\{a_i\}$ and the conventional spectroscopic constants. In particular, neglecting second-order terms in B_e^2/ω_e^2, the following relations are obtained:

$$Y_{0,1} = B_e = \frac{\hbar^2}{2\mu R_e^2} \, , \tag{2.23}$$

$$Y_{1,0} = \omega_e = \sqrt{4B_e a_0} \, , \tag{2.24}$$

$$Y_{1,1} = -\alpha_e = \frac{6B_e^2}{\omega_e}(1 + a_1) \, , \tag{2.25}$$

$$Y_{2,0} = -\omega_e x_e = \frac{3B_e}{2}\left(a_2 - \frac{5a_1^2}{4}\right) \, . \tag{2.26}$$

The potential coefficients $\{a_i\}$ are related to the partial derivatives of the Dunham potential function evaluated at $\xi = 0$. Rearranging the above equations yields

$$a_0 = \frac{\omega_e^2}{4B_e} = \frac{Y_{1,0}^2}{4Y_{0,1}} = \frac{1}{2}\left.\frac{d^2V}{d\xi^2}\right|_{\xi=0} = \frac{R_e^2}{2}\left.\frac{d^2V}{dR^2}\right|_{R=R_e} \, , \tag{2.27}$$

$$a_1 = -\left[\frac{\alpha_e\omega_e}{6B_e^2} + 1\right] = -\left[\frac{Y_{1,1}Y_{1,0}}{6Y_{0,1}^2} + 1\right] = \frac{R_e}{3}\left.\frac{d^3V}{dR^3}\right|_{R=R_e} \Big/ \left.\frac{d^2V}{dR^2}\right|_{R=R_e} \, , \tag{2.28}$$

$$a_2 = \frac{5}{4}a_1^2 - \frac{2\omega_e x_e}{3B_e} = \frac{5}{4}a_1^2 - \frac{2Y_{2,0}}{3Y_{0,1}} = \frac{R_e^2}{12}\left.\frac{d^4V}{dR^4}\right|_{R=R_e} \Big/ \left.\frac{d^2V}{dR^2}\right|_{R=R_e} \, . \tag{2.29}$$

If the Dunham potential functions $V(R)$ in the above equations are replaced by the chosen analytical potential models and the partial derivatives are evaluated at $R = R_e$, the first three leading trial potential parameters can be calculated from the values of $\{Y_{l,m}\}$ using these equations. This method of estimating the trial parameters has been automated in DSPotFit [9]. Determining the

first few leading trial potential parameters is the most important step. With them known, one can determine the high-order parameters using a "bootstrapping" method; i.e., by freeing additional higher-power parameter (initialized as zero), one at a time, and re-fitting to the experimental data to optimize this expanded parameter set. In this manner, one can optimize the parameter values and find the optimal number of potential parameters needed.

2.5 Fitting to Tunneling Predissociation Line Widths

The direct-potential-fit approach described above focuses on fitting the potential energy function to the transition frequencies. In fact, the DPF method can also fit to any other observables which depend upon the potential energy function. For an electronic state with a rotationless potential barrier or a centrifugal barrier [10] which protrudes above the asymptote at distances larger than the potential minimum, the molecule may predissociate by tunneling through the potential barrier, which causes a broadening of the observed lines and energy shifts of those quasibound levels. As the tunneling predissociation line widths are also observables and dependent upon the potential energy function, these observed line width data can be fitted together with the transition frequencies to determine the analytical potential energy functions, which can further improve the accuracy of the potential energy and the prediction of line widths.

Semiclassically, the predissociation lifetime τ of a quasibound state can be defined in first order as [57]

$$\tau \;=\; \frac{t_{vib}}{\omega} \quad .$$

In this expression, t_{vib} is the oscillation period of the particle in the potential well, and can be defined as

$$t_{vib} \;=\; 2\int_{R_1}^{R_2} \frac{dR}{v} \;=\; 2\int_{R_1}^{R_2} \frac{dR}{p/\mu} \;=\; (2\mu)\int_{R_1}^{R_2} \frac{dR}{[E - V_J(R)]^{1/2}} \quad , \tag{2.30}$$

[10] Centrifugally-distorted potentials for $J > 0$ always have a barrier (except for ion pair states).

in which R_1 and R_2 are the first and second classical turning points at energy E. The frequency ω represents the probability per collision of tunneling through the barrier: within a simple first-order semiclassical treatment of tunneling, it is given by [28]

$$\omega \;=\; \exp\left\{-\frac{(8\mu)^{1/2}}{\hbar}\int_{R_2}^{R_3}[V_J(R)-E]^{1/2}\,dR\right\} \quad , \tag{2.31}$$

in which R_2 and R_3 are the second and third classical turning points at energy E. The level width (FWHM) is then defined via the Heisenberg uncertainty principle as

$$\Gamma(\omega, t_{vib}) \;=\; \frac{\hbar}{\tau} \;=\; \frac{\hbar\omega}{t_{vib}} \quad . \tag{2.32}$$

Higher-order treatments of widths can be found in Refs. [7, 57, 58, 59]. The procedure of fitting the width data to the potential function is almost identical to that of fitting transition energies to potential models, as described in section 2.4.2, except that in addition to calculating the eigenvalues and their partial derivatives with respect to the various potential parameters, level widths and their partial derivatives need to be evaluated too. In the present thesis, level widths are calculated by subroutine SCHRQ of program LEVEL [7] using the higher-order methods discussed in Ref. [58]. The partial derivatives of the level widths and the integration techniques for evaluating these integrals are described in Appendix B.

2.6 The "Diatomic Singlet Potential Fit" Computer Program

A computer program "Diatomic Singlet Potential Fit" (DSPotFit) [16] has been developed in our group to implement the analytical DPF procedure. DSPotFit can perform least-squares fits of diatomic spectroscopic data to potential energy functions for multiple isotopomers and multiple electronic states simultaneously, and can take account of Born-Oppenheimer breakdown effects. In the present work, it was extended to take account of Λ-doubling splitting and to fit potential energy functions to the tunneling predissociation line widths for quasibound levels. In all the

least-squares fits in this work, the quality of fit is measured by the dimensionless Root Mean Square Residual (RMSR)

$$\text{RMSR} = \left\{ \frac{1}{N} \sum_{i=1}^{N} \left[\frac{Y_{calc}(i) - Y_{obs}(i)}{u_i} \right]^2 \right\}^{1/2} , \tag{2.33}$$

with $Y_{obs}(i)$ representing the observed value, $Y_{calc}(i)$ representing the calculated value, and N and u_i being defined as above. To run the program, a user will need to specify his/her chosen potential forms [11] and initial trial parameters to define the potential function. Determination of some of the initial trial parameters is partially automated in the program. The least-squares fits of the observables to the calculated values is controlled by subroutine NLLSSRR [5] in which an embedded subroutine is used to calculate the required eigenvalues/level widths and their partial derivatives. To demonstrate the use of the DPF approach, this program was applied to transition frequencies and tunneling predissociation line widths involving levels of three isotopomers of the $B\,^1\Pi_u$ state of Li_2, [12] and to the multiple-isotopomer spectroscopic data of the ground $X\,^2\Sigma^+$ state of BeH. [13]

[11] See Chapter 3.

[12] See Chapter 4.

[13] See Chapter 5.

Chapter 3

Representation of the Potential Energy and BOB Functions

3.1 Analytical Potential Energy Function Models

A very general form to express potential energy functions is the Dunham potential [25], which is a Taylor series expansion about the equilibrium internuclear distance R_e, namely

$$V(\xi) = a_0\xi^2(1 + a_1\xi + a_2\xi^2 + \ldots) \quad , \tag{3.1}$$

in which $\xi = \xi_{\rm D} = \frac{(R-R_e)}{R_e}$. The historic Dunham vibration-rotation energy expansions of Eq. (2.5) were derived from the above potential [25, 29]. However, the Dunham potential will always diverge at large R, while any potential energy function for a real diatomic molecule should approach a finite asymptote as $R \to \infty$. In order to avoid this singularity problem, Simons, Parr and Finlan [60] introduced the expansion variable $\xi_{\rm SPF} = \frac{(R-R_e)}{R}$ which approaches unity as $R \to \infty$, and Thakkar [61] then suggested the more general form:

$$\xi_{\rm T} = s(p)\left[1 - \left(\frac{R_e}{R}\right)^p\right] \quad , \tag{3.2}$$

where p is non-zero real number, and $s(p) = 1$ if $p > 0$, and $s(p) = -1$ if $p < 0$. Thakkar's radial expansion variable $\xi_{\rm T}$ becomes $\xi_{\rm D}$ when $p = -1$ and becomes $\xi_{\rm SPF}$ when $p = 1$. Unfortunately, while $\xi_{\rm SPF}$ and $\xi_{\rm T}$ approach unity as $R \to \infty$, both become singular as $R \to 0$. To ensure a finite domain for the expansion variable, Ogilvie [62] used the variable $\xi_{\rm OT} = 2(R - R_e)/(R + R_e)$. Later Šurkus [53] summarized these forms and suggested a generalized variable:

$$\xi_{\rm S} = s(p) \left(\frac{R^p - {R_e}^p}{R^p + n\,{R_e}^p} \right) \quad , \tag{3.3}$$

where n and p are real numbers. The Dunham, Simons-Parr-Finlan, Thakkar and Ogilvie variables are particular cases of the Šurkus variable for different combinations of $s(p)$, n and p values. The Dunham potential of Eq.(3.1) expanded in terms of any one of the later variables approaches a finite limit as $R \to \infty$; however, that potential will not necessarily have the correct dissociation energy $\mathfrak{D}_e$ at its asymptote.

Other frequently used potential models are Morse-type potential functions. The simplest of them is the well-known "simple Morse oscillator" (SMO) [63], which has the typical single-minimum well shape associated with regular potential curves, such as that for the ground $X\,^1\Sigma_g^+$ state of Li_2. The SMO potential is expressed as

$$V_{\rm SMO}(R) = \mathfrak{D}_e \left[1 - e^{-\beta_{\rm M}(R - R_e)} \right]^2 \quad , \tag{3.4}$$

where $\mathfrak{D}_e$ is the potential well depth, $\beta_{\rm M}$ is a constant, and R_e is the internuclear equilibrium distance. Obviously, the potential asymptote of SMO lies at the exact $\mathfrak{D}_e$. However, its simplicity with only three free parameters means that it cannot be accurate for states with a large number of observed levels.

3.1.1 The Generalized Morse Oscillator

An improvement to the SMO model was introduced by Coxon and Hajigeorgiou [11]; they replaced the constant exponential parameter $\beta_{\rm M}$ by a function $\beta_{\rm GMO}(R)$, which they expressed as a power

series in R. This yields the so-called "generalized Morse oscillator" (GMO) function,

$$V_{\rm GMO}(R) = \mathfrak{D}_e \left[1 - e^{-\beta_{\rm GMO}(R)\,(R-R_e)}\right]^2 \quad , \tag{3.5}$$

with

$$\beta_{\rm GMO}(R) = \beta_0^{\rm GMO} + \beta_1^{\rm GMO}(R-R_e) + \beta_2^{\rm GMO}(R-R_e)^2 + \ldots \quad , \tag{3.6}$$

in which $\beta_i^{\rm GMO}$ are constants. The GMO is much more flexible than the SMO and is able to represent experimental data with extremely high accuracy over a wide range of levels. It has been shown to represent successfully the lower part of the potential curves for a number of molecular systems [11, 49, 64]. However, since $\beta_{\rm GMO}(R)$ is a simple power series in R, the potential $V(R)$ diverges when R becomes infinite if the highest order coefficient of the $\beta_{\rm GMO}(R)$ expansion happens to be negative. The bottom part of Fig. 3.1 shows the GMO potential determined in Ref [11] for the ground electronic state potential curve of the HI molecule. At distances beyond the data region their $\beta_{\rm GMO}(R)$ function begins to decrease sharply, passes through zero just beyond 4 Å, and then continues to decrease toward $-\infty$. This causes the pathological behaviour seen for this potential curve in the extrapolated region.

3.1.2 The Modified Morse Oscillator

To address the long-range singularity problem, Dulick and Bernath and co-workers [13, 51, 52] introduced the "modified Morse oscillator" (MMO) potential function model,

$$V_{\rm MMO}(R) = \mathfrak{D}_e \left[1 - e^{-\beta_{\rm MMO}(z)\,z}\right]^2 / \left[1 - e^{-\beta_{\rm MMO}^{\infty}}\right]^2 \quad , \tag{3.7}$$

in which z is one-half the Ogilvie-Tipping variable [62] $\xi_{\rm OT}$,

$$z = \frac{1}{2}\xi_{\rm OT} = (R-R_e)/(R+R_e) \quad , \tag{3.8}$$

and

$$\beta_{\rm MMO}(z) = \beta_0^{\rm MMO} + \beta_1^{\rm MMO} z + \beta_2^{\rm MMO} z^2 + \ldots \quad , \tag{3.9}$$

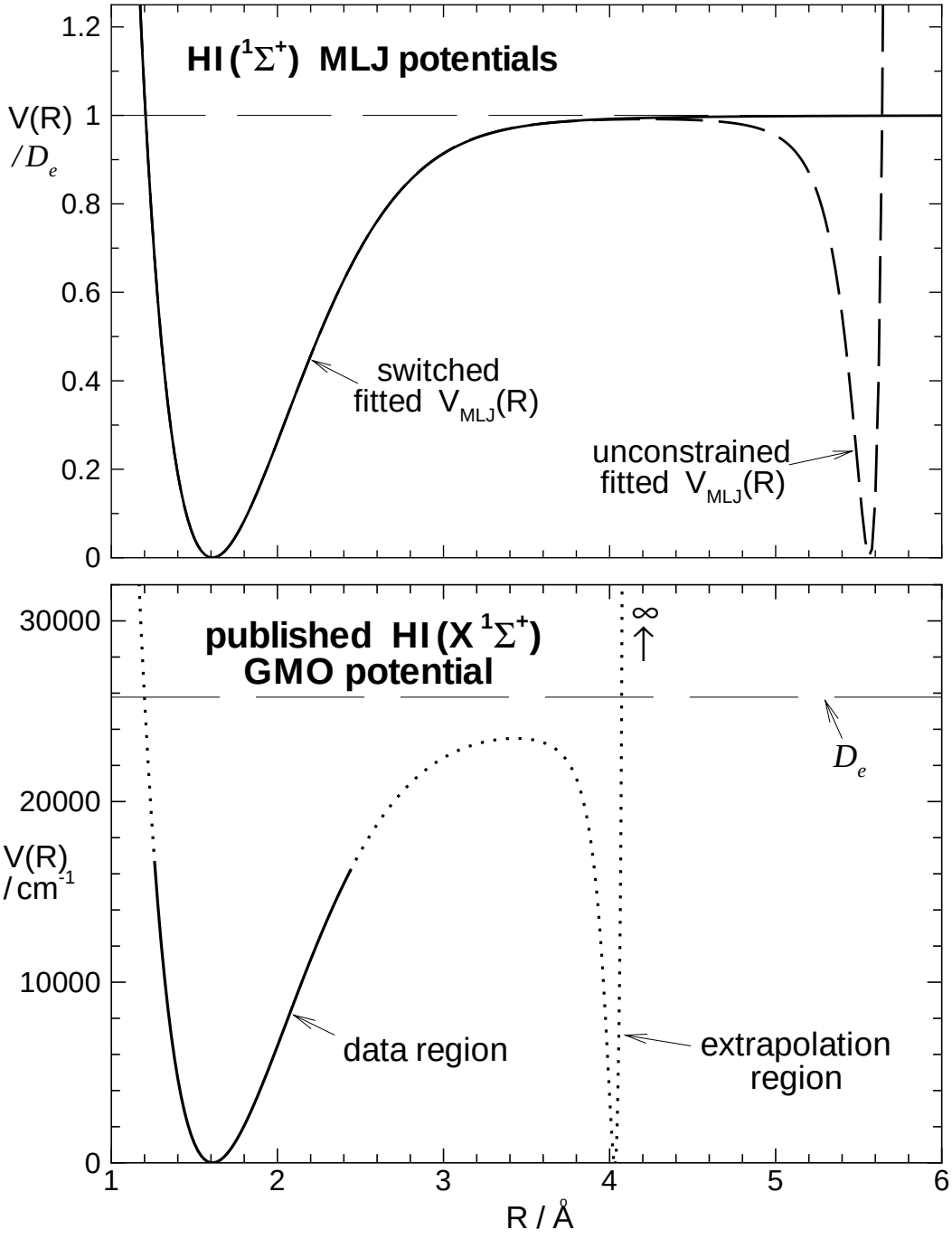

Figure 3.1: Ground state potential curve of HI obtained using GMO and MLJ models respectively. Adapted from Fig. 2 of Ref. [8].

with

$$\beta_{\rm MMO}^{\infty} \equiv \beta_{\rm MMO}(R=\infty) = \beta_{\rm MMO}(z=1) = \sum_{i=0} \beta_i^{\rm MMO} \quad . \tag{3.10}$$

The fact that the distance variable z is restricted to the range $[-1,1]$ for $R \in [0,\infty)$ prevents the MMO model from being singular at long range, and the inclusion of the factor $[1-e^{-\beta_{\rm MMO}^{\infty}}]^2$ in the denominator make the potential asymptote lie precisely at $\mathfrak{D}_e$. However, sign changes by $\beta_{\rm MMO}(z)$ in the extrapolation region at large or small R can still give rise to unphysical behaviour.

3.1.3 The Extended Morse Oscillator

An alternative model to the MMO function is the "extended Morse oscillator" (EMO) potential proposed by Le Roy and co-workers [15, 17]. This potential form does not require a normalization factor in the denominator, and is given by,

$$V_{\rm EMO}(R) = \mathfrak{D}_e \left[1 - e^{-\beta_{\rm EMO}(z)\,(R-R_e)}\right]^2 \quad , \tag{3.11}$$

where z is defined as above, and $\beta_{\rm EMO}(z)$ is a power series with the same form as $\beta_{\rm MMO}(z)$. The functional form of $V_{\rm EMO}(R)$ is simpler than that of $V_{\rm MMO}(R)$ and tends to be well-behaved over the entire region of R as long as $\beta_{\rm EMO}(z)$ does not decrease too rapidly or become negative at large or small distances.

3.1.4 The Morse-Lennard-Jones Oscillator

One deficiency of all of the above-mentioned Morse-type potential models is that they fail to incorporate the theoretically-predicted attractive inverse-power asymptotic behavior of most diatomic potentials. It has been shown that if two atoms lie sufficiently far apart that their electron overlap may be ignored, the electronic potential energy may be written as the inverse-power expansion [65, 66]

$$V(R) = \mathfrak{D} + \sum_m \frac{C_m}{R^m} \quad , \tag{3.12}$$

where the powers m are positive integers that depend upon the nature of the two atoms. This expression becomes invalid at smaller distances, where a "damping" function may need to be incorporated into the inverse-power expansion in order to obtain a realistic model.

Hajigeorgiou and Le Roy [8] addressed this problem by introducing the "Morse-Lennard-Jones" (MLJ) oscillator model, which has the same flexibility and compactness as the above Morse-type potential forms, but incorporates the theoretically-predicted limiting long-range behavior, and thus should extrapolate more reliably beyond the highest observed levels to dissociation. It has the form

$$V_{\rm MLJ}(R) = \mathfrak{D}_e \left[1 - \left(\frac{R_e}{R}\right)^n e^{-\beta_{\rm MLJ}(z)\, z}\right]^2 \quad , \tag{3.13}$$

with the same definitions of z and $\beta_{\rm MLJ}(z)$ as for the MMO and EMO potentials, where n is the power of the leading long-range inverse-power term. The $e^{-\beta_{\rm MLJ}(z)\, z}$ term softens the steep $1/R^{2n}$ behaviour at small distance, and the potential takes on an inverse-power form as $R \to \infty$

$$V_{\rm MLJ}(R) = \mathfrak{D}_e - 2\mathfrak{D}_e e^{-\beta^\infty} \left(\frac{R_e}{R}\right)^n = \mathfrak{D}_e + \frac{C_n}{R^n} \quad , \tag{3.14}$$

where $\beta^\infty = \lim_{R\to\infty} \beta_{\rm MLJ}(z)$, and $C_n = -2\mathfrak{D}_e (R_e)^n e^{-\beta^\infty}$ if the leading term coefficient C_n is negative (attractive), or

$$\beta^\infty = \ln\left[-2\,\mathfrak{D}_e (R_e)^n / C_n\right] \quad . \tag{3.15}$$

Eq.(3.15) indicates that β^∞ may be constrained to match the known theoretical C_n value. In practice, $\beta(z)$ is a sum of a finite number of terms (say N),

$$\beta_{\rm MLJ}(z) = \sum_{i=0}^{N} \beta_i\, z^i \quad , \qquad \text{so that} \qquad \beta_\infty = \lim_{R\to\infty} \beta_{\rm MLJ}(z) = \sum_{i=0}^{N} \beta_i \quad . \tag{3.16}$$

A polynomial constraint may be used to require that a MLJ potential have a correct externally-determined C_n coefficient; i.e., a knowledge of the C_n value allows the determination of the last

coefficient of the $\beta(z)$ function in terms of the others:

$$\beta_N = \ln\left[-2\,\mathfrak{D}_e (R_e)^n / C_n\right] - \sum_{i=0}^{N-1} \beta_i \quad . \tag{3.17}$$

One shortcoming of the MLJ model is that it incorporates only the leading term of the long-range interaction, which is not enough if the second or third terms also have strong effects on the potential energy functions. A more serious concern is the fact that, as with the GMO and MMO potential models, the MLJ model can display anomalous behaviour in the interval between the region covered by the experimental data and the asymptotic limits if the $\beta_{\rm MLJ}(z)$ function changes too rapidly. The dashed curve in the top frame of Fig. 3.1 shows the MLJ potential for the $X\,^1\Sigma^+$ state of HI determined in Ref. [8]; this potential function seems to extrapolate plausibly to the dissociation limit, but turns over at large distances as $\beta_{\rm MLJ}(z)$ passes through zero near 5.6 Å, and approaches a large limiting value.

One approach to solving this problem is to introduce a switching function [8, 9] which damps the $\beta_{\rm MLJ}(z)$ function beyond the range of the data and forces it to approach the specified β^∞ limit of Eq.(3.15) smoothly:

$$\beta_{\rm sw}(R) \;=\; f_{\rm sw}(R)\,[\beta_{\rm MLJ}(R) - \beta^\infty] + \beta^\infty \quad . \tag{3.18}$$

The switching function is defined by

$$f_{\rm sw}(R) \;=\; \frac{1}{e^{\alpha_s (R - R_s)} + 1} \quad . \tag{3.19}$$

Here, α_s is the damping strength parameter and R_s the distance at which the switching function turns on; their values are chosen manually to ensure that $\beta_{\rm sw}(R)$ has a plausible shape [10]. Application of this "switched MLJ model" to the $X\,^1\Sigma^+$ state of HI gives the solid line in the top frame of Fig. 3.1; this potential is well-behaved in the long-range region. The switched MLJ function has been applied successfully in a number of practical analyses of experimental data [10, 55, 56, 67].

3.1.5 An Improved Solution for Long-Range Extrapolation: the New EMO$_p$ and MLJ$_p$ Functions

As has been stated above, another deficiency of these potential models may arise from the behaviour of the $\beta(R)$ power series, which sometimes has implausible extrema or oscillations between the experimental data region and the very long range region where the inverse-power expansion of Eq.(3.12) becomes dominant, since a rapidly varying $\beta(R)$ function there may cause a potential curve to behave unphysically. [1] In the worst case, the potential curve can turn over and diverge, as shown by the dashed curve in the upper segment of Fig. 3.1, if the $\beta(z)$ function decreases steeply enough and changes sign.

We have found that a simple solution to this problem is to use the modified Šurkus-type expansion variable [53]

$$y_p(R) = \frac{R^p - {R_e}^p}{R^p + {R_e}^p} \quad , \tag{3.20}$$

with the β function being expanded as

$$\beta(y_p) = \beta_0 + \beta_1\, y_p + \beta_2\, {y_p}^2 + \beta_3\, {y_p}^3 + \ldots \quad , \tag{3.21}$$

where p is a small positive integer. For all values of p, the $y_p(R)$ variable has the domain $[-1, 1]$ for $R \in [0, +\infty)$. If $p = 1$, then $y_1(R) = z$. With $p = 2$ or 3, the $y_p(R)$ function helps by reducing the length of the extrapolation region expressed in terms of this variable, since the power p forces the $\beta(y_p)$ function to approach the limit more rapidly. This is illustrated by Fig. 3.2 in which $y_p(R)$ is plotted versus R/R_e for various values of p. It can be seen from this plot that for a fixed range of distance which the experimental data cover, the extrapolation region in terms of $y_p(R)$ is a much smaller fraction of its whole domain $[-1, 1]$ for power $p = 6$ than is for $p = 1$. For example, for $X\,{}^1\Sigma_g^+$ of Rb_2, $R_e = 4.2099\,\text{Å}$ and the experimental data span the interval from 2.1

[1] The rapid change of β functions may not be bad behaviour if the given potential curves are shelf-state or double-minimum potentials. In these cases a rapidly varying β function is required to yield the shape of a shelf or double-minimum [8].

to 12.35 Å (i.e., $R/R_e = 0.50 - 2.93$), and the associated ranges of y_p are:

$$\begin{aligned} y_1(R) &\in [-0.33, 0.49] \\ y_2(R) &\in [-0.60, 0.79] \\ y_3(R) &\in [-0.78, 0.92] \\ y_4(R) &\in [-0.88, 0.97] \\ y_5(R) &\in [-0.94, 0.99] \\ y_6(R) &\in [-0.97, 1.00] \quad . \end{aligned}$$

The above numbers show that with increasing p value, the extrapolation range in terms of $y_p(R)$ decreases, until the experimental data span almost its whole $[-1, 1]$ range. On the other hand, if p is too large, the potential approaches the asymptote too abruptly, which may result in a lack of flexibility in the potential form, which in turn would lead to a poor fit to the experimental data. Therefore, an appropriate value of p is required to ensure a well-behaved long-range potential and a good quality fit. This is demonstrated below for the case of the $X\,^1\Sigma_g^+$ state of Rb_2. The EMO and MLJ models expanded in terms of $y_p(R)$ are denoted by EMO_p and MLJ_p.

Illustrative applications of the new EMO_p and MLJ_p functions have been made to the ground states of the coinage metal hydrides and the Rb_2 molecule. The EMO_p model was used in re-fitting to the spectra of coinage metal hydrides because the experimental data cover only the lower part of the potential well, and thus the fits are not expected to be able to determine $\mathfrak{D}_e$. As was found by Seto *et al.* [9, 15], their fitted EMO_1 potential for the $X\,^1\Sigma^+$ state of CuH turns over at both short and long range, and their potential curve for ground state AuH misbehaves at long range. The bottom frame of Fig. 3.3 shows the published ground-state potential curves for the coinage metal hydrides obtained using the original EMO (or EMO_1) function [9]; the curves are solid in the experimental data regions, and dotted/dash-dotted in the extrapolation regions. The upper frame of this figure shows the associated $\beta(z)$ functions. As seen from these plots, when the $\beta(z)$ functions drop off sufficiently steeply that the absolute value of the product $\beta(z)\,(R - R_e)$ decreases with increasing/decreasing R, the potential begins to turn over; when

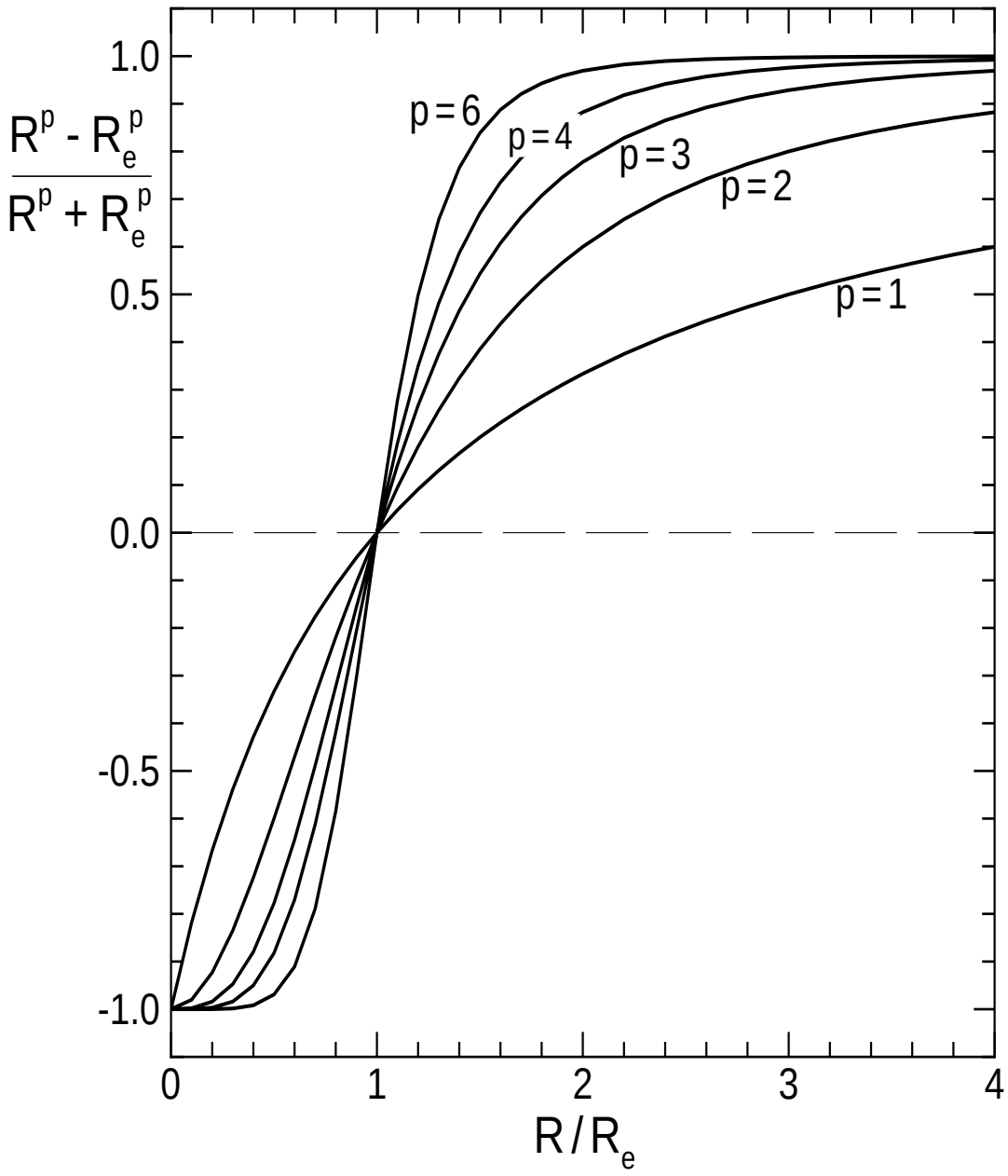

Figure 3.2: Behaviour of $y_p(R)$ for different values of p.

$\beta(z)$ passes through zero, the potential has a spurious additional minimum of depth $\mathfrak{D}_e$, and as $\beta(z)$ decreases further the potential has a spurious repulsive wall. This type of behaviour could affect any of the analytical functions discussed above.

The pathological behaviour discussed above was removed from the potential curves for the ground-state coinage metal hydrides when the EMO_3 function was used in the fits. Fig. 3.4 shows the plots of the potential curves and $\beta(y_3)$ functions obtained from fits to exactly the same multi-isotopomer data sets using EMO_3 model. The fits to data with the EMO_3 function are just as good as the published fits obtained with the EMO_1 form. However, the $\beta(y_3)$ functions remain positive for $R \in [0, \infty)$ Å, and smoothly approach limiting values without any implausible extrema. This means that the $\beta(y_3)$ are well-behaved over the entire range of the distance variable.

The rubidium dimer serves as a good example for testing the long-range behaviour of the $\beta(R)$ functions and the potential curves, since transition data are available for the ground electronic state up to $v = 113$, while v_D is 122.994 ± 0.012 [9, 10]. An accurate MLJ (or MLJ_1) ground-state potential curve for this molecule was recently reported by Seto *et al.* [10]. However, an undesired switching function was required to force the $\beta(z)$ function to approach the correct limiting value defined by the known theoretical C_6 coefficient. There is considerable current interest in obtaining a ground-state potential energy curve of very high accuracy over the widest possible range of distance for this molecule, since it has been a key species for studying Bose-Einstein condensation and ultracold gases. Therefore, a re-analysis of this molecule is done here.

The MLJ_p potential model was used in this case because the last observed level is only $7\,cm^{-1}$ from the dissociation limit ($\mathfrak{D}_e = 3993.53 \pm 0.06\,cm^{-1}$ [68]). The $\beta(y_p)$ function is constrained to incorporate the correct long-range C_6 coefficient by applying a polynomial constraint

$$\beta(y_p) = \sum_{i=0}^{N-1} \beta_i \, {y_p}^i + \beta_N \, {y_p}^N \qquad \text{and} \qquad \beta_N = \beta^\infty - \sum_{i=0}^{N-1} \beta_i \tag{3.22}$$

with β^∞ defined by Eq.(3.15). The experimental data were fitted to the MLJ_p form for values of p ranging from 1 to 6. The quality of fit is equally good for the first three cases ($p = 1 - 3$). Fig. 3.5 shows the potential curve and $\beta(y_p)$ function of the ground electronic state of Rb_2 obtained with

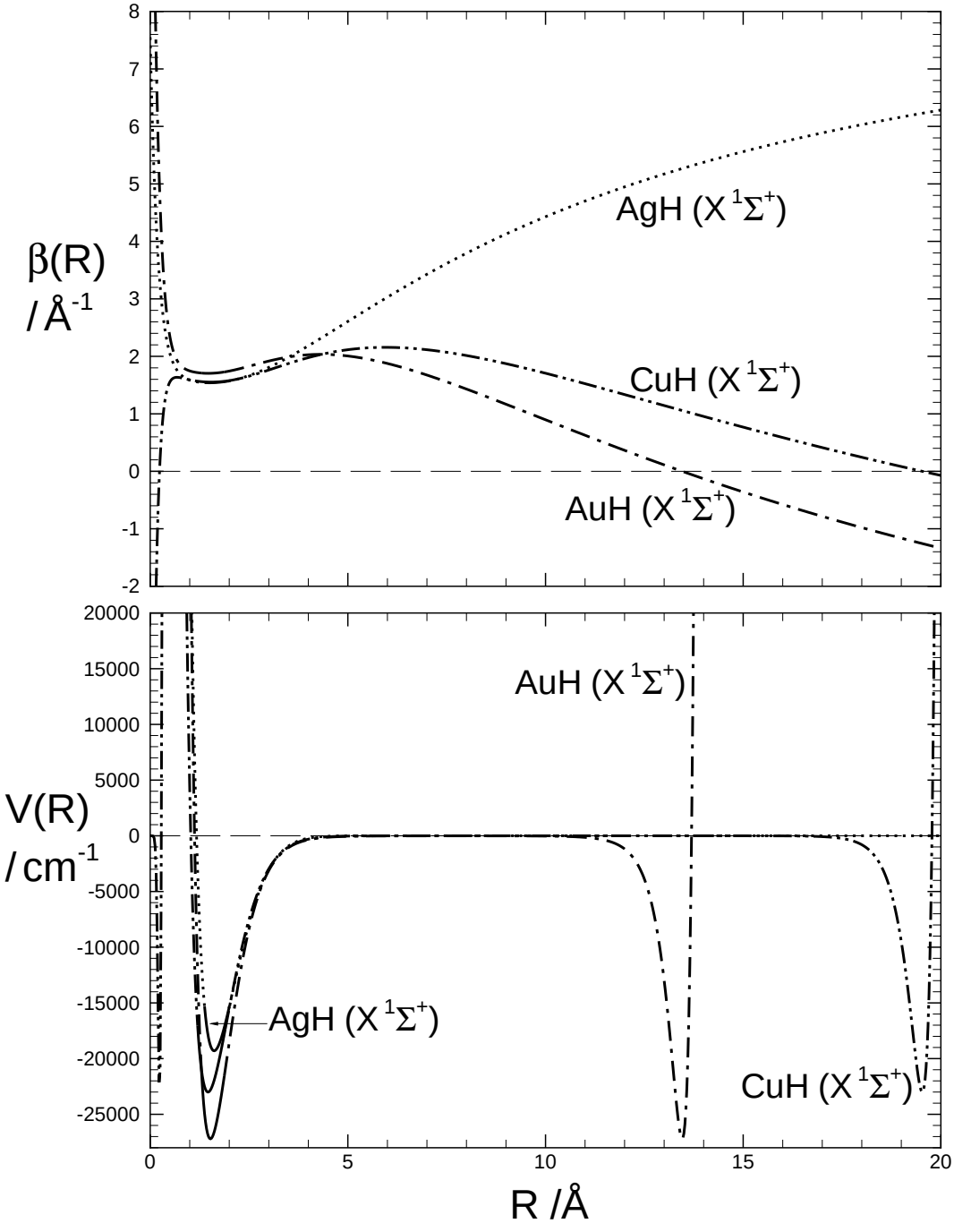

Figure 3.3: The published ground-state potential curves of the coinage metal hydrides obtained using the EMO_1 form, from the experimental data for all isotopomers: ^{63}CuH, ^{65}CuH, ^{63}CuD and ^{65}CuD; ^{107}AgH, ^{109}AgH, ^{107}AgD and ^{109}AgD; ^{197}AuH and ^{197}AuD. Adapted from Fig. 3.2 of Ref. [9].

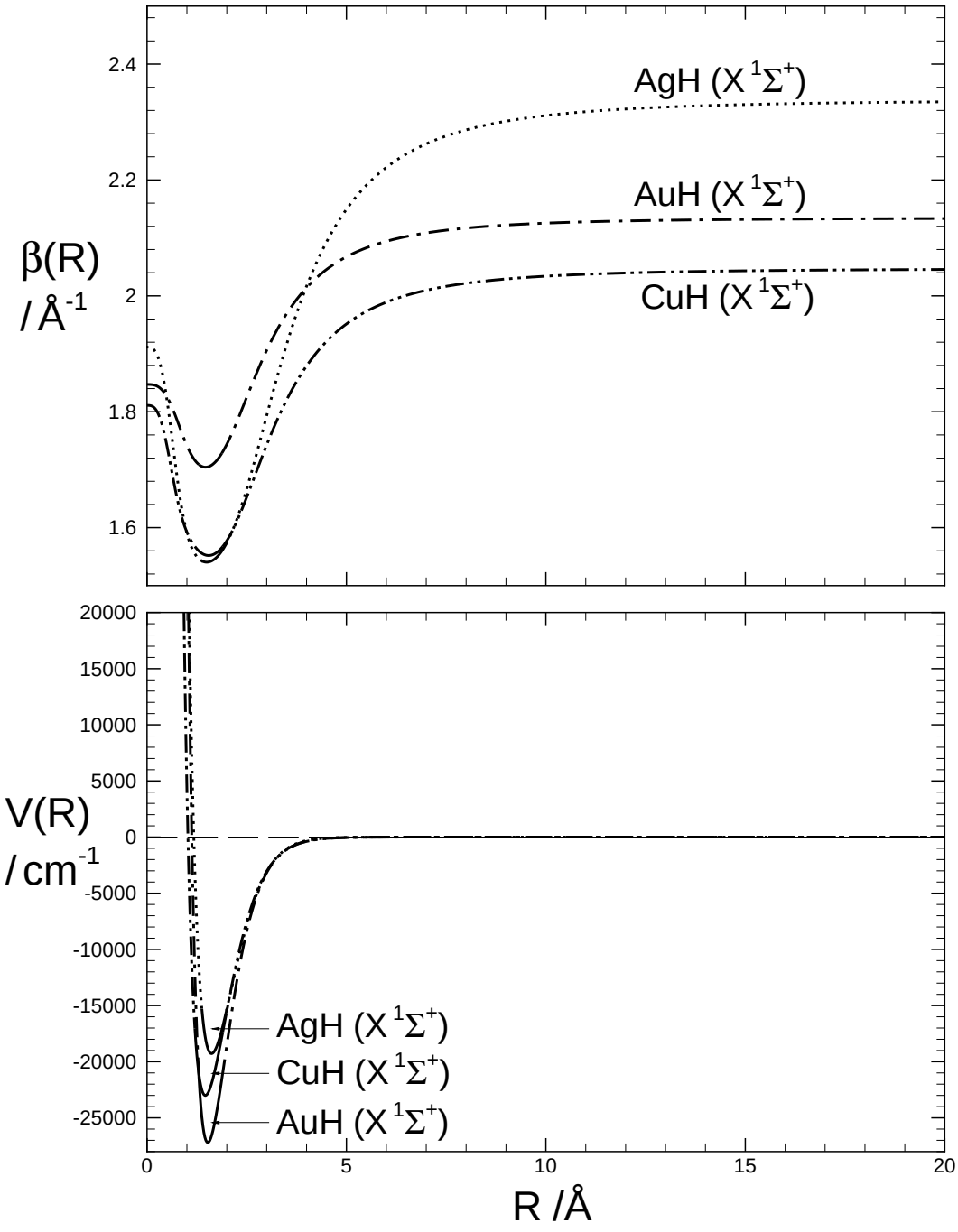

Figure 3.4: Ground state potential curves of the coinage metal hydrides obtained using the EMO_p form with $p = 3$, from experimental data for all isotopomers: ^{63}CuH, ^{65}CuH, ^{63}CuD and ^{65}CuD; ^{107}AgH, ^{109}AgH, ^{107}AgD and ^{109}AgD; ^{197}AuH and ^{197}AuD.

$p = 1$; the $\beta(y_1)$ function passes through a large maximum (off the scale of the plot) before it drops down to the constrained limiting value of $\beta^\infty = 0.6764\,\text{Å}^{-1}$.

With p values increasing from 1 to 3, the resulting fitted Rb_2 potential curves are indistinguishable on the scale of Fig. 3.5. However, the $\beta(y_p)$ functions behave quite differently. The bottom segment of Fig. 3.6 compares the $\beta(y_p)$ functions obtained with different p values. The published "switched $\beta(z)$ function" [10] is also included for comparison. The $p = 2$ function passes through a small maximum, which would cause the potential to approach the asymptote too abruptly, while the $\beta(y_3)$ curve smoothly approaches β^∞ from below the limit. The switched $\beta(z)$ function originally exceeds the limiting β_∞ value, but is forced to return to the limiting value by the switching function.

To show how the potentials actually differ, even though they look the same on the potential plot, the potential functions are multiplied by R^6. The $V(R) \times R^6$ curves must all approach the imposed C_6 value at long range. However, the resulting curves exhibit very different behaviour before approaching that limiting C_6 value. This is shown in the upper frame of Fig. 3.6. The $p = 1$ curve does not approach the C_6 value until very large R, and it goes very abruptly almost to zero immediately outside the data region. The $p = 2$ curve passes through a large maximum which is above the C_6 value before it reaches the limiting value. The switched MLJ curve goes through a small anomalous minimum before approaching C_6 limit. Only the $p = 3$ curve smoothly approaches the limiting value from below, which is what is to be expected, since the full long-range potential has attractive $1/R^8$ and $1/R^{10}$ terms.

The parameter $\mathfrak{D}_e$ was free in the above fits to the experimental data, and the fitted MLJ_1 and MLJ_2 functions give inaccurate predictions of $\mathfrak{D}_e$ because their $\beta(y_p)$ functions behave badly. The $\mathfrak{D}_e$ value obtained from a "photoassociation spectroscopy" (PAS) experiment [68] is $3993.53 \pm 0.06\,\text{cm}^{-1}$; this value is expected to be reliable, since the binding energies of the levels used in the analysis are very small. The dissociation energies $\mathfrak{D}_e$ obtained from the $p = 1$ and $p = 2$ fits, respectively, are $3989.02\,\text{cm}^{-1}$ and $3992.74\,\text{cm}^{-1}$ which are inaccurate. However, the $\mathfrak{D}_e$ obtained from the fit with MLJ_3 is $3993.65\,\text{cm}^{-1}$, which is in remarkable agreement with PAS result.

Table 3.1 lists the fitted parameters of the recommended polynomial-constrained MLJ_3 func-

tion determined here for the $X\,^1\Sigma_g^+$ state Rb_2. The number of free parameters in this fit is the same as that required for the switched MLJ_1 function [10], since although the switched MLJ_1 $\beta(z)$ polynomial had only 15 fitted coefficients, it required another two manually-fitted parameters. Both models fit the data equally well. However, the fit with the switching function was unable to determine an accurate $\mathfrak{D}_e$ [10]. Furthermore, an unsettling feature of the MLJ_1 function is that its higher-order β coefficients have magnitude 10^7, while those of MLJ_3 function do not grow as large. Using coefficients of magnitude 10^7 to define function values of magnitude 10^0 will more likely yield bad extrapolation. Thus, introducing the new $y_p(R)$ variable avoids both the use of the inelegant switching function and the arbitrariness associated with the choice of the switching function control parameters R_s and α_s of Eq.(3.19) [10].

The above discussion does not mean that the larger the p value is, the better the fitting result we can obtain. If the $y_p(R)$ variable approaches its limits of ± 1 too abruptly, the $\beta(y_p)$ function will lose its flexibility, and the fitted potential functions will not be able to fully account for the experimental data. For the $X\,^1\Sigma_g^+$ of Rb_2, the best MLJ_p potential fit obtainable using $p = 4$ gives RMSR $= 3.526$, which is more than three times worse than that obtained using the MLJ_3 form (see Table 3.1). Even worse, the best $p = 6$ fit gives an RMSR value of 203.7, which shows that a too high power of p makes the model too rigid to use. Clearly, $p = 3$ is the best choice in this case. Thus, an appropriate p value should ensure that the $\beta(y_p)$ function is flexible enough in representing the experimental data, but should have $y_p(R)$ approach its limits abruptly enough to avoid unphysical behaviour in extrapolation.

3.1.6 The Constrained Morse-Lennard-Jones Oscillator

An alternative MLJ potential model which explicitly incorporates the β^∞ constraint and takes advantage of the $y_p(R)$ expansion variable can be expressed as

$$V_{\mathrm{MLJ}_p^c(R)} = \mathfrak{D}_e \left[1 - \left(\frac{R_e}{R} \right)^n e^{-\beta_{\mathrm{MLJ}_p^c}(R)} \right]^2 \quad , \tag{3.23}$$

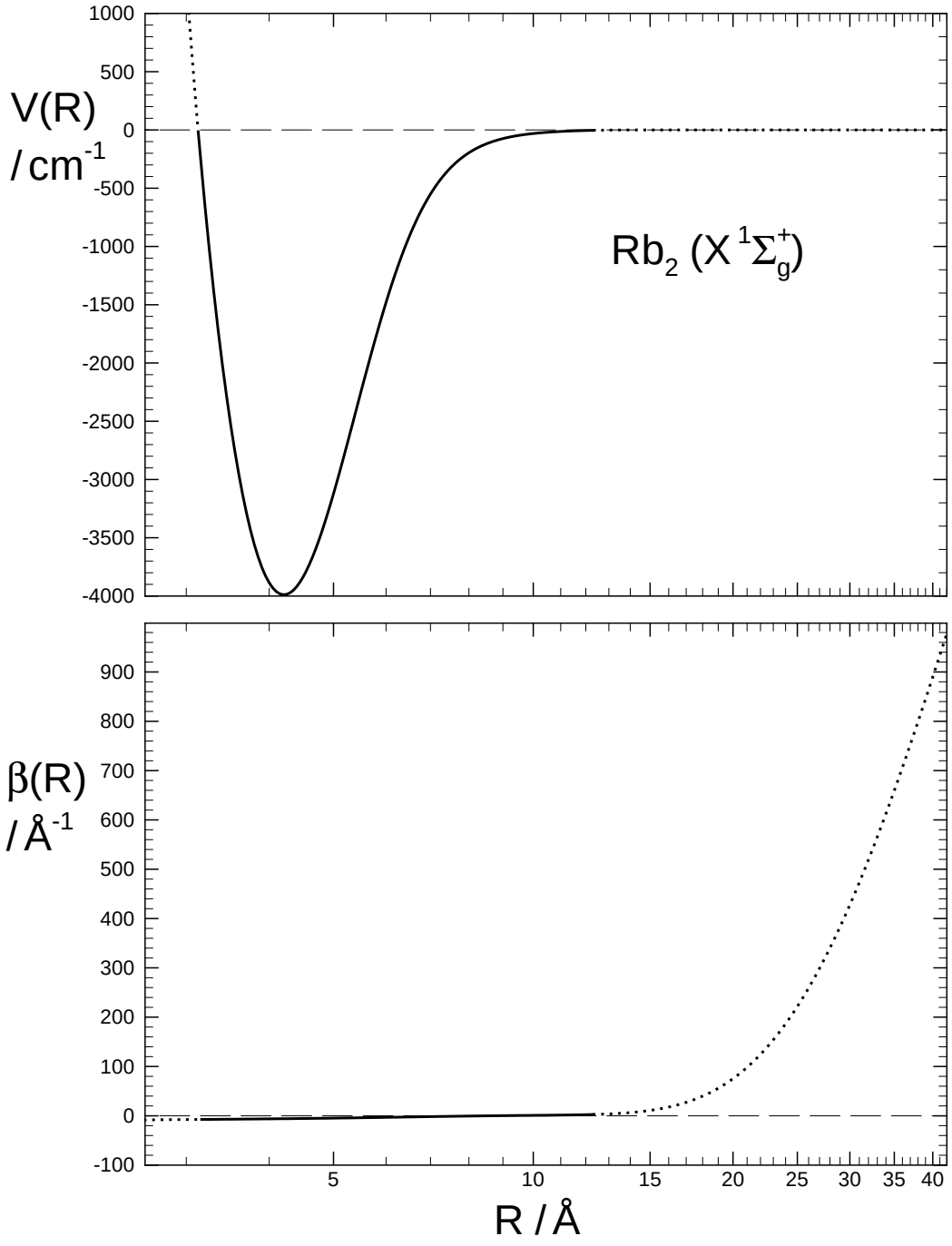

Figure 3.5: Ground state potential curve and $\beta(y_1)$ function of Rb_2 obtained using the MLJ_1 model. The distance variable R is on a logarithmic scale.

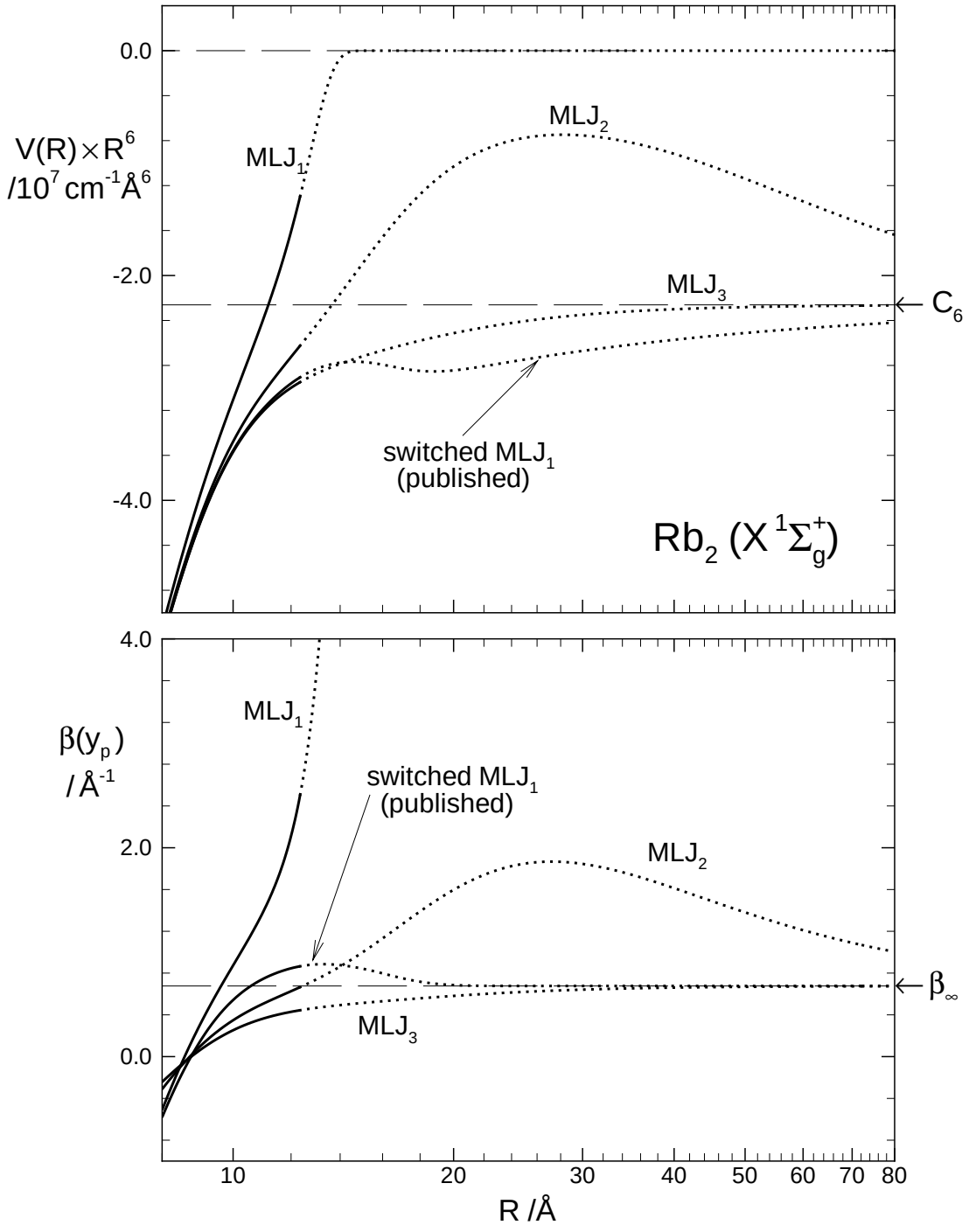

Figure 3.6: Plots of $V(R) \times R^6$ and $\beta(y_p)$ functions for fitted potentials of ground-state Rb_2 with different p values. Curves for the switched MLJ_1 function are generated from the parameters taken from Table 2 of Ref. [10]. The distance variable R is on a logarithmic scale.

Parameter	$^{85}Rb_2$	
$\mathfrak{D}_e$ / cm^{-1}	3993.65668	($\pm 6.8 \times 10^{-3}$)
R_e / Å	4.20991431	($\pm 7.7 \times 10^{-6}$)
β_0 / Å^{-1}	-1.9634495	($\pm 7.7 \times 10^{-6}$)
β_1 / Å^{-1}	1.3459925	($\pm 1.9 \times 10^{-4}$)
β_2 / Å^{-1}	-0.0565667	($\pm 5.7 \times 10^{-4}$)
β_3 / Å^{-1}	1.2469171	($\pm 6.2 \times 10^{-3}$)
β_4 / Å^{-1}	0.603262	($\pm$0.016)
β_5 / Å^{-1}	-0.692695	($\pm$0.11)
β_6 / Å^{-1}	0.36603	($\pm$0.23)
β_7 / Å^{-1}	13.28649	($\pm$1.1)
β_8 / Å^{-1}	-8.4566	($\pm$1.8)
β_9 / Å^{-1}	-92.524	($\pm$7.4)
β_{10} / Å^{-1}	132.716	($\pm$8.9)
β_{11} / Å^{-1}	264.96	($\pm$27.)
β_{12} / Å^{-1}	-696.94	($\pm$37.)
β_{13} / Å^{-1}	47.6	($\pm$34.)
β_{14} / Å^{-1}	1183.5	($\pm$82.)
β_{15} / Å^{-1}	-1251.0	($\pm$63.)
β_{16} / Å^{-1}	450.3846	
β^∞ / Å^{-1}	0.6764	
C_6 / cm^{-1} Å^6	-2.261×10^7	
# data	12148	
RMSR	1.006	

Table 3.1: Parameters and fitting quality for the recommended MLJ$_3$ potential for the $X\,^1\Sigma_g^+$ state of Rb_2. The C_6 value has been taken from Ref. [1], while β_{16} is defined by C_6 (or β^∞) through the polynomial constraint of Eq.(3.22).

where

$$\beta_{\mathrm{MLJ}_p^c}(R) = \beta^\infty \left(\frac{R^p - {R_e}^p}{R^p + {R_e}^p}\right) + \left(\frac{2{R_e}^p}{R^p + {R_e}^p}\right) \sum_{i=1} \beta_i \left(\frac{R^p - {R_e}^p}{R^p + {R_e}^p}\right)^i \tag{3.24}$$

and β^∞ is defined by Eq.(3.15). In this form the limiting constraint is imposed explicitly, rather than through a polynomial constraint. This model is denoted by MLJ_p^c. It is easy to see that for this form $\beta_{\mathrm{MLJ}_p^c}(R) \to \beta^\infty$ as $R \to \infty$. A MLJ_p^c potential has the same features as a MLJ_p function, and should yield fits of equal quality, but it has not yet been fully tested.

3.1.7 Two Solutions to Short-Range Extrapolation Problems

The preceeding discussion shows that the long-range extrapolation problem can often be solved simply by use of the $y_p(R)$ expansion variable with $p > 1$. It turns out that the $y_p(R)$ expansion variable with $p > 1$ also helps solve the problem of pathological behaviour in the short-range region. In the silver hydride example discussed above, if the data for only the two isotopomers ^{107}AgH and ^{109}AgH are used in the fits to the EMO_1 function, then the fitted potential energy function turns over in the short-range region [9]. This is shown in the extrapolated dotted curve labeled as "$\beta_{R=0}$ Unconstrained" in bottom frame of Fig. 3.7. Seto examined the use of a short-range power-series constraint method to fix the $\beta(z)$ function to a positive value at $R = 0$, in an attempt to reduce the chance that the $\beta(z)$ function will change sign or decrease too abruptly with decreasing R, and thus causes the potential to misbehave [9]. Analogous to the discussion associated with Eq.(3.22), Seto's power-series constraint was implemented by adding an extra term to $\beta(z)$ function of EMO model; i.e.,

$$\beta(z) \;=\; \sum_{i=0}^{N} \beta_i \, z^i + \beta_{N+1} \, z^{N+1} \quad \text{with} \tag{3.25}$$

$$\beta_{N+1} \;=\; (-1)^{N+1} \left[\beta_{R=0} - \sum_{i=0}^{N} (-1)^i \, \beta_i\right] \quad , \tag{3.26}$$

where $\beta_{R=0}$ is the value to which $\beta(z)$ is constrained at $R = 0$. The top frame of Fig. 3.7 shows the behaviour the $\beta(z)$ functions that he obtained for various $\beta_{R=0}$ values; the bottom segment of the figure shows the corresponding potential curves. It can be seen that the unphysical behaviour of the potential in the short-range region is not removed until $\beta_{R=0}$ is set to $50\,\text{Å}^{-1}$.

While the above polynomial constraint method works, it requires a manually chosen value of $\beta_{R=0}$ which has no physical meaning, and as shown by this example, that value may have to lie far outside any reasonable region one might have expected. However, this is not a problem when an EMO_p potential model with $p > 1$ is used in the fit. The fitted EMO_p potential curve is well-behaved and no $\beta_{R=0}$ constraint is needed. The $\beta(y_3)$ function and potential curve obtained using the EMO_3 model in a fit to the same data set are shown in Fig. 3.8. It is clear that use of the $p = 3$ expansion variable in this case removes all problems associated with the short-range region.

In some cases, [2] the fitted analytical EMO_p or MLJ_p potential functions may still misbehave by taking on negative curvature or turning over at small distances if high-order polynomial $\beta(y_p)$ functions are used in the fits, since the high-order $\beta(y_p)$ power series necessary to represent the outer wall of the potential well may distort the inner potential wall. A normal inner potential wall is expected to be steep and to have positive curvature, and the associated data region usually spans only the interval $0.8 \lesssim R/R_e \leq 1$; hence it should suffice to represent the inner wall by the first few terms of the $\beta(y_p)$ power series. In these cases, the $\beta(y_p)$ function can be split into two segments at the distance $R = R_e$; the $\beta(y_p)$ function for the inner segment is represented by $N_S + 1$ terms, and that for the outer segment by $N_L + 1$ terms, i.e.,

$$\beta(y_p) = \sum_{i=0}^{N_S} \beta_i\, y^i \quad \text{for } R < R_e \qquad \text{and} \tag{3.27}$$

$$\beta(y_p) = \sum_{i=0}^{N_L} \beta_i\, y^i \quad \text{for } R \geq R_e \quad , \tag{3.28}$$

where N_S and N_L are order of the $\beta(y_p)$ function, $N_S \leq N_L$, and coefficients from β_0 to β_{N_S}

[2] See Chapter 4.

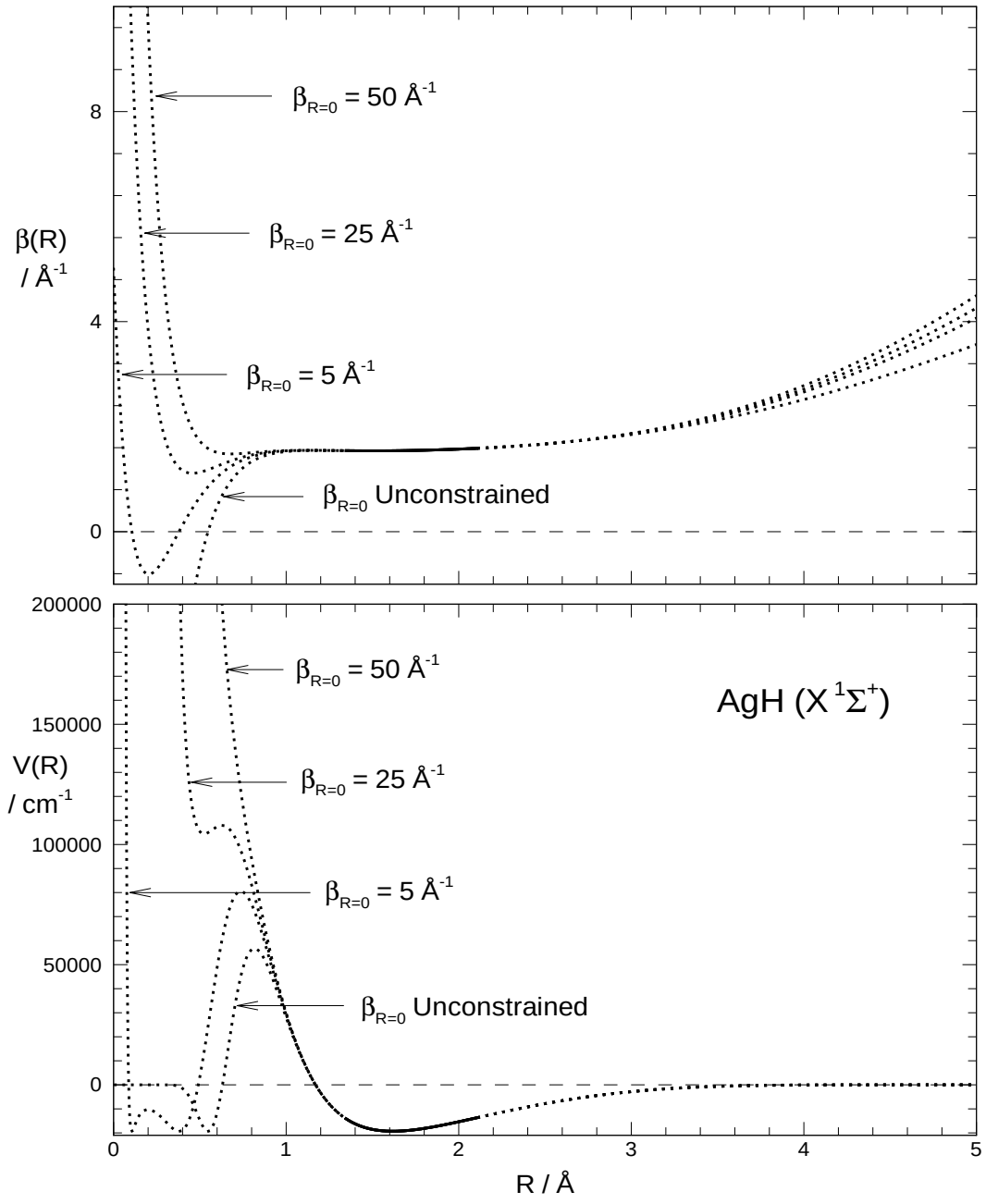

Figure 3.7: Potential Curves for the $X\,^1\Sigma^+$ state of AgH with Power Series Constraint, adapted from Fig. 3.3 of Ref. [9].

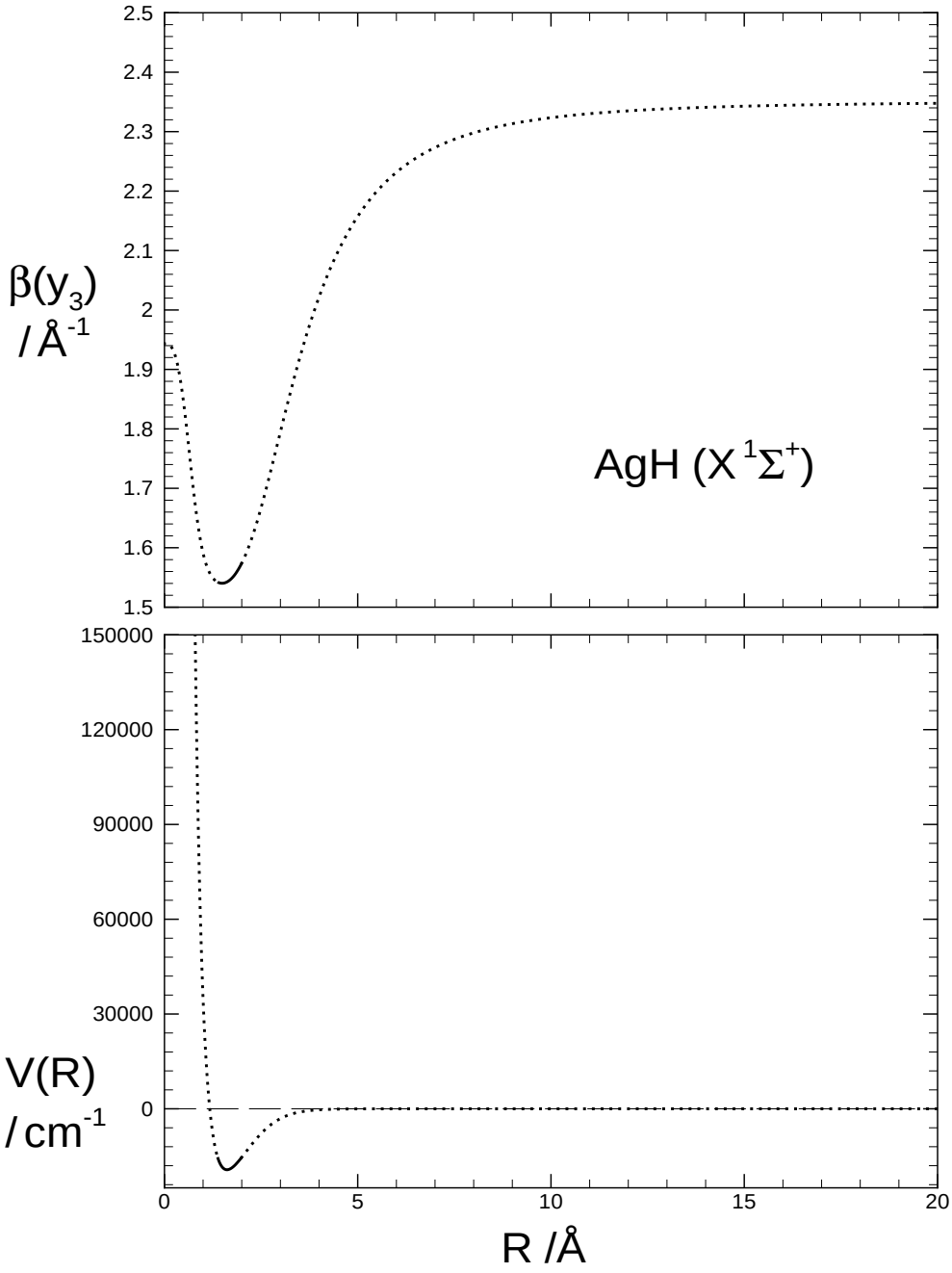

Figure 3.8: Potential Curves of the $X\,^1\Sigma^+$ state of AgH obtained using the EMO_3 model.

are identical in both Eqs.(3.27) and (3.28). Note that this means the $(N_S + 1)^{th}$ derivative of the $\beta(y_p)$ function with respect to y_p will be discontinuous at $R = R_e$. However, because of its algebraic form the derivatives of the potential itself will be discontinuous at $R = R_e$ only at the order of $(N_S + 2)$ or higher. The "separate-power" method for the $\beta(y_p)$ function is effective in eliminating the spurious behaviour of the short-range region. An application of this approach can be found in Chapter 4.

3.1.8 The Double-Exponential Long-Range Potential Function

None of the forms derived to date can represent a barrier protruding above the potential asymptote. Moreover, these forms do not take account of multiple inverse-power long-range terms. A new potential model developed in this work to describe a potential curve with a barrier is denoted the "double-exponential long-range" (DELR) potential energy function. It is a combination of two exponential terms plus an analytical function to represent the long-range behaviour:

$$V_{\rm DELR}(R) \;=\; [{\rm A}\, e^{-2\beta(y_p)\,(R-R_e)} \;-\; {\rm B}\, e^{-\beta(y_p)\,(R-R_e)} \;+\; \mathfrak{D}_e] \;+\; V_{\rm LR}(R) \quad , \tag{3.29}$$

where $\beta(y_p)$ is a simple polynomial as defined by Eq.(3.21), and A and B are explicit analytical functions of $\mathfrak{D}_e$, R_e, β_0 and the value and first derivative of $V_{\rm LR}(R)$ evaluated at $R = R_e$. In particular, since

$$V_{\rm DELR}(R_e) = 0 \qquad \text{and} \qquad \left.\frac{dV_{\rm DELR}(R)}{dR}\right|_{R=R_e} = 0 \quad , \tag{3.30}$$

A and B are defined by the expressions:

$$\mathrm{A} \;=\; \mathfrak{D}_e \;+\; V_{\rm LR}(R_e) \;+\; \frac{V'_{\rm LR}(R_e)}{\beta_0} \tag{3.31}$$

and

$$\mathrm{B} \;=\; 2\mathfrak{D}_e \;+\; 2V_{\rm LR}(R_e) \;+\; \frac{V'_{\rm LR}(R_e)}{\beta_0} \quad , \tag{3.32}$$

where

$$V'_{\rm LR}(R_e) \equiv \left.\frac{dV_{\rm LR}}{dR}\right|_{R=R_e} \quad . \tag{3.33}$$

As for the various functions discussed in the preceeding sections, use of the expansion variable y_p with $p > 1$ and $\beta(y_p)$ defined by Eqs.(3.27) and (3.28) with $N_S \leq N_L$ will eliminate the unphysical behaviour at small distances.

A particularly useful form of $V_{\rm LR}(R)$ is the general inverse-power expansion for a long-range potential [69, 70, 71]

$$V_{\rm LR}(R) \;=\; \sum_n \frac{C_n}{R^n} {\rm D_n}(R) \quad , \tag{3.34}$$

where $\rm D_n$ is a damping function which corrects for the shrinking strength of the inverse-power terms as electron overlap between the component atoms grows at small R. The $\rm D_n$ function used herein is expressed as [72]

$${\rm D_n}(R) \;=\; \left[1 - \exp\{-2.1(\rho_x\, R)/n - 0.109(\rho_x\, R)^2/\sqrt{n}\}\right]^n \quad , \tag{3.35}$$

in which ρ_x is a system-dependent scaling factor based on the ratio of ionization potentials of the component atoms to the hydrogen atom. Fig. 3.9 illustrates how the components of the DELR potential yield a potential energy curve with a barrier.

This double-exponential model is closely related to the Morse-type potential functions discussed earlier. If $V_{\rm LR}(R) = 0$, then $A = \mathfrak{D}_e$ and $B = 2\mathfrak{D}_e$, and a DELR function turns into an extended Morse Oscillator potential. The DELR model is an explicit function of the physically-meaningful variables $\mathfrak{D}_e$ and R_e, but it allows one to include all appropriate inverse-power terms and to provide a more sophisticated treatment of the long-range behaviour. In effect, the DELR function uses a flexible Morse-type form for the well region, while the inverse-power expansion is used to simulate the long-range potential and (when appropriate) the repulsive outer wall of a potential barrier. In principle, the DELR model can represent any irregularly shaped potential

curve, including a double-minimum well, by adjusting the C_n values within $V_{\rm LR}(R)$ as in Eq.(3.34) and $\{\beta_i\}$ parameters, or simply by using an alternative algebraic form for $V_{\rm LR}(R)$.

In view of the above, the EMO$_p$, MLJ$_p$ or MLJ$_p^c$ and DELR functions are more reliable potential models which minimize pathological behaviour in extrapolation. These potential models have been implemented in the computer program DSPotFit. Because the non-linear least-squares fit procedure of the DPF approach requires one to know the partial derivatives of the potential functions with respect to its fitting parameters, the relevant partial derivatives of these models are listed in Appendix A. In Chapters 4 and 5, the DELR model is used to represent the $B\,^1\Pi_u$ state of the lithium dimer and the $X\,^2\Sigma^+$ state of the BeH molecule. Note, however, that Born-Oppenheimer breakdown correction terms must be included in order to account accurately for the differences between isotopomers.

3.2 Born-Oppenheimer Breakdown (BOB) Effects

The first concern of a DPF analysis is to determine the effective radial potential function for the major isotopomer of the species of interest. Potential functions for other "minority" isotopomers are identical within the clamped-nuclei limit of the Born-Oppenheimer approximation. However, the Born-Oppenheimer approximation tends to break down for lighter molecular systems, since effective potential functions are slightly different for different isotopomers, and these discrepancies increase as the reduced mass of the molecule decreases. Thus, correction terms should be added to the Schrödinger equation Eq. (2.3) in such cases. In a detailed treatment of H_2^+, Bunker and Moss [30] described these breakdown effects by introducing an effective Hamiltonian which yielded the radial Schrödinger equation

$$\left[-\frac{\hbar^2}{2\mu_n}\frac{d}{dR}[1+\beta(R)]\frac{d}{dR}+\frac{\hbar^2 J(J+1)}{2\mu_n R^2}[1+q_n(R)]+V_{CN}(R)+\delta V(R)\right]\psi_{vJ}(R)=E_{vJ}\,\psi_{vJ}(R)\quad , \tag{3.36}$$

where μ_n is the reduced mass of the nuclei, $V_{CN}(R)$ is the clamped-nuclei potential obtained within the Born-Oppenheimer approximation, and $\delta V(R)$ represents adiabatic effects due to coupling between nuclear and electronic motions, as well as mass polarization terms, and is responsible

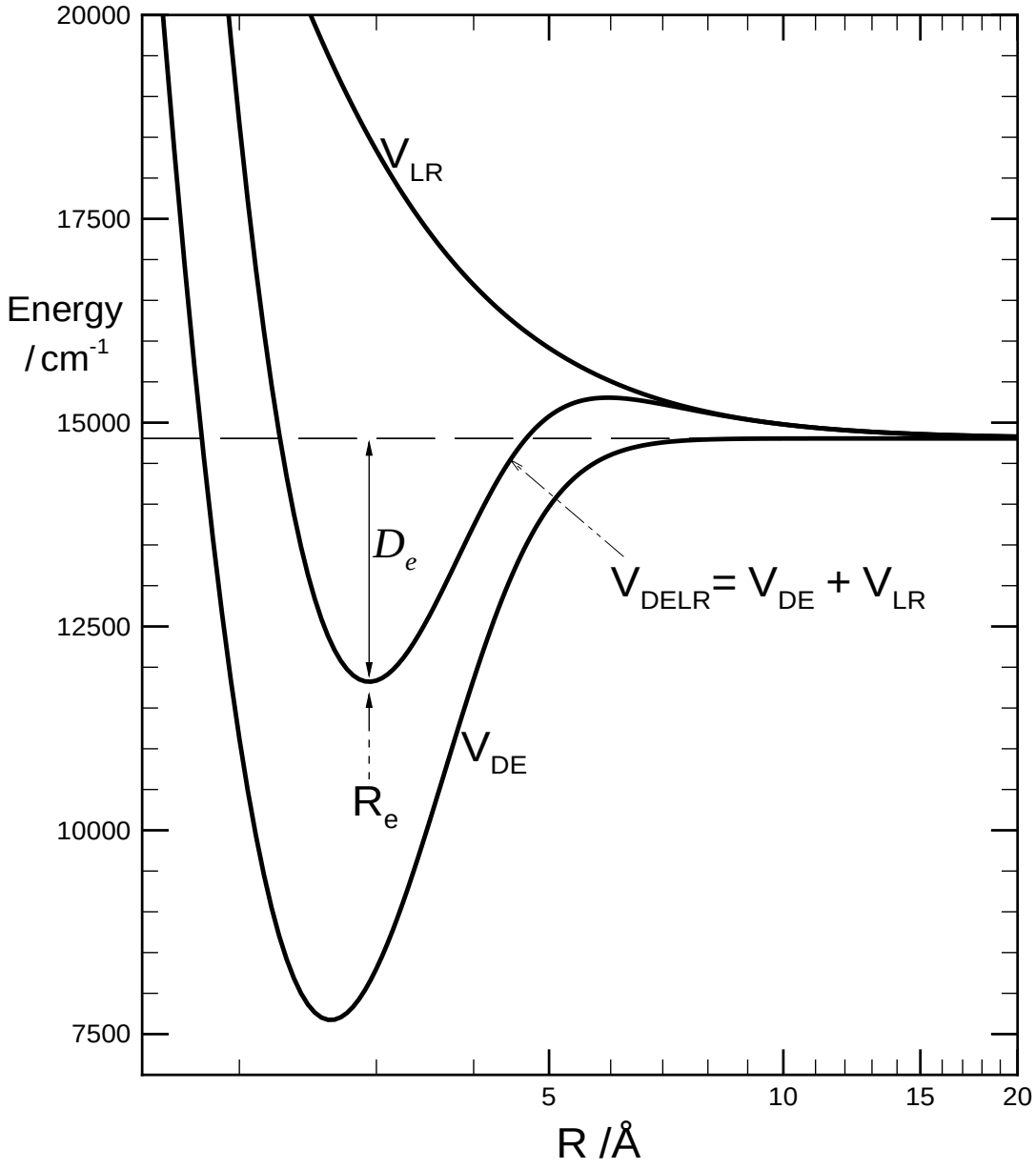

Figure 3.9: Illustration of the DELR potential components for $B\,^1\Pi_u$ state of Li_2. The distance variable R is on a logarithmic scale.

for the slight differences between the potential functions for different isotopomers. The functions $q_n(R)$ and $\beta(R)$ represent non-adiabatic rotational and vibrational effects, reflecting the failure of the electrons to follow precisely the rotational and vibrational motions of the nuclei.

A more widely used description of Born-Oppenheimer breakdown effects given by Watson [31] leads to the effective radial Schrödinger equation

$$\left[-\frac{\hbar^2}{2\mu_\alpha}\frac{d^2}{dR^2}+\frac{\hbar^2 J(J+1)}{2\mu_\alpha R^2}[1+q^\alpha(R)]+V_{CN}(R)+\Delta V^\alpha(R)\right]\psi_{vJ}(R)=E_{vJ}\,\psi_{vJ}(R) \quad , \qquad (3.37)$$

in which μ_α is the reduced mass of the atoms of isotopomer-α, $q^\alpha(R)$ represents non-adiabatic correction terms, and $\Delta V^\alpha(R)$ represents adiabatic effects. An apparent deficiency of Eqs. (3.36) and (3.37) is the fact that $V_{CN}(R)$ is the theoretical clamped-nuclei potential obtained in the lowest-order version of the Born-Oppenheimer approximation, and does not describe any real molecular species, which makes its physical meaning somewhat obscure. To address this problem, Le Roy introduced an improved representation in which the potential of the dominant isotopomer was selected as the reference point, instead of the extrapolated non-physical potential $V_{CN}(R)$ [15, 32]:

$$\left[-\frac{\hbar^2}{2\mu_\alpha}\frac{d^2}{dR^2}+\frac{\hbar^2 J(J+1)}{2\mu_\alpha R^2}[1+q^\alpha(R)]+V_{\rm ad}^\alpha\right]\psi_{vJ}(R)=E_{vJ}\,\psi_{vJ}(R) \quad , \qquad (3.38)$$

where

$$V_{\rm ad}^\alpha = V_{\rm ad}^1 + \Delta V_{\rm ad}^\alpha(R) \quad . \qquad (3.39)$$

Here, $V_{\rm ad}^\alpha$ is the total potential function for isotopomer-α, $V_{\rm ad}^1$ is the potential for the selected reference isotopomer ($\alpha = 1$), which is usually chosen as the one for which the widest range of data is available, and the adiabatic correction term $\Delta V_{\rm ad}^\alpha(R)$ corrects for the difference between the potentials for isotopomer-α and isotopomer-1. In previous work in our laboratory the adiabatic and non-adiabatic correction terms were expressed as

$$\Delta V_{\rm ad}^\alpha(R) \;=\; \frac{\Delta M_{\rm A}^\alpha}{M_{\rm A}^\alpha}\Delta V_{\rm ad}^{\rm A}(R)+\frac{\Delta M_{\rm B}^\alpha}{M_{\rm B}^\alpha}\Delta V_{\rm ad}^{\rm B}(R) \;=\; \frac{\Delta M_{\rm A}^\alpha}{M_{\rm A}^\alpha}\sum_i u_i^{\rm A} z^i+\frac{\Delta M_{\rm B}^\alpha}{M_{\rm B}^\alpha}\sum_i u_i^{\rm B} z^i \quad , \qquad (3.40)$$

and

$$q^{\alpha}(R) \;=\; \frac{M_{\rm A}^{1}}{M_{\rm A}^{\alpha}}\, q_{\rm A}(R) + \frac{M_{\rm B}^{1}}{M_{\rm B}^{\alpha}}\, q_{\rm B}(R) \;=\; \frac{M_{\rm A}^{1}}{M_{\rm A}^{\alpha}} \sum_i q_i^{\rm A} z^i + \frac{M_{\rm B}^{1}}{M_{\rm B}^{\alpha}} \sum_i q_i^{\rm B} z^i \quad , \tag{3.41}$$

where $M_{\rm A}^{1}$ and $M_{\rm B}^{1}$, $M_{\rm A}^{\alpha}$ and $M_{\rm B}^{\alpha}$ are the masses of atoms A and B for isotopomer-1 and isotopomer-α, respectively, $\Delta M_{\rm A}^{\alpha} = M_{\rm A}^{\alpha} - M_{\rm A}^{1}$ and $\Delta M_{\rm B}^{\alpha} = M_{\rm B}^{\alpha} - M_{\rm B}^{1}$ are their differences, $\Delta V_{\rm ad}^{\rm A}(R)$ and $\Delta V_{\rm ad}^{\rm B}(R)$ are the adiabatic BOB correction functions for atom A and B, $q_{\rm A}(R)$ and $q_{\rm B}(R)$ the non-adiabatic correction functions, $q_i^{\rm A}$, $q_i^{\rm B}$, $u_i^{\rm A}$ and $u_i^{\rm B}$ are the mass-independent empirical parameters characterizing the BOB correction terms, and $z = y_1(R)$ as defined by Eq.(3.8). The adiabatic potential correction functions $\Delta V_{\rm ad}^{\rm A}(R)$ and $\Delta V_{\rm ad}^{\rm B}(R)$ and their expansion parameters $\{u_i^{\rm A}\}$ and $\{u_i^{\rm B}\}$ have units $\rm cm^{-1}$, and their magnitudes are directly proportional to the change of the potential from one isotopomer to another.

The above expressions have been used to represent the BOB corrections in a number of recent studies [15, 17]. However, these expressions may have unphysical extrapolation at long range. Even though the nature of the variable z (or y_1) means that these BOB expansions will converge to finite values as $R \to \infty$ or $R \to 0$, they will not necessarily extrapolate to physically-meaningful limits. The differences between the potential energies for different isotopomers at their asymptotic limits should equal the associated atomic isotope shifts, which are known to be small. Therefore, constraints on the limiting values of the adiabatic correction are necessary to allow them to correlate with the known atomic isotope shifts. Similarly, the non-adiabatic centrifugal BOB correction may be significant at distances near R_e because of the coupling of different electronic states. However, this effect can be ignored for two separate atoms. Therefore, the non-adiabatic corrections should be required to be zero at the asymptotic limits.

With the limiting constraints discussed above, we proposed a new form of BOB correction expansions which uses the $y_p(R)$ variable with $p > 1$ to avoid undesired pathological behaviour in the interval between the data region and the asymptote. This form explicitly imposes the correct asymptotic values. The proposed "limit-specified" adiabatic BOB correction expansion is

$$\Delta V_{\rm ad}^{\rm A}(R) = u_0^{\rm A} \left(\frac{2{R_e}^m}{R^m + {R_e}^m} \right) + u_\infty^{\rm A} \left(\frac{R^m - {R_e}^m}{R^m + {R_e}^m} \right) + \left(\frac{2{R_e}^m}{R^m + {R_e}^m} \right) \sum_{i=1} u_i^{\rm A} \left(\frac{R^p - {R_e}^p}{R^p + {R_e}^p} \right)^i \quad , \tag{3.42}$$

where R_e is the equilibrium internuclear distance for the reference isotopomer ($\alpha = 1$), and m and p are positive integers. Making the powers m and p both greater than 1 in Eq.(3.42) has the same advantage seen for the potential energy function as discussed in Section 3.1.5. Moreover, since the potential energy function for minority isotopomer-α must have the same inverse-power long-range behaviour as does the reference isotopomer ($\alpha = 1$), in cases where correct inverse-power behaviour is imposed on the potential energy function, the adiabatic correction function must have that same long-range form. In these cases, m should be set equal to n, the power (inverse) of the asymptotically dominant term in the long-range potential, as in the MLJ$_p$ and DELR functions. However, setting $p = n$ may be too extreme, since the typical n value for a molecular electronic state is 6 or 5, which results in extreme abrupt change of y_p values. This may reduce its ability to represent $\Delta V_{\rm ad}^{\alpha}(R)$ functions with sufficient flexibility over the range of experimental data.

From the form of this expansion, it is clear that

$$\Delta V_{\rm ad}^{\rm A}(R = R_e) \;=\; u_0^{\rm A} \quad , \tag{3.43}$$

and since the factor premultiplying the summation causes the entire term to go to zero at large R; i.e.,

$$\Delta V_{\rm ad}^{\rm A}(R = \infty) \;=\; u_\infty^{\rm A} \quad . \tag{3.44}$$

This means that

$$\Delta V_{\rm ad}^{\alpha}(R = R_e) \;=\; \frac{\Delta M_{\rm A}^{\alpha}}{M_{\rm A}^{\alpha}}\, u_0^{\rm A} + \frac{\Delta M_{\rm B}^{\alpha}}{M_{\rm B}^{\alpha}}\, u_0^{\rm B} \quad , \tag{3.45}$$

and

$$\Delta V_{\rm ad}^{\alpha}(R = \infty) \;=\; \frac{\Delta M_{\rm A}^{\alpha}}{M_{\rm A}^{\alpha}}\, u_\infty^{\rm A} + \frac{\Delta M_{\rm B}^{\alpha}}{M_{\rm B}^{\alpha}}\, u_\infty^{\rm B} \quad , \tag{3.46}$$

where $\Delta V_{\rm ad}^{\alpha}(R = R_e)$ represents the molecular isotope shift of the electronic energy T_e, and

$\Delta V_{\rm ad}^{\alpha}(R=\infty)$ is the atomic isotope shift. The most natural choice for the zero of energy of a given molecular system is the energy of isolated ground state atoms at infinite distance. As a result, $\Delta V_{\rm ad}^{(\alpha)}(R=\infty)=0$ if the given state dissociates to ground state atoms.

The non-adiabatic centrifugal BOB correction function is expanded in a similar form as

$$q_{\rm A}(R) \;=\; q_0^{\rm A}\left(\frac{2{R_e}^p}{R^p+{R_e}^p}\right)+q_\infty\left(\frac{R^p-{R_e}^p}{R^p+{R_e}^p}\right)+\left(\frac{2{R_e}^p}{R^p+{R_e}^p}\right)\sum_{i=1}q_i^{\rm A}\left(\frac{R^p-{R_e}^p}{R^p+{R_e}^p}\right)^i \quad . \quad (3.47)$$

For $q_{\rm A}(R)$, nothing is known about its long-range behaviour, so there is no need to introduce the separate power m which appeared in the $\Delta V_{\rm ad}^{\rm A}(R)$ function, and consequently a common power p is used in all terms. As above, setting $p>1$ forces the $q^{\alpha}(R)$ function to approach its limit more rapidly beyond the data range. The constraint that $q^{\alpha}(R\rightarrow\infty)=0$ is readily introduced simply by requiring that $q_\infty^{\rm A}=q_\infty^{\rm B}=0$, while $q_{\rm A}(R=R_e)=q_0^{\rm A}$. Moreover, if properties related to $q_{\rm A}(R=R_e)$ are not known [73, 74], we adopt the convention proposed by Watson [31] and require $q_{\rm A}(R=R_e)=0$. This is achieved simply by setting $q_0^{\rm A}=q_0^{\rm B}=0$.

3.3 Λ-doubling and the Effective Schrödinger Equation

The radial Schrödinger equation, Eq.(3.38), is not complete if the given electronic state is not a Σ state, since Λ-doubling occurs when quantum number $\Lambda\neq 0$. This effect is especially significant for high-J levels. For $^1\Pi$ state, the level splitting due to Λ-doubling in a first-order approximation is usually expressed in a band-constant representation as [21, 23]

$$\delta E_\Lambda^{e,f} \;=\; \pm\frac{1}{2}\,q_v\times[J(J+1)-\Omega^2] \quad (3.48)$$

where the + and − signs refer to e and f parity levels, respectively. If the Λ-doubling parameter q_v is a smooth function of the vibrational quantum number v, one may treat q_v as the expectation values of some radial strength function, $(\hbar^2/2\mu\,R^2)f_\Lambda(R)$ [75],

$$q_v \;=\; \langle v,\,J|\frac{\hbar^2}{2\mu\,R^2}\,f_\Lambda(R)|v,\,J\rangle \quad , \quad (3.49)$$

where $f_\Lambda(R)$ may be expanded as a power series in $y_p(R)$,

$$f_\Lambda(R) \;=\; \sum_{i=0}^{N} l_i \, {y_p}^i \;=\; \sum_{i=0}^{N} l_i \left(\frac{R^p - {R_e}^p}{R^p + {R_e}^p} \right)^i \quad , \tag{3.50}$$

where $\{l_i\}$ are the expansion parameters. The $f_\Lambda(R)$ radial strength function is included as an additional potential term in the effective radial Schrödinger equation

$$\left\{ -\frac{\hbar^2}{2\mu_\alpha} \frac{d^2}{dR^2} \;+\; \frac{\hbar^2 \left[J(J+1) - \Omega^2 \right]}{2\mu_\alpha \, R^2} \left[1 + q^{(\alpha)}(R) \pm f_\Lambda(R) \right] \;+\; \left[V(R) + \Delta V_{\rm ad}^{(\alpha)}(R) \right] \right\} \psi_{v,J}(R)$$
$$= \; E_{v,J} \, \psi_{v,J}(R) \quad . \tag{3.51}$$

The above expression is the version of the effective radial Schrödinger equation for a diatomic molecule which has been implemented in the current version of the computer program DSPotFit.

Chapter 4

The $B\,^1\Pi_u$ State of The Lithium Dimer

In the present chapter, the new potential function models and BOB correction function forms described in Chapter 3 are utilized in an analysis of extensive high resolution data for the $B\,^1\Pi_u$ state of Li_2 molecule.

4.1 Previous Work on the $B\,^1\Pi_u$ State of Li_2

Of all homonuclear diatomic molecules, Li_2 is the least complex stable molecule that possesses an electron core, and it has been of interest theoretically [76, 77, 78, 79, 80, 81] and experimentally [38, 82, 83, 84, 85, 86, 87] for decades. The $B\,^1\Pi_u$ state of Li_2 is well-known for a potential barrier caused by a competition between the long-range repulsive dipole-dipole interaction and the electron exchange interaction [80, 84]. A major contribution to the spectroscopic study of the $B\,^1\Pi_u$ state is due to Hessel and Vidal [84], who measured high resolution fluorescence spectra of $B\,^1\Pi_u \rightarrow X\,^1\Sigma_g^+$ transitions, and determined the molecular constants using Dunham analysis and a quantum mechanical potential obtained from a direct-potential-fit anal-

ysis based on the polynomial-corrected IPA approach [40]. [1] They predicted a potential barrier height of $450\pm50\,\mathrm{cm}^{-1}$. Later, Russier *et al.* [3] observed high resolution Fourier transform spectra of the $F\,^1\Sigma_g^+ \rightarrow B\,^1\Pi_u$ fluorescence of all three isotopomers $^{7,7}\mathrm{Li}_2$, $^{6,7}\mathrm{Li}_2$ and $^{6,6}\mathrm{Li}_2$, including the transitions to the last vibrational level of $B\,^1\Pi_u$ state ($v = 17$ for $^{7,7}\mathrm{Li}_2$, $v = 16$ for $^{6,7}\mathrm{Li}_2$ and $v = 15$ for $^{6,6}\mathrm{Li}_2$) below the barrier maximum. They modeled the potential curve in the barrier region by joining an RKR curve to an *ab initio* long-range potential [80], and determined a barrier height of $500\pm2\,\mathrm{cm}^{-1}$. In a very recent study of $B\,^1\Pi_u$ state of Li_2, Bouloufa *et al.* [2] measured $B\,^1\Pi_u \leftarrow X\,^1\Sigma_g^+$ transitions of $^{7,7}\mathrm{Li}_2$ with higher resolution, including the quasibound levels. These measurements were combined with the data from Hessel and Vidal [84] and Russier *et al.* [3] to generate a full potential energy function for this system using the spline-pointwise IPA approach. [2] Their fitted potential has a barrier height that is in agreement with the result obtained by Russier *et al.* [3]. Their potential was then used to predict tunneling predissociation line widths [2].

The obvious drawbacks of a pointwise potential are a propensity for high "interpolation noise" [3] and a limited extrapolation ability. These are the general reasons why a well-behaved analytical potential function is to be preferred. As is well known, Li_2 is a relatively "light" (i.e., small reduced mass) molecule, so that effects due to Born-Oppenheimer breakdown are expected to be significant. The IPA analysis described above did not incorporate non-adiabatic corrections to the Hamiltonian. Moreover, the above fits included only 658 levels of f parity from isotopomer $^{7,7}\mathrm{Li}_2$ with $v \leq 16$, even though experimental data were available for all three isotopomers. The Bouloufa *et al.* [2] analysis also ignores the observed Λ-doubling splitting, and their computer program was unable to fit to the level-width data.

In the present chapter, the DELR analytical potential function was fitted to all available isotopomeric data and to the tunneling predissociation line-width data for the $\mathrm{B}\,^1\Pi_u$ state of Li_2 using the analytical DPF method. A complete Hamiltonian incorporating the analytical potential function, adiabatic and non-adiabatic Born-Oppenheimer breakdown correction functions, and a

[1] Described in Chapter 2.

[2] See Chapter 2.

[3] Interpolation noise can be defined as the uncertainty in a function due to the choice of interpolation method.

Λ-doubling radial strength function was used in the fits. Finally, a critical comparison of the most recently published pointwise potential [2] with the current fitted analytical potential is made.

4.2 Fitting Results and Analysis

The DELR potential energy function of Eqs.(3.29) and (3.34) with $p = 3$, BOB adiabatic and non-adiabatic correction functions of Eqs.(3.42) and (3.47) with $m = p = 3$, and the Λ-doubling radial strength function of Eq.(3.50) with $p = 3$ were fitted to the experimental data for the $B\,^1\Pi_u \leftarrow X\,^1\Sigma_g^+$ transitions and to the tunneling predissociation line widths for the $B\,^1\Pi_u$ state, using the program DSPotFit. The explicit expansion for Eq.(3.34) in this case is written as

$$V_{\rm LR}(R) \;=\; \frac{C_3}{R^3}{\rm D}_3(R) + \frac{C_6}{R^6}{\rm D}_6(R) + \frac{C_8}{R^8}{\rm D}_8(R) + \ldots \quad , \tag{4.1}$$

where the values of C_3, C_6 and C_8 were taken from Ref. [3] and held fixed in the fits. The damping function scaling factor ρ_x for this system is 0.5397.

There are 3228 available data up to the last vibrational level ($v = 17$ for isotopomer $^{7,7}{\rm Li}_2$, $v = 16$ for $^{6,7}{\rm Li}_2$, and $v = 15$ for $^{6,6}{\rm Li}_2$). Among them, 3163 data are transition frequencies for both e and f parity, obtained from the Hessel and Vidal [84] high resolution $B\,^1\Pi_u \rightarrow X\,^1\Sigma_g^+$ transitions for $^{7,7}{\rm Li}_2$, the Russier *et al.* [3] Fourier transform data for $^{7,7}{\rm Li}_2$, $^{6,7}{\rm Li}_2$ and $^{6,6}{\rm Li}_2$, and the Bouloufa *et al.* [2] recent experiments on $^{7,7}{\rm Li}_2$; the other 65 data are line widths for the $^{7,7}{\rm Li}_2$ and $^{6,6}{\rm Li}_2$ isotopomers. The experimental data are summarized in Table 4.1.

Isotopomer	Transition	#Lines e	#Lines f	*Unc.* /cm^{-1}	Range	#Widths e	#Widths f	Source
$^{7,7}{\rm Li}_2$	$B\,^1\Pi_u \rightarrow X\,^1\Sigma_g^+$	350	701	0.005	$v' = 0$–4	–	–	Ref. [84]
	$F\,^1\Sigma_g^+ \rightarrow B\,^1\Pi_u$	137	113	0.01	$v'' = 5$–16	–	–	Ref. [3]
	$B\,^1\Pi_u \leftarrow X\,^1\Sigma_g^+$	342	177	0.002	$v' = 5$–12	49	–	Ref. [2]
$^{6,7}{\rm Li}_2$	$F\,^1\Sigma_g^+ \rightarrow B\,^1\Pi_u$	186	97	0.005	$v'' = 0$–16	–	–	Ref. [3]
$^{6,6}{\rm Li}_2$	$F\,^1\Sigma_g^+ \rightarrow B\,^1\Pi_u$	690	370	0.005	$v'' = 0$–15	12	4	Ref. [3]

Table 4.1: Summary of the observed data for the $B\,^1\Pi_u$ state of Li_2. The estimated experimental uncertainties for the widths are ca. $\pm 10\%$ of the line widths themselves.

After some experimentation, it was found that use of a 9^{th} order polynomial expansion for the DELR exponent variable $\beta(y_3)$ yielded a fit of fairly good quality. The RMSR value for the fit to the transition frequencies is approximately unity (RMSR = 1.039): the fitted analytical potential reproduces the observed transition frequencies within the experimental uncertainties. However, as shown in the upper segment of Fig. 4.1, the potential curve misbehaves at short range in spite of the use of the $p = 3$ expansion variable because the $\beta(y_3)$ function required for the $B\,^1\Pi_u$ state potential is a high-order polynomial that leads to unphysical behaviour in the short-range region. For this reason, the second strategy discussed in Section 3.1.7 was employed here. Different combinations of $\{N_S, N_L\}$, from {9,9}, {8,9}, {7,9},{6,9}, {5,9}, {4,9} to {3,9} respectively, have been investigated. Note that {3,9}, for example, means the first 4 terms (β_0 to β_3) of the $\beta(y_p)$ polynomial are used for $R < R_e$, but the complete 10-term polynomial (β_0 to β_9) is employed for $R \geq R_e$.

The results show that various combinations of N_S and N_L give approximately the same overall quality fit. As for the {9,9} case shown in the upper segment of Fig. 4.1, the potential curves for {8,9} and {7,9} turn over at short range, while the {6,9} curve shows negative curvature at small distances. However, with decreasing N_S, the unphysical behaviour in the inner wall of the potential gradually disappears, and for $N_S \leq 5$ no spurious behaviour occurs. As shown in the bottom frame of Fig. 4.1, the potential curve for {3,9} behaves well at both long and short ranges. The solid part of the curve seen there represents the region covered by experimental data, whereas the dotted curve segments represent extrapolation using the analytical form of the potential.

Potential parameters for the two extreme cases {9,9} and {3,9} are listed in Table 4.2. The numbers in parentheses are the 95% confidence limit uncertainties in the last significant digit shown. The second and third columns are the results of fits to transition frequencies alone, and the fourth and fifth columns are those for fits to all the available data, including the line widths. The values of RMSR(total) represent the overall quality of the fit; the RMSR(freq.) are the values for frequency data alone, while RMSR(width) are the values calculated from width data alone. Note that in the {3,9} $\beta(y_3)$ function, coefficients for powers greater than $N_S = 3$ become dramatically different from those in the {9,9} function, since the higher-order terms are no longer

	Fit to frequencies only		Fit to frequencies and widths	
Parameter	{9,9}	{3,9}	{9,9}	{3,9}
$\mathfrak{D}_e$ / cm^{-1}	2984.42	2984.42	2984.42	2984.42
R_e / Å	2.93680983(22000)	2.93686252(22000)	2.93680407(24000)	2.93686249(24000)
β_0 / Å^{-1}	0.96121319(2500)	0.96116997(2000)	0.96121285(28000)	0.96117023(2200)
β_1 / Å^{-1}	0.2078317(3700)	0.2092093(3400)	0.2078334(4100)	0.2092053(3600)
β_2 / Å^{-1}	0.1741428(3500)	0.1708886(11000)	0.1741386(3800)	0.1708656(12000)
β_3 / Å^{-1}	0.178603(2200)	0.13659(310)	0.178559(2400)	0.136537(3400)
β_4 / Å^{-1}	0.070563(3000)	0.50868(4600)	0.070655(3300)	0.51335(5000)
β_5 / Å^{-1}	0.04358(1700)	-1.76847(2700)	0.04391(1800)	-1.8031(3000)
β_6 / Å^{-1}	0.3177(210)	4.303(840)	0.3168(230)	4.4172(9200)
β_7 / Å^{-1}	-0.1247(440)	-5.003(1400)	-0.1253(480)	-5.199(1500)
β_8 / Å^{-1}	-1.351(90)	1.774(1200)	-1.348(98)	1.945(1300)
β_9 / Å^{-1}	0.952(48)	0.14(41)	0.950(52)	0.08(44)
u_0 / cm^{-1}	0.0	0.0	0.0	0.0
u_1 / cm^{-1}	2.807(1500)	2.715(1600)	2.743(1700)	2.717(1700)
u_2 / cm^{-1}	-2.94(120)	-3.03(130)	-2.89(130)	-3.03(140)
u_∞ / cm^{-1}	0.046(180)	0.109(190)	0.053(200)	0.108(200)
q_0	0.000299(73)	0.00031(7)	0.000297(79)	0.00031(8)
q_1	0.000073(70)	0.000203(67)	0.000073(77)	0.000203(73)
q_2	-0.002229(690)	-0.003625(650)	-0.00223(75)	-0.00362(71)
q_3	-0.00134(40)	-0.00227(36)	-0.00135(44)	-0.00228(39)
q_4	0.02907(370)	0.03687(350)	0.02908(410)	0.03688(380)
q_5	-0.0305(33)	-0.0364(31)	-0.0305(36)	-0.0364(34)
q_∞	0.0	0.0	0.0	0.0
l_0	0.00017981(320)	0.0001793(33)	0.0001798(35)	0.00017933(360)
l_1	-0.0003099(560)	-0.0003024(570)	-0.0003094(610)	-0.0003033(620)
l_2	0.000371(68)	0.000384(70)	0.00037(7)	0.000385(76)
l_3	-0.001691(400)	-0.001756(410)	-0.001693(440)	-0.001756(450)
l_4	0.00381(70)	0.00375(72)	0.00382(77)	0.00375(78)
l_5	-0.00254(68)	-0.00238(70)	-0.00255(75)	-0.00238(76)
# data	3163	3163	3228	3228
RMSR(total)	1.039	1.062	1.135	1.157
RMSR(freq.)	1.039	1.062	1.039	1.062
RMSR(width)	2.103	2.123	2.098	2.096

Table 4.2: Potential parameters and fitting quality for the $B\,^1\Pi_u$ state of Li_2. $\mathfrak{D}_e$ is taken from Bouloufa *et al.* [2].

required to remain "well-behaved" for $R < R_e$, and need only describe the potential for $R \geq R_e$. The uncertainties of the coefficient β_9 in the {3,9} $\beta(y_3)$ function is greater than 100%, which means this parameter is not needed to achieve this quality of fit. Thus, the separate-power $\beta(y_p)$ function could lead to fewer β coefficients required for the fit.

The upper part of Fig. 4.2 shows the $\beta(y_p)$ functions for the {9,9}, {5,9} and {3,9} potentials. The functions for both $\beta(y_p)$ functions for {5,9} and {3,9} are well-behaved in the whole domain of the y_p variable, but the {9,9} curve plunges into the negative regime at small distances. As has been discussed in Section 3.1.5, negative values of the $\beta(R)$ function would cause pathological behaviour of a potential curve.

Because the variable $y_{p=3} \equiv y_3 = (R^3 - {R_e}^3)/(R^3 + {R_e}^3)$ is used instead of $y_1 = z = (R - R_e)/(R + R_e)$, the power $p = 3$ forces the $\beta(R)$ function to approach its asymptotic limit more rapidly. As shown in Fig. 4.2, the $\beta(R)$ functions for all $\{N_S, N_L\}$ cases smoothly approach a long-range limit without having implausible extrema beyond the experimental data region [18]. The bottom part of Fig. 4.2 shows the resulting overall potential, to indicate the radial scale. [4]

The RMSR of the width data used in the fit to determine the potential function is about 2.1. The calculated line widths of the quasibound levels are listed in Table 4.3, where $\Gamma_{calc.}$ are the widths calculated from the fitted potential and $\Gamma_{obs.}$ are the observed width values obtained from Ref. [2]. The energy $E_{v,J}$ is expressed relative to the asymptote of the B state. The last column shows the ratios of the differences $(\Gamma_{calc.} - \Gamma_{obs.})$ to the estimated experimental uncertainties (*Unc.*). It is clear that the magnitude of the root mean square of these values, RMSR(width) in Table 4.2, is heavily dependent on the large relative discrepancies for a handful of levels for which the widths are very small (see the bold values at the top of the Table). Doubling the uncertainties of the widths associated with the first five levels in the Table 4.3 would reduce RMSR(width) to only 1.4. This suggests that the estimated 10% uncertainty may be somewhat optimistic for the narrow levels.

Both Λ-doubling and Born-Oppenheimer breakdown effects are significant for the $B\,^1\Pi_u$ state of Li_2. Here we need to determine what orders should be used for the polynomial functions of

[4] The logarithmic abscissa scale is used in the plots to facilitate the view of the short-range region and the behaviour of the function at long-range.

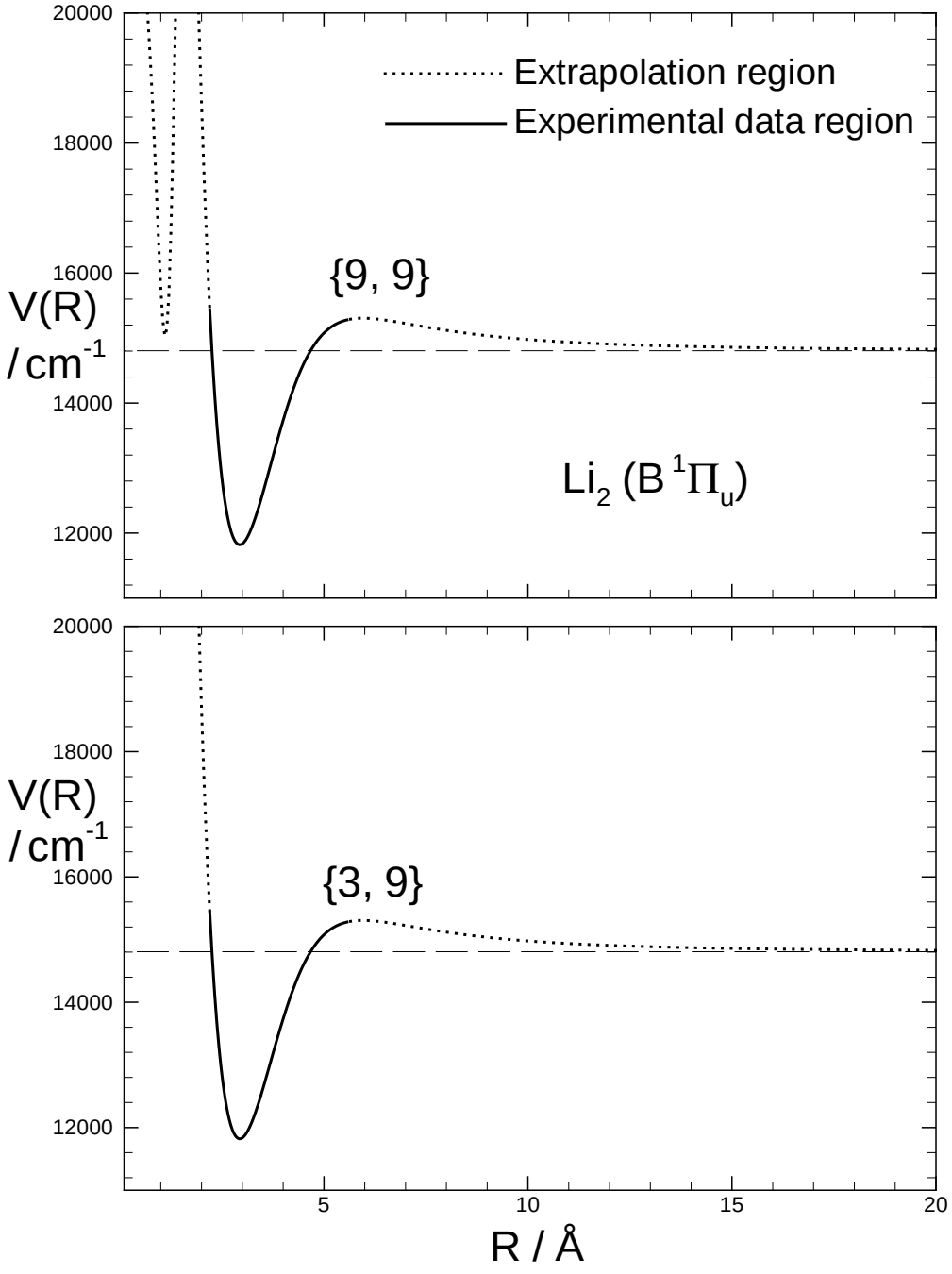

Figure 4.1: Plots of DELR potential curves with $\{N_S, N_L\} = \{9,9\}$ and $\{3,9\}$ for the $B\,^1\Pi_u$ state of Li_2.

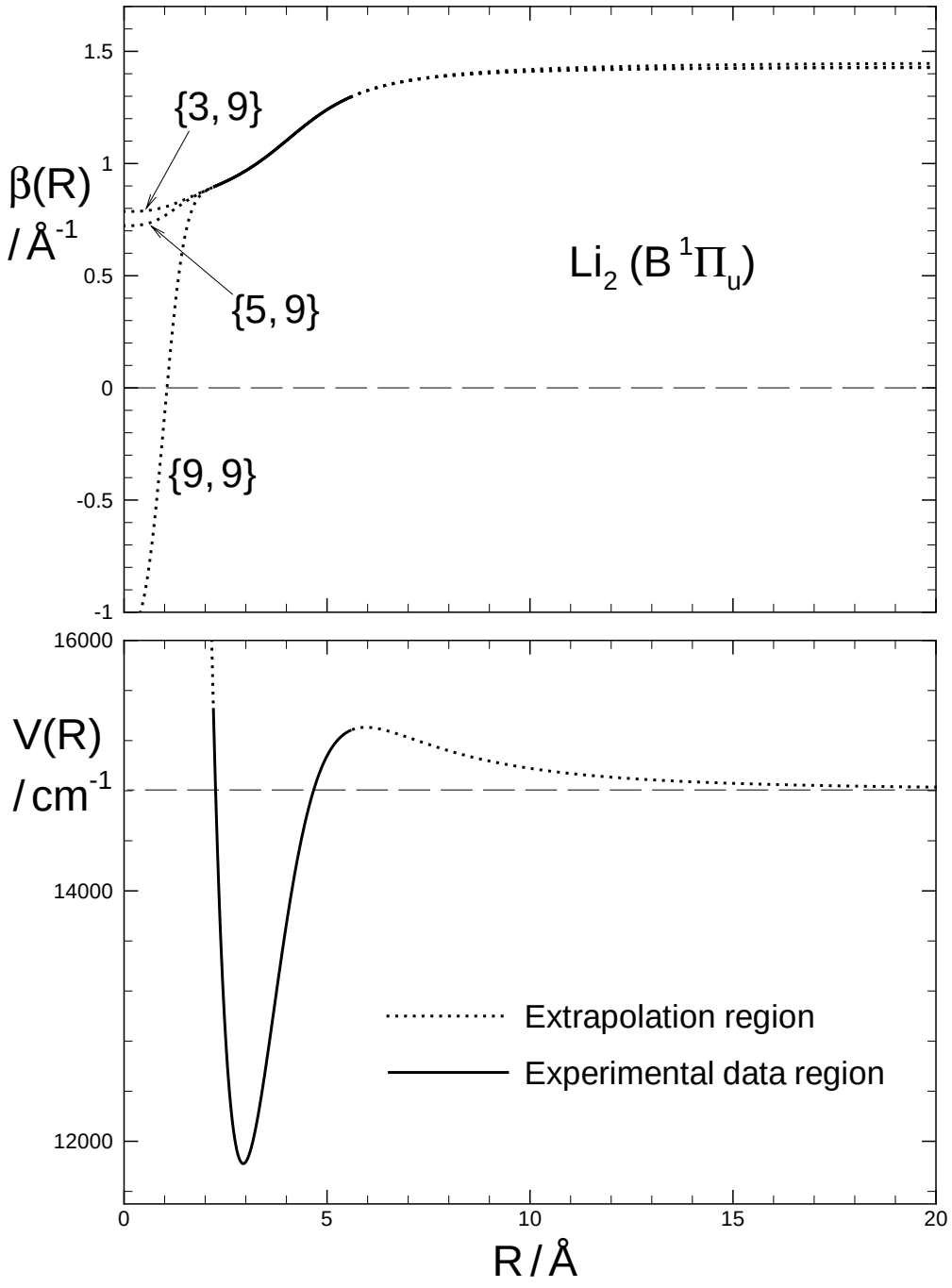

Figure 4.2: The upper panel shows plots of $\beta(y_3)$ functions for $\{N_S, N_L\} = \{9,9\}$, $\{5,9\}$ and $\{3,9\}$, while the bottom panel shows the DELR potential for the $B\,^1\Pi_u$ state of Li_2.

v	J	$E_{v,J}$	$\Gamma_{calc.}$	$\Gamma_{obs.}$	$Unc.$	$(\Gamma_{calc.}-\Gamma_{obs.})/Unc.$
11	54	806.917	5.9431×10^{-5}	9.5×10^{-5}	9.5×10^{-6}	**-3.74**
11	56	879.373	3.0493×10^{-3}	1.7×10^{-3}	1.7×10^{-4}	**7.94**
12	49	748.806	3.6663×10^{-4}	1×10^{-4}	5.0×10^{-5}	**5.33**
13	41	622.357	2.4804×10^{-5}	3.4×10^{-5}	3.4×10^{-6}	**-2.70**
13	43	677.024	8.3506×10^{-4}	5×10^{-4}	5.0×10^{-5}	**6.70**
13	44	704.614	4.2869×10^{-3}	4.0×10^{-3}	5.0×10^{-4}	0.57
13	45	732.266	2.0133×10^{-2}	2.14×10^{-2}	2.1×10^{-3}	-0.59
13	46	759.860	8.5662×10^{-2}	0.100	1.0×10^{-2}	-1.43
14	35	581.225	3.1000×10^{-4}	3.3×10^{-4}	3.3×10^{-5}	-0.61
14	36	603.736	1.3674×10^{-3}	1.5×10^{-3}	1.5×10^{-4}	-0.88
14	37	626.494	5.6949×10^{-3}	5.9×10^{-3}	5.9×10^{-4}	-0.35
14	38	649.430	2.2249×10^{-2}	2.43×10^{-2}	2.4×10^{-3}	-0.84
14	39	672.451	8.0817×10^{-2}	7.9×10^{-2}	7.9×10^{-3}	0.23
15	25	492.066	1.0806×10^{-4}	1.1×10^{-4}	1.1×10^{-5}	-0.18
15	26	508.266	3.5744×10^{-4}	4.3×10^{-4}	4.3×10^{-5}	-1.69
15	27	524.889	1.1633×10^{-3}	1.3×10^{-3}	1.3×10^{-4}	-1.05
15	28	541.901	3.7067×10^{-3}	3.7×10^{-3}	3.7×10^{-4}	0.02
15	29	559.259	1.1493×10^{-2}	1.18×10^{-2}	1.2×10^{-3}	-0.26
15	30	576.909	3.4456×10^{-2}	3.7×10^{-2}	3.7×10^{-3}	-0.69
15	31	594.783	9.9031×10^{-2}	0.109	1.1×10^{-2}	-0.92
16	10	424.286	1.2101×10^{-4}	1.1×10^{-4}	1.1×10^{-5}	1.00
16	11	431.040	2.0837×10^{-4}	1.9×10^{-4}	1.9×10^{-5}	0.97
16	12	438.367	3.7163×10^{-4}	4.3×10^{-4}	4.3×10^{-5}	-1.36
16	13	446.257	6.8420×10^{-4}	7.8×10^{-4}	7.8×10^{-5}	-1.23
16	14	454.697	1.2956×10^{-3}	1.7×10^{-3}	1.7×10^{-4}	-2.38
16	15	463.670	2.5140×10^{-3}	3.7×10^{-3}	3.7×10^{-4}	-3.21
16	16	473.160	4.9782×10^{-3}	5.9×10^{-3}	5.9×10^{-4}	-1.56
16	17	483.146	1.0016×10^{-2}	1.11×10^{-2}	1.1×10^{-3}	-0.98
16	18	493.605	2.0381×10^{-2}	2.55×10^{-2}	2.6×10^{-3}	-2.01
16	19	504.509	4.1726×10^{-2}	4.2×10^{-2}	4.2×10^{-3}	-0.07
16	20	515.823	8.5461×10^{-2}	7.9×10^{-2}	7.9×10^{-3}	0.82
16	21	527.509	0.1739	0.180	1.8×10^{-2}	-0.34
16	22	539.518	0.3494	0.33	3.3×10^{-2}	0.59
16	23	551.800	0.6871	0.70	7.0×10^{-2}	-0.18
16	24	564.306	1.3112	1.3	1.3×10^{-1}	0.09
16	25	577.006	2.4064	2.6	2.6×10^{-1}	-0.74
16	26	589.892	4.1794	4	4.0×10^{-1}	0.45
16	27	602.864	6.3205	8	8.0×10^{-1}	-2.10
17	1	478.162	0.7106	0.80	8.0×10^{-2}	-1.12
17	2	479.192	0.7535	0.91	9.1×10^{-2}	-1.72
17	3	480.732	0.8220	0.85	8.5×10^{-2}	-0.33
17	4	482.777	0.9214	1.1	1.1×10^{-1}	-1.62
17	5	485.320	1.0600	1.1	1.1×10^{-1}	-0.36
17	6	488.352	1.2490	1.2	1.2×10^{-1}	0.41
17	7	491.866	1.5045	1.4	1.4×10^{-1}	0.75
17	8	495.846	1.8471	1.9	1.9×10^{-1}	-0.28
17	9	500.282	2.3042	1.9	1.9×10^{-1}	2.13
17	11	510.482	3.7004	3.6	3.6×10^{-1}	0.28
17	12	516.221	4.6913	4.6	4.6×10^{-1}	0.20

Table 4.3: Comparison of the calculated and observed widths for the $B\,^1\Pi_u$ state of $^{7,7}Li_2$.

Eqs.(3.50) and (3.47), and how the resulting functions behave. The coefficient $u_0^{\rm Li}$ in the adiabatic BOB correction function as defined in Eq.(3.42) has been set to zero, because the data are not extensive enough to allow us to determine the molecular isotope shift $\Delta V_{\rm ad}^{\alpha}(R = R_e)$, as specified in Eq.(3.45), while both $u_\infty^{\rm Li}$ and $q_0^{\rm Li}$ can be determined from the fits. Table 4.4 lists the quality of fit obtained for different orders of Λ-doubling radial strength functions and BOB correction functions. The best quality fit was obtained for polynomials of order 5 for both the $f_\Lambda(R)$ and $q(R)$ functions, and of order 2 for the $\Delta V_{\rm ad}^{\rm Li}(R)$ function. However, the $q(R)$ curve oscillates, as shown in the upper segment of Fig. 4.3, when a polynomial function of order 5 is used. The oscillation is an implausibly irregular shape that suggests the high-order $q(R)$ function may have been fitted to noise. It can be seen from the table that the quality of fit is much worse without inclusion of either $f_\Lambda(R)$ or $q^{\rm Li}(R)$; however, beyond order of 2 for both the $f_\Lambda(R)$ and $q^{\rm Li}(R)$ functions, the quality of fit does not improve too much, and the resulting functions begin to show implausible irregularities.

Polynomial Order for Functions			
$f_\Lambda(R)$	$q^{\rm Li}(R)$	$\Delta V_{\rm ad}^{\rm Li}(R)$	RMSR
–	5	2	13.41
0	5	2	1.653
1	5	2	1.464
2	5	2	1.089
3	5	2	1.075
4	5	2	1.061
5	5	2	1.056
5	–	2	1.248
5	0	2	1.196
5	1	2	1.165
5	2	2	1.158
5	3	2	1.147
5	4	2	1.122
5	5	2	1.056

Table 4.4: Quality of fits for various orders of Λ-doubling radial strength functions and BOB correction functions for the $B\,^1\Pi_u$ state of Li_2 using a $\{5,9\}$ $\beta(y_3)$ function; these test fits consider only transition frequency data.

Figs. 4.3 and Fig. 4.4 show the fitted Λ-doubling radial strength function and the non-adiabatic and adiabatic BOB correction functions. As was discussed in Section 3.2, the $q(R)$ functions

approach zero at the dissociation limit, since q_∞ was set to zero. The $q(R)$ function for order 2 yields a curve which does not oscillate and behaves well on the whole interval. These $f_\Lambda(R)$ and $\Delta V_{\rm ad}(R)$ functions are also smooth, and plausibly approach small constant values at long range.

Among the well-behaved potential curves for $\{N_S, N_L\} = \{3,9\}$ to $\{5,9\}$, the $\{5,9\}$ curve has the highest order of continuity at $R = R_e$. Together with the consideration of the order of the Λ-doubling and BOB correction functions discussed above, we recommend the $\{5,9\}$ potential and order-2 polynomial functions for the Λ-doubling and both BOB corrections as our optimum representation of the $B\,^1\Pi_u$ state potential of Li_2. The parameters of these recommended functions are listed in Table 4.5. The barrier maximum determined from this fit is located at $R = 5.955$Å with an energy of $15306.17\pm0.02\,{\rm cm}^{-1}$ which gives a barrier height of $500.41\pm0.02\,{\rm cm}^{-1}$. [5] This value is in very good agreement with the one suggested by Russier *et al.* [3], but the present result has lower estimated uncertainty, [6] and thus is more reliable.

4.3 Comparison of Pointwise and Analytical Potentials

As is mentioned above, a "spline-pointwise-potential" (SPP) for the $B\,^1\Pi_u$ state of Li_2 has been obtained by Bouloufa *et al.* [2] using the spline-pointwise IPA approach. However, they fitted to only the 658 data for $^{7,7}Li_2$ involving levels of f parity with $v \leq 16$. To make a comparison between the present fitted analytical potential and the SPP function, the same set of experimental data used for the SPP analysis were fitted to the DELR potential model. In addition, a forward calculation was carried out using the SPP function to allow us to compare the two analyses on an equivalent basis: i.e., the SPP function was used in prediction of the transition frequencies and widths which were then compared with the observed data. The RMSR values for both the SPP function and the fitted analytical DELR potential are shown in Table 4.6. The third and fourth columns of the table shows the results of fits performed using a DELR potential with and without inclusion of the non-adiabatic centrifugal BOB correction, respectively. The SPP

[5] Potential asymptote is $14805.76\,{\rm cm}^{-1}$ [2].

[6] This is the 95% confidence limit uncertainty calculated from parameters uncertainties and correlation matrix [88].

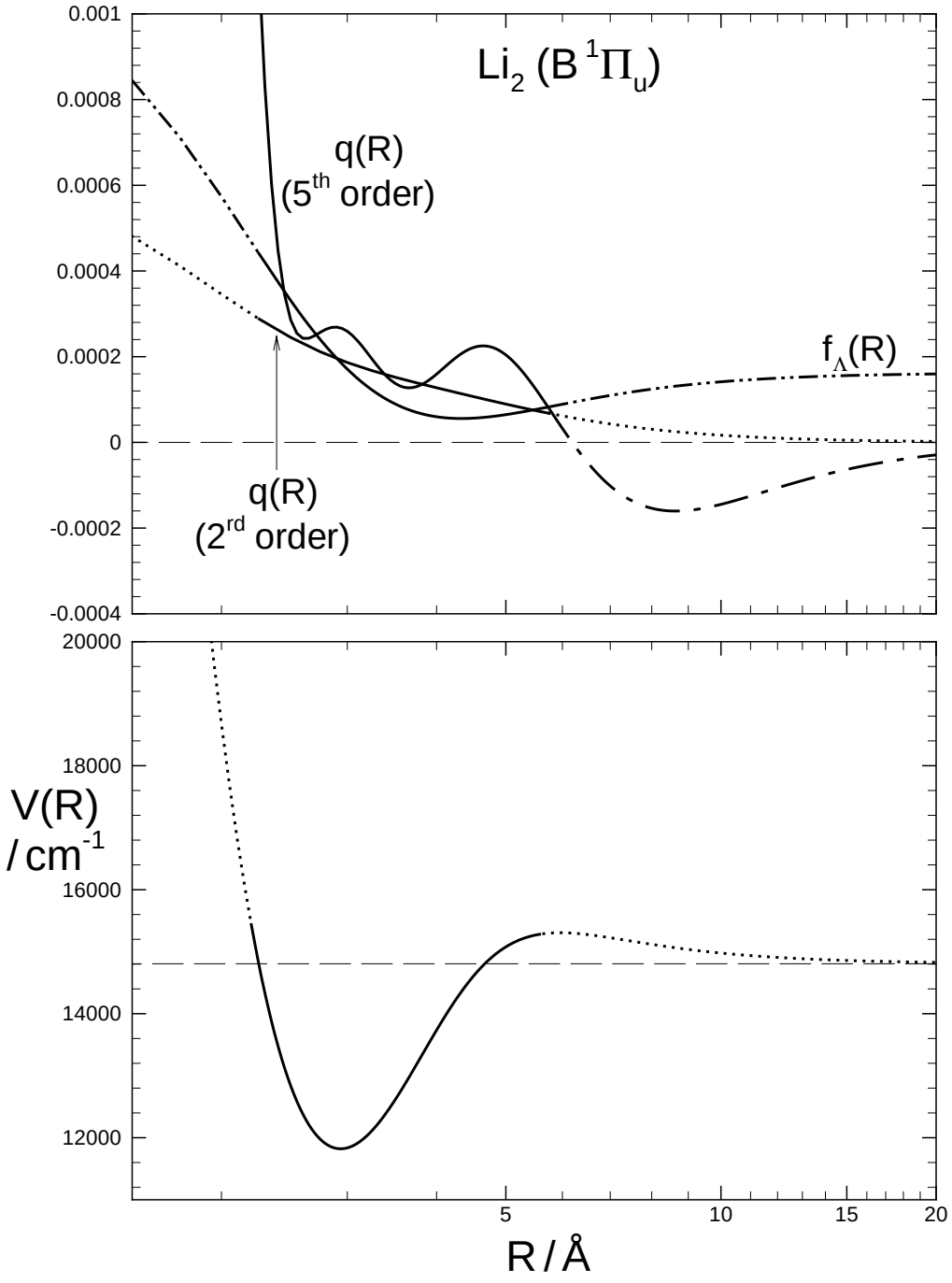

Figure 4.3: The upper panel shows plots of the Λ-doubling and non-adiabatic centrifugal BOB correction functions for the $B\,^1\Pi_u$ state of Li_2; the $f_\Lambda(R)$ function is an order-2 polynomial, and the $q(R)$ functions have orders 2 and 5, respectively. The lower panel shows the overall potential of the B-state of Li_2. The distance variable R is on a logarithmic scale.

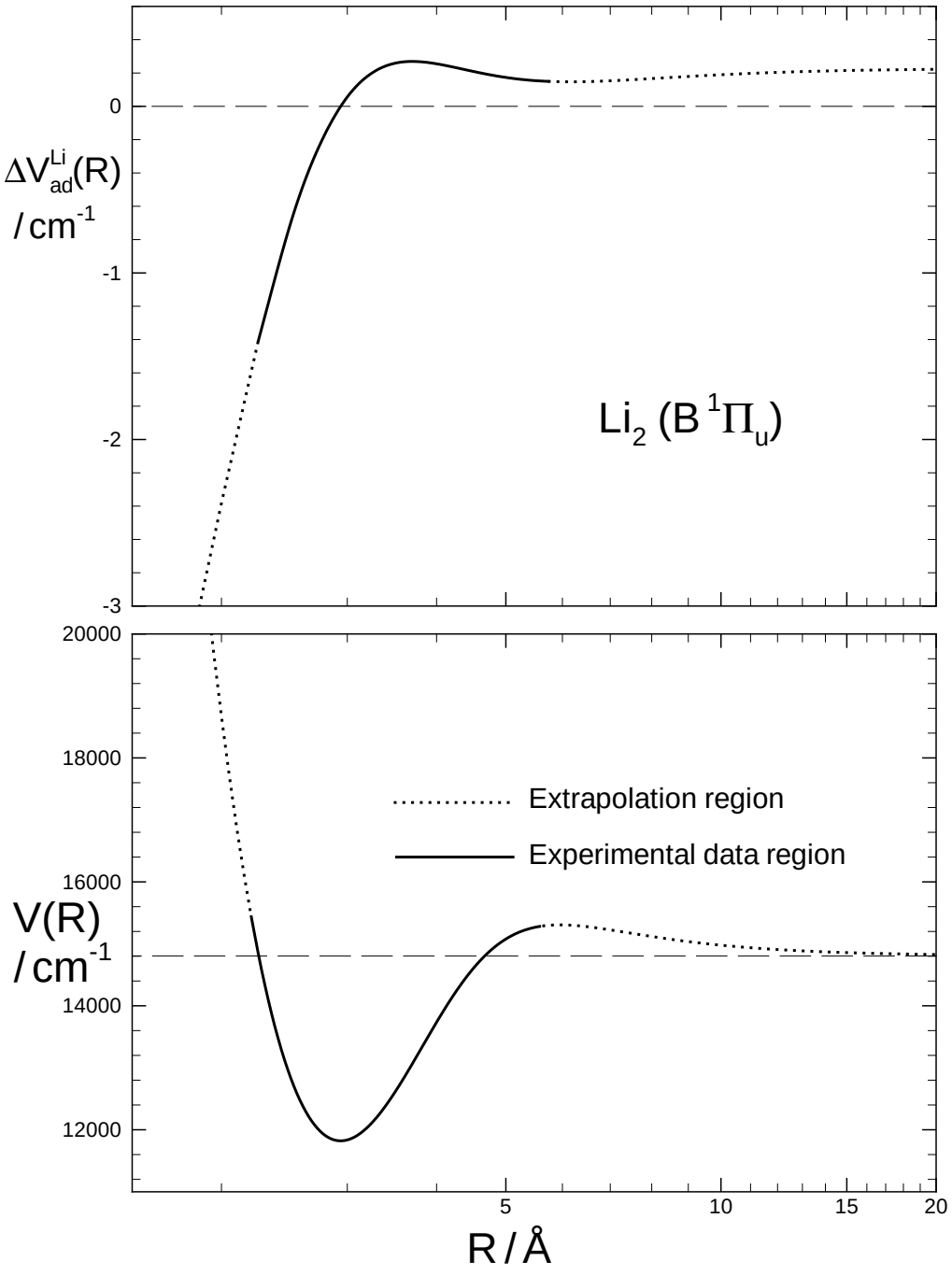

Figure 4.4: The upper panel shows plot of the adiabatic BOB correction function for the $B\,^1\Pi_u$ state Li_2. The lower panel shows the overall potential of the B-state of Li_2. The distance variable R is on a logarithmic scale.

Parameter	{5,9}
$\mathfrak{D}_e$ / cm^{-1}	2984.42
R_e / Å	2.93649296(21000)
A / cm^{-1}	4291.9352
B / cm^{-1}	9766.4646
β_0 / $\mathrm{Å}^{-1}$	0.961289996(2200)
β_1 / $\mathrm{Å}^{-1}$	0.2071496(960)
β_2 / $\mathrm{Å}^{-1}$	0.172301(760)
β_3 / $\mathrm{Å}^{-1}$	0.17522(150)
β_4 / $\mathrm{Å}^{-1}$	0.1187(160)
β_5 / $\mathrm{Å}^{-1}$	0.1793(250)
β_6 / $\mathrm{Å}^{-1}$	-0.98(21)
β_7 / $\mathrm{Å}^{-1}$	2.97539(39000)
β_8 / $\mathrm{Å}^{-1}$	-4.563425(360000)
β_9 / $\mathrm{Å}^{-1}$	2.206(150)
u_0 / cm^{-1}	0.0
u_1 / cm^{-1}	1.65(170)
u_2 / cm^{-1}	-2.337(1300)
u_∞ / cm^{-1}	0.228(210)
q_0	0.0001853(710)
q_1	0.000008(33)
q_2	0.00014(16)
q_∞	0.0
l_0	0.00018654(120)
l_1	-0.0004974(210)
l_2	0.000473(26)
# data	3228
RMSR(total)	1.260
RMSR(freq.)	1.176
RMSR(width)	2.078

Table 4.5: Potential energy and correction function parameters for the B-state of Li_2 obtained using a {5,9} $\beta(y_3)$ function. The fixed coefficients defining $V_{\mathrm{LR}}(R)$ are $C_3 = 1.809 \times 10^5\,\mathrm{cm}^{-1}\,\mathrm{Å}^6$, $C_6 = -7.6 \times 10^6\,\mathrm{cm}^{-1}\,\mathrm{Å}^6$, $C_8 = -18 \times 10^6\,\mathrm{cm}^{-1}\,\mathrm{Å}^6$ and $\rho_x = 0.5397$. These C_n values have been taken from Ref. [3]. A and B determined from $\mathfrak{D}_e$, R_e, β_0 and V_{LR} using Eqs.(3.31) and (3.32). The numbers in parentheses are the 95% confidence limit uncertainties in the last significant digit shown.

function corresponds to the case without a $q(R)$ function. The current fitted analytical potential reproduces the observed data within the experimental uncertainties; however, from the RMSR values the SPP function can be seen to fit the data more than 5 times more poorly.

Another indication of the fitting quality is the ability to predict the tunneling predissociation line widths using the fitted potential. The RMSR value obtained using the fitted analytical potential to predict the line widths, as shown in Table 4.6, has an average of about 2.1, which should be compared with 4.7 for the SPP function.

	IPA SPP function	DELR potential	
f parity	Forward calculation	with $q(R)$	no q(R)
v_{max}	16	16	16
#data	657	657	657
RMSR(fit)	5.42	0.74	1.03
RMSR(width)	4.74	2.06	2.05

Table 4.6: Comparison of the fitting quality of the published spline-pointwise potential and the present fully analytical DELR potential for the $B\,^1\Pi_u$ state of $^{7,7}Li_2$. The RMSR values in the bottom row indicate the ability of these potentials to predict line widths.

The difference between the present analytical potential and the SPP function is shown in Fig. 4.5; there are clearly significant discrepancies between the two potentials, even in the experimental data region. The solid line shows the discrepancies between two potentials; the dotted line shows the 95% confidence limit uncertainty of the analytical potential calculated using parameter uncertainties and the correlation matrix of the fit to the analytical potential. [7]

An often-ignored problem with a pointwise potential is the presence of interpolation noise. No matter what interpolation scheme is used, some interpolation noise can always be expected for a pointwise potential. However, a fully smooth analytical potential function completely avoids this problem. As an example, an EMO_p function with N^{th} order of $\beta(y_p)$ function will be continuous and smooth to all orders if the $\beta(y_p)$ function is not split into two regions. As was discussed in Section 3.1.7, a DELR model with a separate-power $\beta(y_p)$ function is discontinuous only at the single point $R = R_e$, and then only for derivatives of order $(N_S + 2)$ or higher. Thus, for our

[7] See Eq.(7) of Ref. [88].

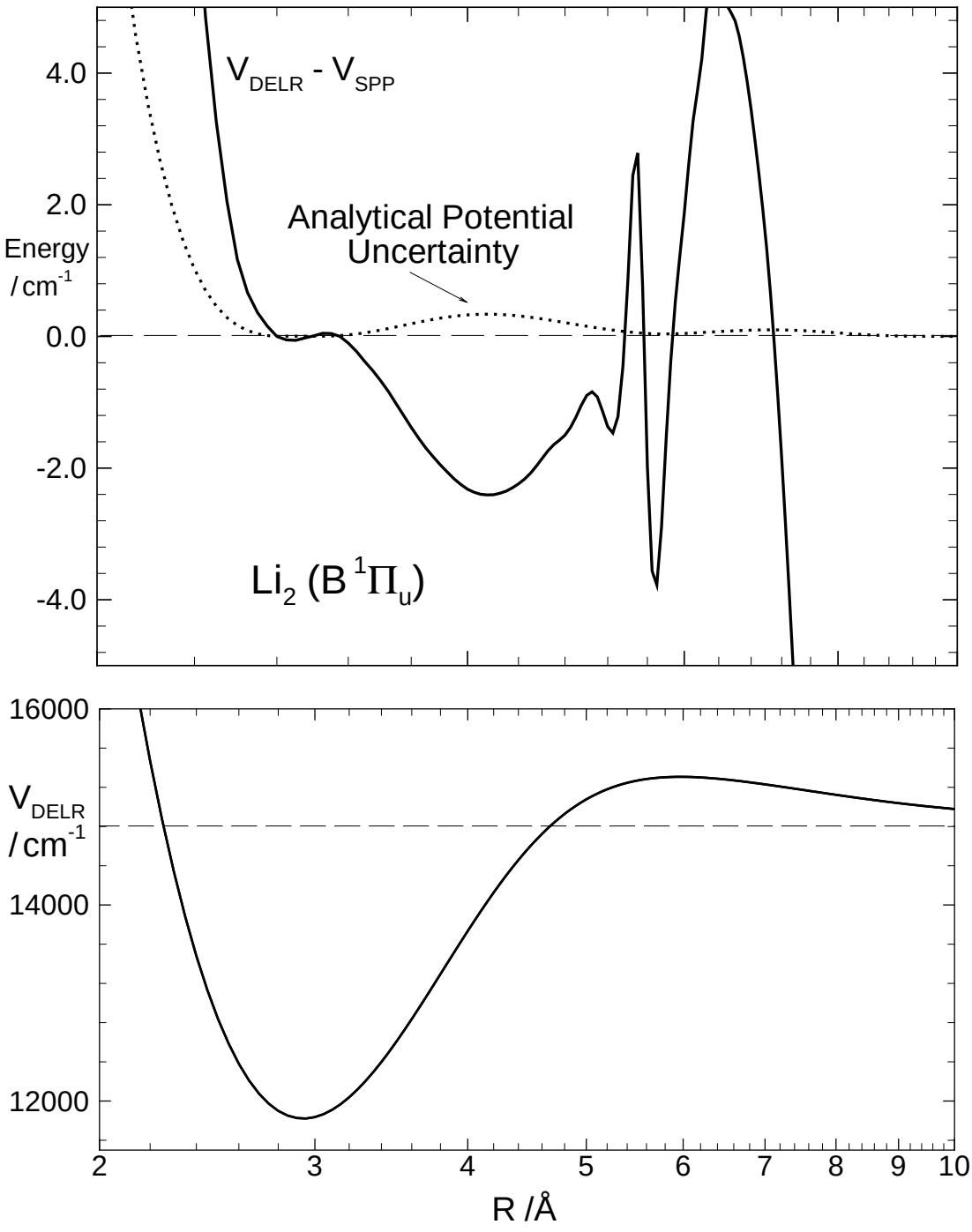

Figure 4.5: The upper frame shows the plot of the difference between the present analytical DELR potential and the published SPP function for the $B\,^1\Pi_u$ state Li_2. The lower frame shows the overall potential of the B-state of Li_2. The distance variable R is on a logarithmic scale.

recommended {5,9} $\beta(y_3)$ function, the potential is discontinuous at only one point ($R = R_e$) for the 7^{th} derivative or higher. However, the third derivative of a SPP function is discontinuous at every internal spline mesh point, and all higher order derivatives do not exist. This lack of high-order smoothness is unphysical, and should be avoided whenever possible.

An interpolation scheme test can demonstrate this problem. Starting from one end of the SPP function, drop each point one at a time, then interpolate for the omitted point using the remaining potential points. For the published SPP function of B-state Li_2, discrepancies between the original known points and the interpolated ones are plotted in Fig. 4.6. Both the spline interpolation and 8-point piecewise polynomial interpolation for the SPP function show high interpolation noise, even in the experimental data region (2.2 - 5.6 Å).

These discussions of the quality of fit and smoothness between the pointwise and analytical potentials show that a fully analytical potential function is generally preferred. However, the SPP function obtained from the spline-pointwise IPA method has more local flexibility than do the existing analytical potential function forms; i.e., the modification of one potential point does not affect the energies of the remaining points of the SPP function during the fitting process. This makes spline-pointwise IPA the method of choice for cases where the potential has significant structure on a small fraction of the overall interval.

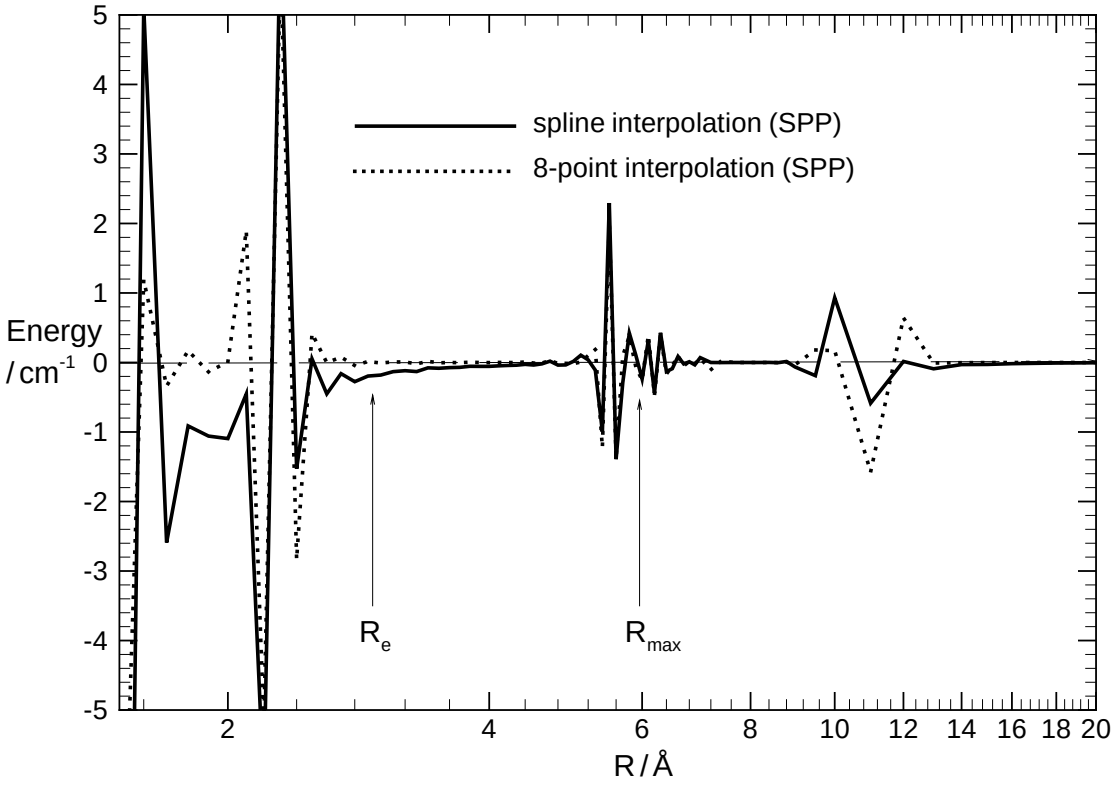

Figure 4.6: Interpolation scheme test for the SPP function for $B\,^1\Pi_u$ state Li_2. The distance variable R is on a logarithmic scale.

Chapter 5

The Ground State of The Beryllium Hydride

BeH is a light heteronuclear diatomic molecule with only five electrons; it has served as an excellent system for testing *ab initio* calculations of electronic structure and properties [89, 90, 91, 92, 93]. Experimentally, the molecule has been known for a long time [94, 95, 96]; however, probably due to the toxicity of Be-containing molecules, detailed studies of BeH and its isotopomers have been undertaken only fairly recently. Major contributions to the experimental study of the BeH isotopic molecular system have been made by Colin and co-workers who have measured the $A\,^2\Pi - X\,^2\Sigma^+$ and $C\,^2\Sigma^+ - X\,^2\Sigma^+$ band systems [97, 98, 99, 100, 101] and transitions of the ground state into various Rydberg states [102, 103]. A systematic analysis of the $X\,^2\Sigma^+$, $A\,^2\Pi$ and $C\,^2\Sigma^+$ states for BeH and BeD has yielded molecular constants of these states [99, 100, 101], and an RKR potential curve of the ground $X\,^2\Sigma^+$ state [100]. Although Born-Oppenheimer breakdown effects for hydrides are expected to be significant due to the small reduced mass, BOB effects for the ground state have yet to be determined, and the best reported potential energy function remains a pointwise RKR curve [100].

From a study of the limiting curve of predissociation, Colin *et al.* [99] concluded that a small potential barrier exists in the ground state rotationless potential. This proposal was supported

by some *ab initio* calculations [89, 90], while other theoretical studies [89, 90, 91, 93] disagreed with this possibility. In this chapter, analytical potential energy functions incorporating BOB correction terms are fitted to experimental data for the $X\,^2\Sigma^+$ state of BeH, BeD and BeT, and an attempt was made to determine whether a barrier exists in the ground state rotationless potential curve. In the first section, the EMO_p potential form with $p = 2$ was fitted to the transition frequencies of the $A\,^2\Pi - X\,^2\Sigma^+$ and $C\,^2\Sigma^+ - X\,^2\Sigma^+$ band systems to obtain a potential energy curve for $X\,^2\Sigma^+$ state. The large deviations of the calculated frequencies from the experimental values for transitions to some high-J levels which are above the dissociation limit may be explained by a barrier in the ground state rotationless potential. To investigate this possibility further, the observed transition frequencies were then fitted to a DELR potential form that allows for a barrier.

The experimental data used in the fits are a combination of the $A\,^2\Pi - X\,^2\Sigma^+$ and $C\,^2\Sigma^+ - X\,^2\Sigma^+$ transitions for the three isotopomers BeH, BeD and BeT reported by Colin and co-workers group [98, 99, 100, 101]. In order to perform a clean X-state analysis which would not be affected by perturbations between A and C-state levels, the $A - X$ and $C - X$ band transitions are re-arranged into the form of a fluorescence series. The highest observed vibrational level is $v'' = 10$ for BeH, and $v'' = 12$ for BeD. However, only the $0-0$, $1-1$, $2-2$ and $3-3$ bands were observed for BeT: moreover, the BeT data for many high-J levels (above 20) were not reliable, and thus were ignored in the fits. The experimental data are summarized in Table 5.1.

Isotopomer	Total #Lines	$Unc./\mathrm{cm}^{-1}$	Type	Range	Source
BeH	1495	0.01	$A\,^2\Pi - X\,^2\Sigma^+$	$v'' = 0 - 6$	Ref. [100]
		0.1	$C\,^2\Sigma^+ - X\,^2\Sigma^+$	$v'' = 7 - 10$	Ref. [99]
BeD	1290	0.01	$A\,^2\Pi - X\,^2\Sigma^+$	$v'' = 0 - 6$	Ref. [101]
		0.1	$C\,^2\Sigma^+ - X\,^2\Sigma^+$	$v'' = 8 - 12$	Ref. [99]
BeT	236	0.1	$A\,^2\Pi - X\,^2\Sigma^+$	$v'' = 0 - 3$	Ref. [98]

Table 5.1: Summary of the observed data for the $X\,^2\Sigma^+$ state of BeH, BeD and BeT. The reported experimental uncertainties ($Unc.$) are for unblended lines.

5.1 Fitting to the Extended Morse Oscillator Model

The EMO_p potential model

$$V_{\mathrm{EMO}_p}(R) = \mathfrak{D}_e \left[1 - e^{-\beta_{\mathrm{EMO}_p}(y_p)\,(R-R_e)}\right]^2 \tag{5.1}$$

was applied in the fit, where $y_p = (R^p - {R_e}^p)/(R^p + {R_e}^p)$ with $p = 2$. Eqs.(3.42) and (3.47) with $p = m = 2$ are used to represent the adiabatic and non-adiabatic correction functions. The fitted parameters are shown in Table 5.2; the numbers in parentheses are the 95% confidence limit uncertainties [88]. The potential curve and the $\beta(y_2)$ function are plotted in Fig. 5.1: the top frame shows the overall ground state potential curve of BeH molecule, and the bottom frame shows the $\beta(y_2)$ function. The well depth $\mathfrak{D}_e = 17530.5995 \pm 6.4\,\mathrm{cm}^{-1}$ is a free parameter determined from the fit.

The adiabatic BOB correction function was constrained to approach zero at the dissociation limit (u_∞^{H} was set to 0), since the given electronic state is the ground state. On the other hand, the data are not sufficiently extensive to discern the isotopic differences in the molecular dissociation energy $\Delta V_{ad}^{\alpha}(R = R_e)$ clearly, as specified in Eq.(3.45), and consequently u_0^{H} is also set to zero. Figure 5.2 shows the plots of adiabatic and non-adiabatic correction functions: the adiabatic BOB corrections are very significant because of the small reduced mass.

The current fit gives an RMSR value of 3.283; thus the fitted potential doesn't represent all the experimental data within the experimental uncertainties. However, when studying the differences between the calculated and observed values in more detail, one finds that the discrepancies mainly come from the transitions to a few high-J levels. These "bad" lines are listed in Table 5.3: v and J represent the ground state level, E is the level energy relative to the potential asymptote, R_2 is the outer turning point of the potential at that level, and $(\nu_{calc.} - \nu_{obs.})/Unc.$ is the ratio of the difference scaled by the experimental uncertainty between the calculated and the observed frequency for the transition from an upper state level to the X state. These relative discrepancies are listed in column I. Note from Table 5.3 that, except for the level $v = 8$ $J = 37$ in BeD, all other levels lie above the fitted $\mathfrak{D}_e$ value ($17530.5995\,\mathrm{cm}^{-1}$). When these particular lines are

ignored and the fit repeated, an RMSR of 1.329 is obtained, which demonstrates that discrepancies associated with these high-J level energies were responsible for the poor quality of the previous fit. This potential (RMSR = 1.329) is then used to predict these ignored transition frequencies. Their relative discrepancies are listed in the column *II* of Table 5.3. Some of the predicted frequencies are in good agreement with experimental data, but some of the predictions are much worse than those predicted from the previous fit. This shows that the previous fitted potential must be distorted in some way in an attempt to take account of the levels with large discrepancies. One possible way to account for the energy shifts of these high-J levels may be via the existence of a barrier in the rotationless potential curve [99]. To attempt to determine whether there really is a potential barrier in the rotationless potential curve, the same set of data was fitted using the DELR barrier potential model.

5.2 Fitting to the Double-Exponential Long-Range Model

The ground state of BeH dissociates to yield ground-state atoms Be(^{1}S)+H(^{2}S) [89]. The leading terms in its long-range potential are C_6/R^6, C_8/R^8 and C_{10}/R^{10}, and all these coefficients are negative (attractive) [4]. Thus, if a potential hump exists, it must come from the electron exchange interaction as the two atoms approach closer to one to another. However, the EMO$_p$ and MLJ$_p$ potential forms described in Section 3.1.5 are completely unable to yield a barrier protruding above the potential asymptote. On the other hand, the DELR potential described in Section 3.1.8 yields a barrier only if one of the leading terms is positive (repulsive). Thus, in the case of ground-state BeH, an additional repulsive term is required in the DELR model to represent the outer repulsive wall. The DELR model for this case is written as in Eq.(3.29), except that we define

$$V_{\rm LR}(R) \;=\; {\rm C}\, e^{-\chi\,\beta_0\,(R-R_e)} + \sum_{n=6,8,10} \frac{C_n}{R^n} {\rm D_n}(R) \quad , \tag{5.2}$$

where ${\rm C}\, e^{-\chi\,\beta_0\,(R-R_e)}$ is the electron exchange repulsion term, in which C is an amplitude, to be determined freely from the fit, β_0 is the first coefficient of the $\beta(y_p)$ function as defined in Eq.(3.21), and χ is a constant, defining the "softness" of the repulsive term. The parameter χ is

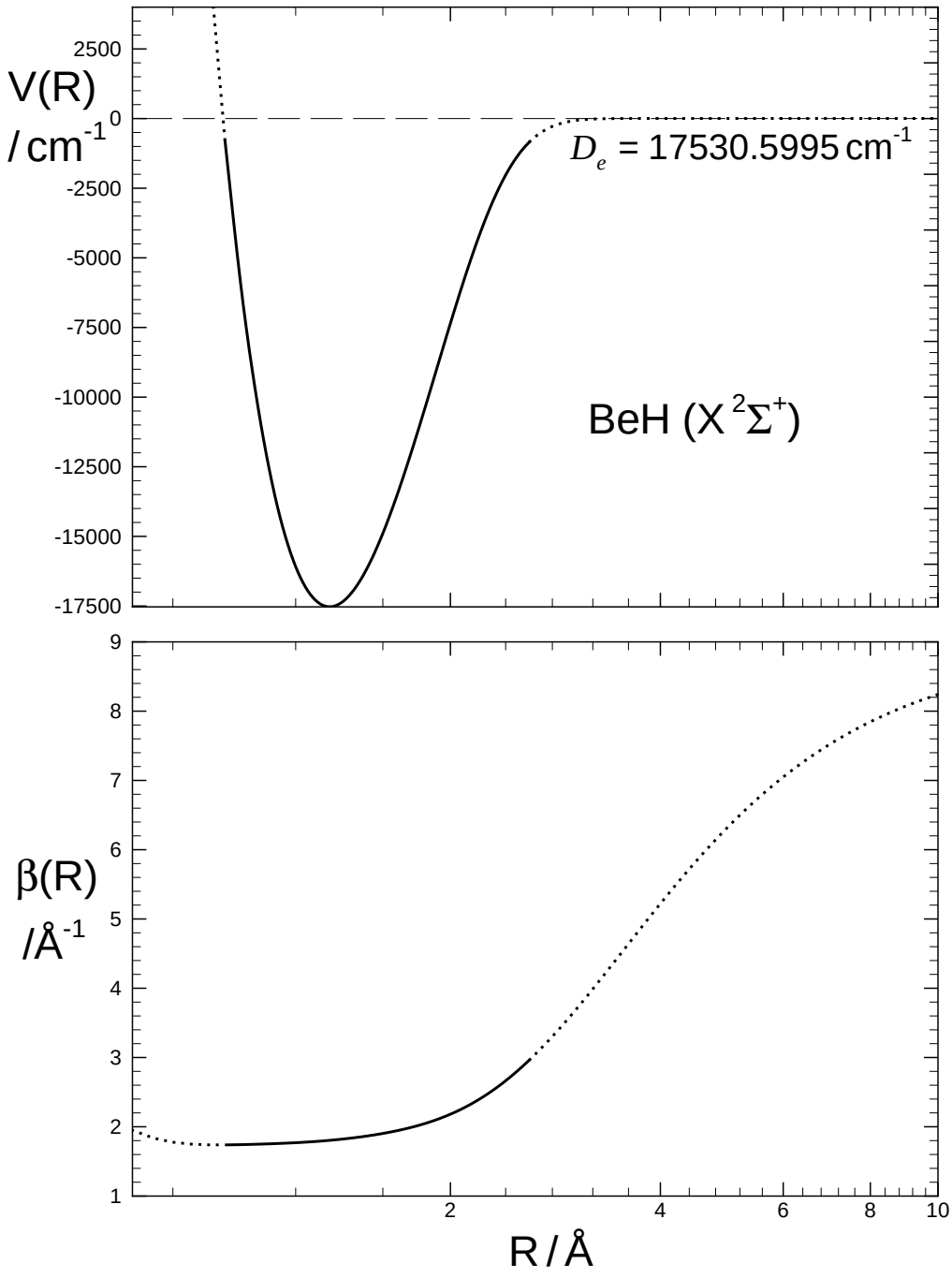

Figure 5.1: Plots of the EMO_2 potential curve and $\beta(y_2)$ function for the $X\,^2\Sigma^+$ state of BeH: the solid curve represents the experimental data region, while the dotted curves are extrapolations. The distance variable R is on a logarithmic scale.

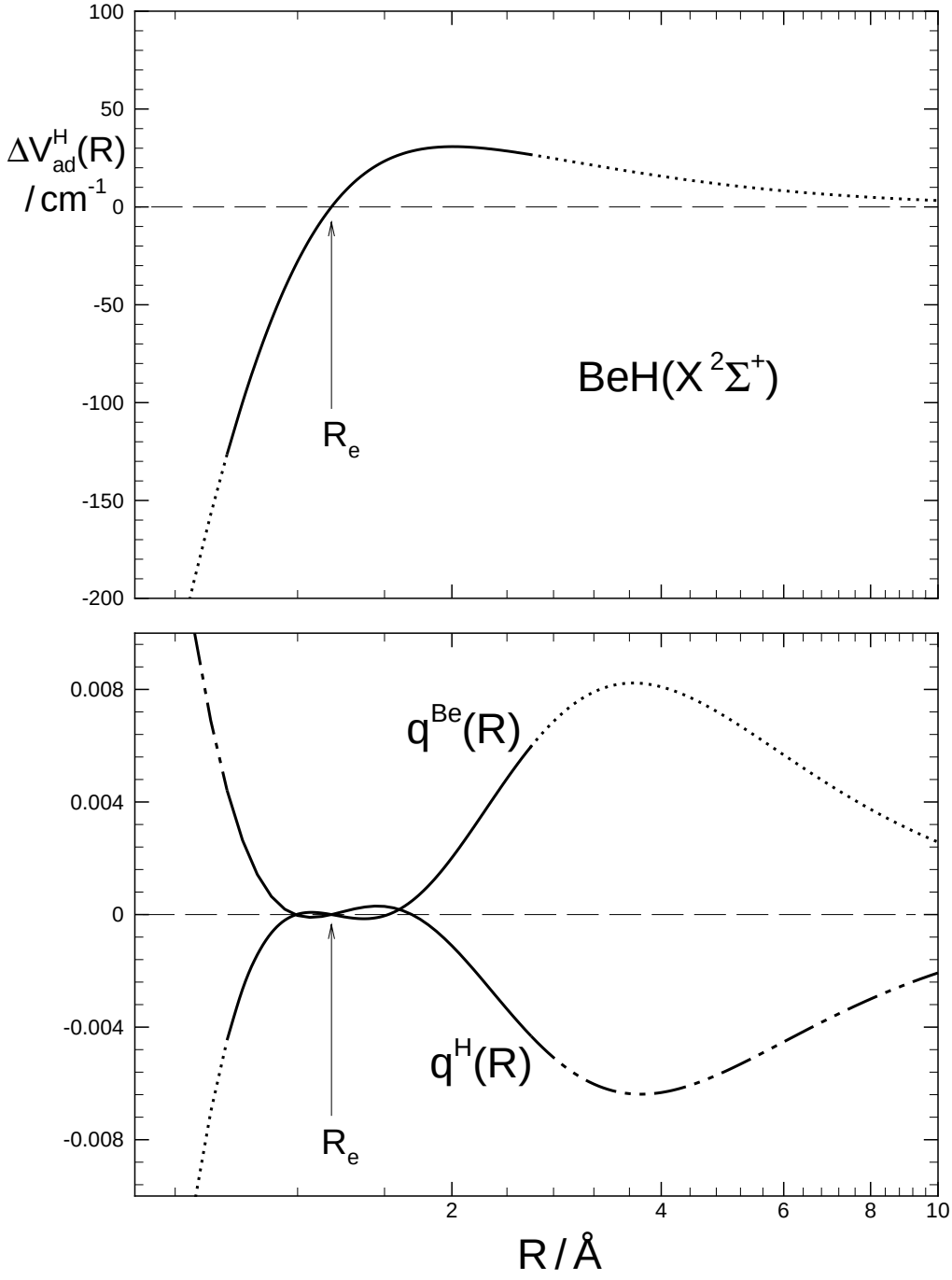

Figure 5.2: Plot of BOB correction functions determined with the EMO_2 function for ground state BeH; the top frame shows the adiabatic correction function, and the bottom frame shows the non-adiabatic centrifugal corrections. The distance variable R is on a logarithmic scale.

Parameter	BeH, BeD and BeT	
$\mathfrak{D}_e$ / cm^{-1}	17530.5995	(6.4)
R_e / Å	1.34231668	(4.3×10^{-5})
β_0 / Å^{-1}	1.8043336	(5.0×10^{-4})
β_1 / Å^{-1}	3.88834×10^{-1}	(2.6×10^{-3})
β_2 / Å^{-1}	8.52245×10^{-1}	(1.2×10^{-2})
β_3 / Å^{-1}	8.8516×10^{-1}	(5.0×10^{-2})
β_4 / Å^{-1}	3.386×10^{-1}	(2.4×10^{-1})
β_5 / Å^{-1}	4.5890	(3.5×10^{-1})
β_6 / Å^{-1}	9.103	(1.4)
β_7 / Å^{-1}	-8.99	(1.9)
u_0^{H} / cm^{-1}	0.0	
u_1^{H} / cm^{-1}	197.79	(15.0)
u_2^{H} / cm^{-1}	-222.42	(24.0)
u_3^{H} / cm^{-1}	121.0	(58.0)
u_∞^{H} / cm^{-1}	0.0	
q_0^{Be}	0.0	
q_1^{Be}	-1.916×10^{-3}	(1.0×10^{-3})
q_2^{Be}	-6.25×10^{-3}	(7.1×10^{-3})
q_3^{Be}	8.967×10^{-2}	(2.3×10^{-2})
q_∞^{Be}	0.0	
q_0^{H}	0.0	
q_1^{H}	2.48×10^{-3}	(1.1×10^{-3})
q_2^{H}	1.109×10^{-2}	(6.6×10^{-3})
q_3^{H}	-7.94×10^{-2}	(2.4×10^{-2})
q_∞^{H}	0.0	
# data	3021	
RMSR	3.283	

Table 5.2: Potential parameters and fitting quality for the $X\,^2\Sigma^+$ state of BeH, BeD and BeT obtained using the EMO_2 potential model.

	v	J	R_2	E	$(\nu_{calc.} - \nu_{obs.})/Unc.$	
					I	II
BeH						
	6	29	2.35	476.08	-15.84	-16.28
	6	30	2.37	843.06	1.49	0.47
	6	31	2.40	1211.44	1.58	16.28
	7	28	2.50	1120.72	-1.49	-0.79
	8	23	2.55	555.86	-1.66	0.50
	9	18	2.64	241.11	-5.11	-0.83
	9	19	2.67	432.53	-10.08	-4.06
BeD						
	8	37	2.28	-352.01	-18.11	-29.71
	8	39	2.32	195.97	-24.63	-31.16
	8	41	2.35	753.22	-13.71	-0.52
	8	42	2.37	1033.92	-8.47	3.97
	9	37	2.40	473.17	-27.32	-30.06
	9	38	2.42	724.20	-22.10	-0.49
	9	39	2.44	976.09	-22.92	-17.77
	9	40	2.46	1227.93	13.83	32.86
	9	41	2.49	1478.51	40.77	70.30
	10	34	2.47	504.24	-15.84	22.15
	10	35	2.49	725.19	21.96	45.90
	10	36	2.52	946.33	55.24	85.23
	10	37	2.55	1166.38	93.00	108.71

Table 5.3: The discrepancies between experimental frequencies and both fitted and predicted values using the EMO_2 potential for transitions to some high-J levels of BeH and BeD. R_2 is the outer turning point of the centrifugal distortion effective potential for that level. Column I is from a fit to all data, including these high-J levels; column II is the prediction from the potential obtained ignoring these levels.

constrained to be $0 < \chi \leq 1$ to make the repulsive term "softer" than the exponential terms used to determine the main potential well.

In the present fit, $\mathfrak{D}_e$ is fixed to the experimental value in an effort to determine the potential barrier. Colin *et al.* [102] reported an experimental $\mathfrak{D}_e$ value of $17426 \pm 100\,\mathrm{cm}^{-1}$, and estimated a barrier height of less than $200\,\mathrm{cm}^{-1}$ with its maximum located at $R \approx 3.3\,\text{Å}$ [99]. Taking into account the difference of the fitted $\mathfrak{D}_e$ ($17530.5995\,\mathrm{cm}^{-1}$) in our EMO_2 potential and the Colin *et al.* experimental value ($17426\,\mathrm{cm}^{-1}$), their experimental uncertainty of $\pm 100\,\mathrm{cm}^{-1}$ in $\mathfrak{D}_e$ and the estimated barrier height of $200\,\mathrm{cm}^{-1}$, trial fits were performed with $\mathfrak{D}_e$ fixed at 17426 and $17326\,\mathrm{cm}^{-1}$. In these fits, χ was not treated as a free parameter; rather, a series of fits with fixed trial values showed that the fits were stable when χ was chosen to be 0.5 or 1.0. The parameters of a typical fit ($\mathfrak{D}_e = 17326\,\mathrm{cm}^{-1}$, $\chi = 0.5$) are listed in Table 5.4. Figure 5.3 shows the associated potential curve, in which a maximum occurs at the distance $R \approx 3.25\,\text{Å}$ with an energy of about $17480.47\,\mathrm{cm}^{-1}$: thus, the barrier height relative to $\mathfrak{D}_e$ is approximately $17480 - 17326 = 154\,\mathrm{cm}^{-1}$.

Unfortunately, the fits using the DELR potential are no better than that using EMO_2 function. For example, the above fit with $\mathfrak{D}_e = 17326\,\mathrm{cm}^{-1}$ and $\chi = 0.5$ has a RMSR of 3.286, versus 3.283 in the previous fit using the EMO_2 model. In addition, the $(\nu_{calc.} - \nu_{obs.})/Unc.$ values for the set of high-J levels specified in Table 5.3 are nearly the same: thus, imposing a barrier in the current DELR potential fails to account for the problem. Table 5.5 compares the $(\nu_{calc.} - \nu_{obs.})/Unc.$ values obtained in the DELR and EMO_2 fits.

One way to explain the discrepancies may be that the current potential form simply cannot simulate the correct barrier shape adequately. Changes of the potential parameters in the current DELR model can affect the potential curve everywhere, while the ground-state BeH potential appears to be irregular only in a small region. Therefore, we need to build in "local-change-control" parameters to the model to manipulate these local structure. As an initial step, we may try to use the spline-pointwise IPA method, as described in Section 2.4.1, to obtain a pointwise potential curve. Although the potential function generated in that manner is not ideal, as seen for the case of B-state Li_2, it will hopefully give a good overall shape for the curve. Because the spline-pointwise IPA method optimizes the potential function point by point, the adjustment of

a single point does not affect the energies of the other potential points. Once the shape of the curve is known, we may model the potential by developing an appropriate analytical function.

Another reason for the poor quality fit may simply be that the discrepancies of these high-J levels come from some unknown source, and not from a barrier. This may be supported by the fact that some discrepancies in these high-J levels have opposite signs, while discrepancies of the same sign are expected if they are caused by a barrier. In any case, we have not found an adequate solution to this problem yet. It certainly needs further investigation to reveal the real shape of the potential curve and to develop a proper potential model to represent it.

Parameter	BeH, BeD and BeT	
$\mathfrak{D}_e$ / cm^{-1}	17326.0	
R_e / Å	1.34232013	(4.3×10^{-5})
A / cm^{-1}	17828.689	
B / cm^{-1}	36182.490	
C / cm^{-1}	1072.5	(37.0)
χ	0.5	
ρ_x	0.8748	
C_6 /cm^{-1} Å^6	-66270	
C_8 /cm^{-1} Å^8	-1.673×10^6	
C_{10} /cm^{-1} Å^{10}	-17.74×10^6	
β_0 / Å^{-1}	1.79316162	(9.3×10^{-4})
β_1 / Å^{-1}	0.375887	(2.8×10^{-3})
β_2 / Å^{-1}	0.84325	(0.011)
β_3 / Å^{-1}	0.82022	(0.050)
β_4 / Å^{-1}	0.025	(0.24)
β_5 / Å^{-1}	5.082	(0.35)
β_6 / Å^{-1}	10.2221	(1.4)
β_7 / Å^{-1}	-13.018	(2.0)
u_0^{H} / cm^{-1}	0.0	
u_1^{H} / cm^{-1}	197.54	(15.0)
u_2^{H} / cm^{-1}	-222.24	(24.0)
u_3^{H} / cm^{-1}	125.6	(58.0)
u_∞^{H} / cm^{-1}	0.0	
q_0^{Be}	0.0	
q_1^{Be}	-1.93×10^{-3}	(1.0×10^{-3})
q_2^{Be}	-6.14×10^{-3}	(7.1×10^{-3})
q_3^{Be}	0.08961	(2.3×10^{-3})
q_∞^{Be}	0.0	
q_0^{H}	0.0	
q_1^{H}	2.478×10^{-3}	(1.1×10^{-3})
q_2^{H}	0.01111	(6.6×10^{-3})
q_3^{H}	-0.0795	(0.024)
q_∞^{H}	0.0	
# data	3021	
RMSR	3.286	

Table 5.4: Potential parameters and fitting quality for the $X\,^2\Sigma^+$ state of BeH, BeD and BeT using the DELR potential model. The C_6, C_8 and C_{10} values have been obtained from Ref. [4]. The numbers in parentheses are the 95% confidence limit uncertainties in the parameters determined by the fit.

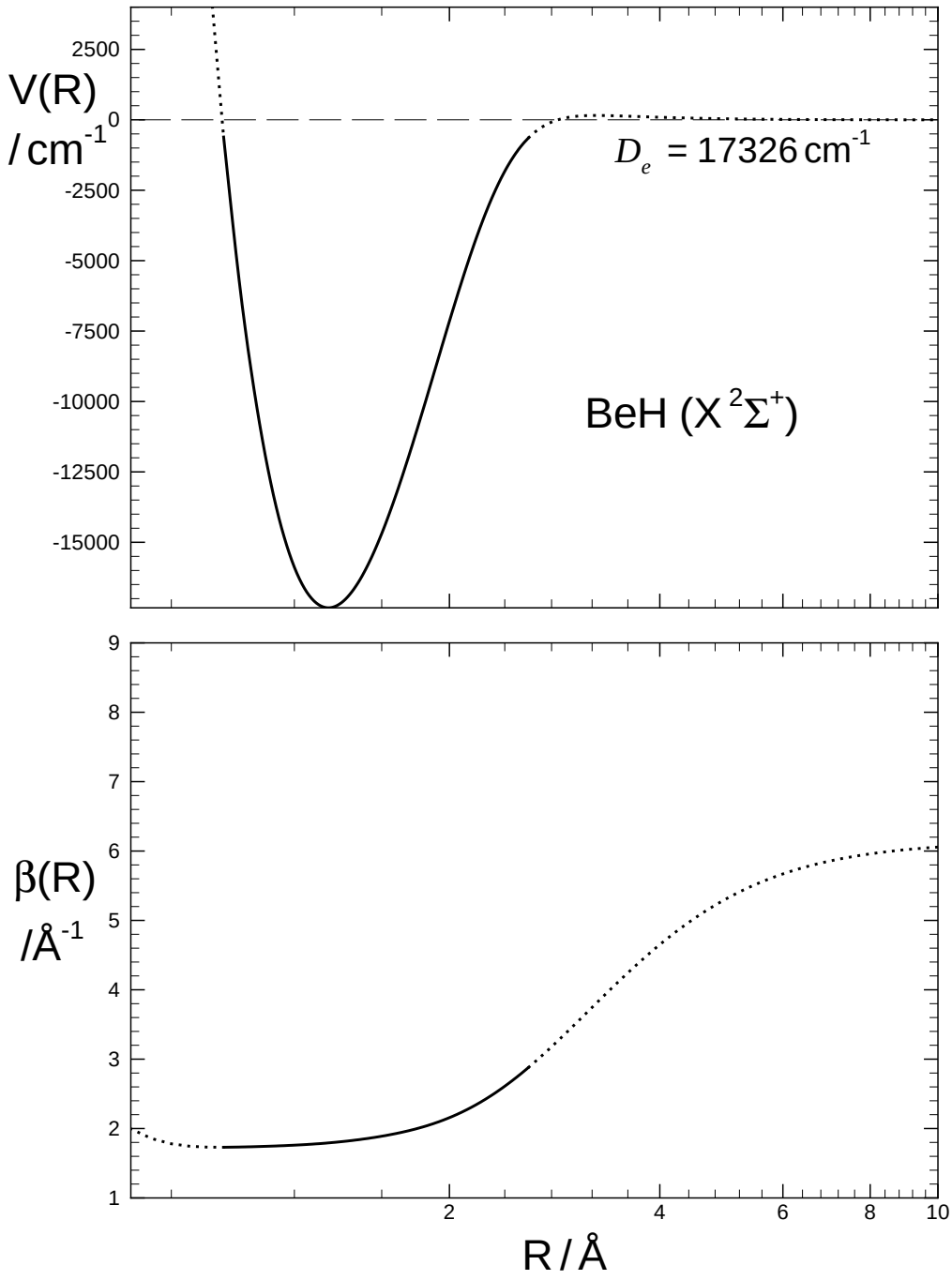

Figure 5.3: Plots of the DELR potential curve and the $\beta(y_2)$ function for the $X\,^2\Sigma^+$ state of BeH obtained with $\mathfrak{D}_e = 17326\,\mathrm{cm}^{-1}$ and $\chi = 0.5$; the solid curve spans the experimental data region and the dotted curve spans the extrapolation regions. The distance variable R is on a logarithmic scale.

			EMO_2	DELR			
			$\mathfrak{D}_e = 17531$	$\mathfrak{D}_e = 17326$	$\mathfrak{D}_e = 17326$	$\mathfrak{D}_e = 17426$	$\mathfrak{D}_e = 17426$
	v	J		$\chi = 0.5$	$\chi = 1.0$	$\chi = 0.5$	$\chi = 1.0$
BeH							
	6	29	-15.84	-15.90	-15.93	-15.87	-15.88
	6	30	1.49	1.66	1.83	1.58	1.68
	6	31	1.58	15.90	15.93	15.87	15.88
	7	28	-1.49	-1.66	-1.83	-1.58	-1.68
	8	23	-1.66	-1.88	-2.08	-1.79	-1.92
	9	18	-5.11	-4.92	-4.68	-5.02	-4.90
	9	19	-10.08	-6.99	-4.73	-8.39	-6.97
BeD							
	8	37	-18.11	-17.99	-17.88	-18.04	-17.98
	8	39	-24.63	-24.33	-24.06	-24.47	-24.32
	8	41	-13.71	-13.42	-13.17	-13.55	-13.41
	8	42	-8.47	-8.27	-8.10	-8.36	-8.26
	9	37	-27.32	-26.90	-26.58	-27.10	-26.92
	9	38	-22.10	-21.81	-21.59	-21.95	-21.82
	9	39	-22.92	-22.70	-22.55	-22.81	-22.73
	9	40	13.83	13.54	13.28	13.68	13.52
	9	41	40.77	40.30	39.90	40.52	40.29
	10	34	-1.584	-1.64	-1.71	-1.61	-1.66
	10	35	21.96	21.56	21.23	21.74	21.54
	10	36	55.24	54.45	53.81	54.82	54.45
	10	37	93.00	91.93	91.09	92.43	91.96

Table 5.5: Discrepancies between the calculated frequencies and the experimental values, divided by the experimental uncertainty, for transitions to some high-J levels of BeH and BeD for fitted DELR potential obtained with the indicated $\mathfrak{D}_e$ and χ values.

Chapter 6

Summary

New types of models for the potential energy and BOB correction functions have been developed, incorporated into the program DSPotFit, and tested in applications to data for a number of systems. The use of the variable $y_p(R) = (R^p - {R_e}^p)/(R^p + {R_e}^p)$ with $p > 1$ has helped to avoid unphysical behaviour in the long-range and short-range regions. The $y_p(R)$ variable is superior to the variable $z = y_1 = (R - R_e)/(R + R_e)$ used in previous work [10, 15], since the the use of $y_p(R)$ with $p > 1$ shortens the extrapolation region in terms of this variable. These conclusion have been tested by illustrative applications to the ground electronic states of the coinage metal hydrides and the Rb_2 molecule. The results show that with $p = 3$ these potential energy functions reproduce the experimental data within the experimental uncertainties, and extrapolate realistically to both small and large internuclear distances.

It has been shown that another simple technique for eliminating spurious behaviour in the short-range region of the potential is to truncate the polynomial describing the $\beta(y_p)$ function when $R < R_e$. Our application of the DELR potential model to the $B\,{}^1\Pi_u$ state of Li_2 provides a dramatic illustration of the utility of this technique. [1] The potential curve for this case misbehaves at short range when the complete $\beta(y_p)$ function is used for the entire range of internuclear distances, but is well-behaved when the inner wall of the potential is represented by a $\beta(y_p)$

[1] See Fig. 4.1.

polynomial of order N_S ($N_S = 3-5$), and the outer wall by the complete $\beta(y_p)$ function of order N_L ($N_L = 9$).

The new DELR potential model has proven to be useful for representing a potential curve with a barrier at long range, and has been successfully applied to the $B\,^1\Pi_u$ state of Li_2. However, an attempt to represent the $X\,^2\Sigma^+$ state of BeH by the DELR model has not yet proven satisfactory. The present study gives some hints for further investigation.

To account for Λ-doubling splitting in $^1\Pi$ electronic states, the effective Schrödinger equation used for our analytical DPF method has been extended by adding an analytical Λ-doubling radial strength function, and this capacity has been incorporated into DSPotFit. The DSPotFit program has been further developed to include the capacity for fitting the analytical potential energy functions to the tunneling predissociation line widths for quasibound levels. This improves the accuracy of fitted potentials with barriers.

The current directly-fitted analytical potential function for the $B\,^1\Pi_u$ state of Li_2 is the most accurate potential for this system yet obtained. It reproduces all available observed multiple-isotopomer transition frequency data within the experimental uncertainties, and represents the transition frequencies 5 times better than does the recently published SPP potential [2] (cf. a RMSR value of 1.03 for the present analytical potential with $q(R)$ ignored, versus a value of 5.42 for the SPP potential). Moreover, the discrepancies in tunneling predissociation line widths calculated from the present potential are a factor two smaller than those from the published SPP potential. The barrier height determined in the present analysis is $500.41 \pm 0.02\,cm^{-1}$, which has a lower estimated uncertainty than that ($500 \pm 2\,cm^{-1}$) obtained by Russier *et al.* [3].

Future work in this area should focus both on further improvement to existing potential models and to the development of new forms. As has been discussed in Chapter 5, a more subtle local way of modifying an analytical potential function is required to represent the ground state of BeH. One possible way for doing this is by introducing a damping function which can cancel the effect of global changes of the potential when changing a certain parameter.

Efforts to apply our analytical potential forms to fit to data for shelf state [104] and double-minimum [9] potential curves have been less satisfactory. In particular, spurious irregularities

appear at small internuclear distances in the $F\,^1\Sigma_g^+$ shelf state potential curve of Li_2, even using the new potential models, since an appropriate N_S value for the inner wall is difficult to determine due to the correlation among the terms of the high-order polynomial which is required to represent the shelf. One solution to this problem may be to use a potential model which takes into account the properties of the inverse-power long-range attraction and the $1/R$ very short-range repulsion. The MLJ model is an ideal form to implement this concept. Instead of using a constant power n in the MLJ function, a distance-dependent variable $\mathrm{N}(y_p)$ may be used:

$$V(R) \;=\; \mathfrak{D}_e \left[1 - \left(\frac{R_e}{R}\right)^{\mathrm{N}(y_p)} e^{-\beta(y_p)\, y_p}\right]^2 \tag{6.1}$$

where $\mathrm{N}(y_p)$ is defined as

$$\mathrm{N}(y_p) = \frac{y_p(y_p-1)}{4} + \frac{n(y_p+1)}{2} \tag{6.2}$$

with n being the leading long-range power. Thus, $\lim_{R\to 0} \mathrm{N}(y_p) = 1/2$ and $\lim_{R\,\to\,\infty} \mathrm{N}(y_p) = n$, which yields a $1/R$ repulsive term at short range and a $1/R^n$ term at long range. This new form or modified versions of it will be implemented in future work. Hopefully it will help to solve the extrapolation problem completely.

To date, the DSPotFit program treats each electronic state independently without considering the coupling of two states of the same symmetry in the same energy region, since the program is based on the adiabatic approximation which ignores explicit interactions with the levels of neighbouring electronic states. To deperturb the coupled states, incorporation of the coupled Schrödinger equations is required, which may help to deal with some irregular potential energy functions such as the $F\,^1\Sigma_g^+$ shelf state of Li_2, since the shelf is caused by avoided-crossings with the $E\,^1\Sigma_g^+$ and $G\,^1\Sigma_g^+$ states.

Another topic for future research involves extending the program to allow fits to data for non-singlet electronic states. Due to the interactions between the electronic spin and the orbital and rotational angular momenta, the normal rotational energy levels of non-singlet electronic states split further into multiple levels, and the eigenvalue calculation becomes more complicated.

Significant extension of the present methodology will have to be developed to take account of this effect.

Appendix A

Partial Derivatives of Potential Energy and BOB Functions

As has been described in Section 2.4.2, the least-squares fitting procedure requires a knowledge of the partial derivatives of the calculated value of each datum with respect to each parameter of the model. The application of this method in potential fitting therefore requires the calculation of the partial derivatives of the effective potentials (the analytical potential energy and correction functions) with respect to each of the fitted parameters. The partial derivative of the effective potential

$$V_{eff}(R) = V(R) + \Delta V_{\rm ad}^{(\alpha)}(R) + \frac{\hbar^2\left[J(J+1)-\Omega^2\right]}{2\mu_\alpha R^2}\left[1 + q^{(\alpha)}(R) \pm f_\Lambda(R)\right] \quad , \tag{A.1}$$

with respect to potential parameter P_k is

$$\frac{\partial V_{eff}(R)}{\partial P_k} = \frac{\partial V(R)}{\partial P_k} + \frac{\partial \Delta V_{\rm ad}^{(\alpha)}(R)}{\partial P_k} + \frac{\hbar^2\left[J(J+1)-\Omega^2\right]}{2\mu_\alpha R^2}\left[\frac{\partial q^{(\alpha)}(R)}{\partial P_k} \pm \frac{\partial f_\Lambda(R)}{\partial P_k}\right] \quad . \tag{A.2}$$

For the analytical potential energy and correction function forms introduced in this work, expressions for the various partial derivatives are listed below.

A.1 The Partial Derivatives of Rotationless Potentials

The potential function models EMO_p, MLJ_p, MLJ_p^c and DELR are considered here; partial derivatives for a range of other potential forms were presented in Ref. [9]. It is readily shown that when $p = 1$ the partial derivatives presented in Sections A.1.1 and A.1.2 collapse to those listed in Ref. [9].

A.1.1 The Extended Morse Oscillator Potential, EMO_p

The EMO_p potential is defined by Eqs.(A.3) - (A.5):

$$\begin{aligned} V_{\mathrm{EMO}_p}(R) &= \mathfrak{D}_e \left[1 - e^{-\beta_{\mathrm{EMO}_p}(y_p)\,(R-R_e)}\right]^2 \\ &= \mathfrak{D}_e + \mathfrak{D}_e\, e^{-2\beta_{\mathrm{EMO}_p}(y_p)\,(R-R_e)} - 2\mathfrak{D}_e e^{-\beta_{\mathrm{EMO}_p}(y_p)\,(R-R_e)} \quad , \qquad \text{(A.3)} \\ y_p(R) &= \frac{R^p - {R_e}^p}{R^p + {R_e}^p} \quad , \qquad \text{(A.4)} \\ \beta_{\mathrm{EMO}_p}(y_p) &= \beta_0^{\mathrm{EMO}_p} + \beta_1^{\mathrm{EMO}_p} y_p + \beta_2^{\mathrm{EMO}_p} {y_p}^2 + \ldots \quad . \qquad \text{(A.5)} \end{aligned}$$

The potential derivatives required for the eigenvalue derivative calculation are:

$$\frac{\partial V_{\mathrm{EMO}_p}(R)}{\partial \mathfrak{D}_e} = \left[1 - e^{-\beta_{\mathrm{EMO}_p}(y_p)\,(R-R_e)}\right]^2 \quad , \qquad \text{(A.6)}$$

$$\begin{aligned} \frac{\partial V_{\mathrm{EMO}_p}(R)}{\partial R_e} &= -2\mathfrak{D}_e e^{-\beta_{\mathrm{EMO}_p}(y_p)\,(R-R_e)} \left[1 - e^{-\beta_{\mathrm{EMO}_p}(y_p)\,(R-R_e)}\right] \\ &\quad \times \left[\beta_{\mathrm{EMO}_p}(y_p) + \frac{2p\,{R_e}^{p-1}\,R^p\,(R-R_e)}{(R^p + {R_e}^p)^2} \sum_{i=0}^{N} i\,\beta_i^{\mathrm{EMO}_p}\,{y_p}^{i-1}\right] \quad , \qquad \text{(A.7)} \end{aligned}$$

$$\frac{\partial V_{\mathrm{EMO}_p}(R)}{\partial \beta_i^{\mathrm{EMO}_p}} = 2\mathfrak{D}_e e^{-\beta_{\mathrm{EMO}_p}(y_p)\,(R-R_e)} \left[1 - e^{-\beta_{\mathrm{EMO}_p}(y_p)\,(R-R_e)}\right] (R-R_e)\,{y_p}^i \quad . \qquad \text{(A.8)}$$

A.1.2 The Morse-Lennard-Jones Potential, MLJ_p

The MLJ_p potential is defined by Eqs.(A.9) and (A.10):

$$V_{\mathrm{MLJ}_p}(R) = \mathfrak{D}_e \left[1 - \left(\frac{R_e}{R}\right)^n e^{-\beta_{\mathrm{MLJ}_p}(y_p)\, y_p}\right]^2 \quad , \tag{A.9}$$

$$\beta_{\mathrm{MLJ}_p}(y_p) = \beta_0^{\mathrm{MLJ}_p} + \beta_1^{\mathrm{MLJ}_p} y_p + \beta_2^{\mathrm{MLJ}_p} {y_p}^2 + \ldots \quad . \tag{A.10}$$

The potential derivatives required for the eigenvalue derivative calculation are:

$$\frac{\partial V_{\mathrm{MLJ}_p}(R)}{\partial \mathfrak{D}_e} = \left[1 - \left(\frac{R_e}{R}\right)^n e^{-\beta_{\mathrm{MLJ}_p}(y_p)\, y_p}\right]^2 \quad , \tag{A.11}$$

$$\frac{\partial V_{\mathrm{MLJ}_p}(R)}{\partial R_e} = -2\mathfrak{D}_e \left(\frac{R_e}{R}\right)^n e^{-\beta_{\mathrm{MLJ}_p}(y_p)\, y_p} \left[1 - \left(\frac{R_e}{R}\right)^n e^{-\beta_{\mathrm{MLJ}_p}(y_p)\, y_p}\right] \times \left[\frac{n}{R_e} + \frac{2p\, {R_e}^{p-1} R^p}{(R^p + {R_e}^p)^2} \sum_{i=0}^{N} (i+1)\, \beta_i^{\mathrm{MLJ}_p}\ {y_p}^{i+1}\right] \quad , \tag{A.12}$$

$$\frac{\partial V_{\mathrm{MLJ}_p}(R)}{\partial \beta_i^{\mathrm{MLJ}_p}} = 2\mathfrak{D}_e \left(\frac{R_e}{R}\right)^n \left[1 - \left(\frac{R_e}{R}\right)^n e^{-\beta_{\mathrm{MLJ}_p}(y_p)\, y_p}\right] {y_p}^{i+1} \quad . \tag{A.13}$$

A.1.3 The Constrained Morse-Lennard-Jones Potential, MLJ_p^c

The MLJ_p^c potential is defined by Eqs.(A.14) - (A.16):

$$V_{\mathrm{MLJ}_p^c}(R) = \mathfrak{D}_e \left[1 - \left(\frac{R_e}{R}\right)^n e^{-\beta_{\mathrm{MLJ}_p^c}(y_p)}\right]^2 \quad , \tag{A.14}$$

$$\beta_{\mathrm{MLJ}_p^c}(R) = \beta^\infty \left(\frac{R^p - {R_e}^p}{R^p + {R_e}^p}\right) + \left(\frac{2{R_e}^p}{R^p + {R_e}^p}\right) \sum_{i=1} \beta_i \left(\frac{R^p - {R_e}^p}{R^p + {R_e}^p}\right)^i \quad , \tag{A.15}$$

$$\beta^\infty = \ln\left[-2\,\mathfrak{D}_e (R_e)^n / C_n\right] \quad . \tag{A.16}$$

The potential derivatives required for the eigenvalue derivative calculation are:

$$\frac{\partial V_{\mathrm{MLJ}_p^c}(R)}{\partial \mathfrak{D}_e} = \left[1 - \left(\frac{R_e}{R}\right)^n e^{-\beta_{\mathrm{MLJ}_p^c}(y_p)}\right]^2 \quad , \tag{A.17}$$

$$\frac{\partial V_{\mathrm{MLJ}_p^c}(R)}{\partial R_e} = -2\mathfrak{D}_e \left(\frac{R_e}{R}\right)^n e^{-\beta_{\mathrm{MLJ}_p^c}(y_p)} \left[1 - \left(\frac{R_e}{R}\right)^n e^{-\beta_{\mathrm{MLJ}_p^c}(y_p)}\right] \times \left[\frac{n}{R_e} + \frac{2p\,{R_e}^{p-1}\,R^p}{(R^p + {R_e}^p)^2} \left(\beta^\infty + \sum_{i=0}^{N} \beta_i \frac{2i\,{R_e}^p + {R_e}^p - R^p}{R^p + {R_e}^p} {y_p}^{i-1}\right)\right] \quad ,(A.18)$$

$$\frac{\partial V_{\mathrm{MLJ}_p^c}(R)}{\partial \beta_i} = 2\mathfrak{D}_e \left(\frac{R_e}{R}\right)^n e^{-\beta_{\mathrm{MLJ}_p^c}(y_p)} \left[1 - \left(\frac{R_e}{R}\right)^n e^{-\beta_{\mathrm{MLJ}_p^c}(y_p)}\right] \frac{2{R_e}^p}{R^p + {R_e}^p} {y_p}^i \quad . \tag{A.19}$$

A.1.4 The Double-Exponential Long-Range Potential, DELR

The general form of the DELR potential is defined by Eqs.(A.20) - (A.28):

$$V_{\mathrm{DELR}}(R) = [\mathrm{A}\, e^{-2\beta(y_p)\,(R-R_e)} - \mathrm{B}\, e^{-\beta(y_p)\,(R-R_e)} + \mathfrak{D}_e] + V_{\mathrm{LR}}(R) \quad , \tag{A.20}$$

$$V_{\mathrm{LR}}(R) = \mathrm{C}\, e^{-\chi\,\beta_0\,(R-R_e)} + \sum_n \frac{C_n}{R^n} \mathrm{D_n}(R) \quad , \tag{A.21}$$

$$\beta(y_p) = \sum_{i=0}^{N} \beta_i\, y^i \quad , \tag{A.22}$$

$$\mathrm{A} = \mathfrak{D}_e + \sum_n \frac{C_n}{{R_e}^n} \mathrm{D_n}(R_e) \left[1 + \frac{\mathrm{D}'_n(R_e)}{\beta_0 \mathrm{D}_n(R_e)} - \frac{n}{\beta_0 R_e}\right] + (1-\chi)\,\mathrm{C} \quad , \tag{A.23}$$

$$\mathrm{B} = 2\mathfrak{D}_e + \sum_n \frac{C_n}{{R_e}^n} \mathrm{D_n}(R_e) \left[2 + \frac{\mathrm{D}'_n(R_e)}{\beta_0 \mathrm{D}_n(R_e)} - \frac{n}{\beta_0 R_e}\right] + (2-\chi)\,\mathrm{C} \quad , \tag{A.24}$$

$$\mathrm{D_n}(R) = \left[1 - \exp\{-2.1(\rho_x\, R)/n - 0.109(\rho_x\, R)^2/\sqrt{n}\}\right]^n \tag{A.25}$$

$$\mathrm{D}'_n(R_e) = \left.\frac{d\mathrm{D}_n(R)}{dR}\right|_{R=R_e} = (2.1\rho_x + 0.218\sqrt{n}\,\rho_x^2\, R_e)\, e^{\mathrm{d}}\,(1-e^{\mathrm{d}})^{n-1} \quad , \tag{A.26}$$

$$\mathrm{D}''_n(R_e) = \left.\frac{d^2\mathrm{D}_n(R)}{dR^2}\right|_{R=R_e} = \left[0.218\sqrt{n}\rho_x^2 - n\left(\frac{\mathrm{d}}{R_e}\right)^2 \frac{1 - ne^{\mathrm{d}}}{1-e^{\mathrm{d}}}\right] e^{\mathrm{d}}(1-e^{\mathrm{d}})^{n-1} \quad ,(A.27)$$

$$\text{with} \quad \mathrm{d} = -\frac{2.1\rho_x\, R_e}{n} - \frac{0.109\rho_x^2\, {R_e}^2}{\sqrt{n}} \quad . \tag{A.28}$$

The potential derivatives required for the eigenvalue derivative calculation are:

$$\frac{\partial V_{\mathrm{DELR}}(R)}{\partial \mathfrak{D}_e} = e^{-2\beta(y_p)\,(R-R_e)} - 2e^{-\beta(y_p)\,(R-R_e)} + 1 \tag{A.29}$$

$$\frac{\partial V_{\mathrm{DELR}}(R)}{\partial R_e} = \left[2\mathrm{A}\, e^{-2\beta(y_p)\,(R-R_e)} - \mathrm{B}\, e^{-\beta(y_p)\,(R-R_e)}\right] \left[\beta(y_p) + \frac{2p\,{R_e}^{p-1}\,R^p\,(R-R_e)}{(R^p + {R_e}^p)^2} \sum_{i=0}^{N} i\,\beta_i\, {y_p}^{i-1}\right]$$

$$+ e^{-2\beta(y_p)\,(R-R_e)}\,\frac{d\mathrm{A}}{dR_e} - e^{-\beta(y_p)\,(R-R_e)}\,\frac{d\mathrm{B}}{dR_e} + \chi\,C\,\beta_0\,e^{-\chi\,\beta_0\,(R-R_e)} \quad , \tag{A.30}$$

$$\frac{d\mathrm{A}}{dR_e} = \sum_n C_n \left\{ \left[\frac{\mathrm{D}'_n(R_e)\,R_e - n\,\mathrm{D}_n(R_e)}{{R_e}^{n+1}} \right] \left[1 + \frac{\mathrm{D}'_n(R_e)}{\beta_0\,\mathrm{D}_n(R_e)} - \frac{n}{\beta_0\,R_e} \right] + \frac{\mathrm{D}_n(R_e)}{{R_e}^{n}} \left[\frac{\mathrm{D}_n(R_e)\,\mathrm{D}''_n(R_e) - \mathrm{D}'_n(R_e)^2}{\beta_0\,\mathrm{D}_n(R_e)^2} + \frac{n}{\beta_0\,{R_e}^2} \right] \right\} \quad , \tag{A.31}$$

$$\frac{d\mathrm{B}}{dR_e} = \sum_n C_n \left\{ \left[\frac{\mathrm{D}'_n(R_e)\,R_e - n\,\mathrm{D}_n(R_e)}{{R_e}^{n+1}} \right] \left[2 + \frac{\mathrm{D}'_n(R_e)}{\beta_0\,\mathrm{D}_n(R_e)} - \frac{n}{\beta_0\,R_e} \right] + \frac{\mathrm{D}_n(R_e)}{{R_e}^{n}} \left[\frac{\mathrm{D}_n(R_e)\,\mathrm{D}''_n(R_e) - \mathrm{D}'_n(R_e)^2}{\beta_0\,\mathrm{D}_n(R_e)^2} + \frac{n}{\beta_0\,{R_e}^2} \right] \right\} \quad , \tag{A.32}$$

$$\frac{\partial V_{\mathrm{DELR}}(R)}{\partial \beta_0} = \left[-2\mathrm{A}\,e^{-2\beta(y_p)\,(R-R_e)} + \mathrm{B}\,e^{-\beta(y_p)\,(R-R_e)} - \chi\,\mathrm{C}\,e^{-\chi\,\beta_0\,(R-R_e)} \right] (R-R_e) + \left[e^{-2\beta(y_p)\,(R-R_e)} - e^{-\beta(y_p)\,(R-R_e)} \right] \sum_n \frac{C_n\,\mathrm{D}_n(R_e)}{{R_e}^{n}} \left[\frac{n}{\beta_0^2\,R_e} - \frac{\mathrm{D}'_n(R_e)}{\beta_0^2\,\mathrm{D}_n(R_e)} \right] \quad , \tag{A.33}$$

$$\frac{\partial V_{\mathrm{DELR}}(R)}{\partial \beta_i} = \left[-2\mathrm{A}\,e^{-2\beta(y_p)\,(R-R_e)} + \mathrm{B}\,e^{-\beta(y_p)\,(R-R_e)} \right] (R-R_e)\,{y_p}^i \quad \text{with } i > 0 \quad , \tag{A.34}$$

$$\frac{\partial V_{\mathrm{DELR}}(R)}{\partial \mathrm{C}} = (1-\chi)\,e^{-2\beta(y_p)\,(R-R_e)} - (2-\chi)\,e^{-\beta(y_p)\,(R-R_e)} + e^{-\chi\,\beta_0\,(R-R_e)} \quad . \tag{A.35}$$

A.2 Born-Oppenheimer Breakdown Correction Functions

The adiabatic and non-adiabatic correction functions used herein have the forms:

$$\Delta V_{\mathrm{ad}}^{\alpha}(R) = \frac{\Delta M_{\mathrm{A}}^{\alpha}}{M_{\mathrm{A}}^{\alpha}}\,\Delta V_{\mathrm{ad}}^{\mathrm{A}}(R) + \frac{\Delta M_{\mathrm{B}}^{\alpha}}{M_{\mathrm{B}}^{\alpha}}\,\Delta V_{\mathrm{ad}}^{\mathrm{B}}(R) \quad , \tag{A.36}$$

and

$$q^{\alpha}(R) = \frac{M_{\mathrm{A}}^{1}}{M_{\mathrm{A}}^{\alpha}}\,q_{\mathrm{A}}(R) + \frac{M_{\mathrm{B}}^{1}}{M_{\mathrm{B}}^{\alpha}}\,q_{\mathrm{B}}(R) \quad . \tag{A.37}$$

Thus, their partial derivatives are written as

$$\frac{\partial \Delta V_{\rm ad}^{\alpha}(R)}{\partial P_k} = \frac{\Delta M_{\rm A}^{\alpha}}{M_{\rm A}^{\alpha}} \frac{\partial \Delta V_{\rm ad}^{\rm A}(R)}{\partial P_k} + \frac{\Delta M_{\rm B}^{\alpha}}{M_{\rm B}^{\alpha}} \frac{\partial \Delta V_{\rm ad}^{\rm B}(R)}{\partial P_k} \quad , \tag{A.38}$$

and

$$\frac{\partial q^{\alpha}(R)}{\partial P_k} = \frac{M_{\rm A}^{1}}{M_{\rm A}^{\alpha}} \frac{\partial q_{\rm A}(R)}{\partial P_k} + \frac{M_{\rm B}^{1}}{M_{\rm B}^{\alpha}} \frac{\partial q_{\rm B}(R)}{\partial P_k} \quad . \tag{A.39}$$

Only the partial derivatives for atom A are written down below; the partial derivatives for atom B of course have the same forms.

A.2.1 Adiabatic Correction Function

The present work has introduced the new "limit-specified" expression of the form:

$$\Delta V_{\rm ad}^{\rm A}(R) = u_0^{\rm A} \left(\frac{2{R_e}^m}{R^m + {R_e}^m} \right) + u_\infty^{\rm A} \left(\frac{R^m - {R_e}^m}{R^m + {R_e}^m} \right) + \left(\frac{2{R_e}^m}{R^m + {R_e}^m} \right) \sum_{i=1} u_i^{\rm A} \left(\frac{R^p - {R_e}^p}{R^p + {R_e}^p} \right)^i \quad . \tag{A.40}$$

Partial derivatives with respect to its variables are

$$\begin{aligned} \frac{\partial \Delta V_{\rm ad}^{\rm A}(R)}{\partial R_e} = {} & \frac{2m\,{R_e}^{m-1} R^m}{(R^m + {R_e}^m)^2} \left[u_0^{\rm A} - u_\infty^{\rm A} + \sum_{i=1}^{N} u_i^{\rm A} \left(\frac{R^p - {R_e}^p}{R^p + {R_e}^p} \right)^i \right] \\ & - \left(\frac{2{R_e}^m}{R^m + {R_e}^m} \right) \frac{2p\,{R_e}^{p-1} R^p}{(R^p + {R_e}^p)^2} \sum_{i=1}^{N} u_i^{\rm A}\, i \left(\frac{R^p - {R_e}^p}{R^p + {R_e}^p} \right)^{i-1} \quad , \end{aligned} \tag{A.41}$$

$$\frac{\partial \Delta V_{\rm ad}^{\rm A}(R)}{\partial u_0^{\rm A}} = \frac{2{R_e}^m}{R^m + {R_e}^m} \quad , \tag{A.42}$$

$$\frac{\partial \Delta V_{\rm ad}^{\rm A}(R)}{\partial u_\infty^{\rm A}} = \frac{R^m - {R_e}^m}{R^m + {R_e}^m} \quad , \tag{A.43}$$

$$\frac{\partial \Delta V_{\rm ad}^{\rm A}(R)}{\partial u_i^{\rm A}} = \frac{2{R_e}^m}{(R^m + {R_e}^m)} \left(\frac{R^p - {R_e}^p}{R^p + {R_e}^p} \right)^i \quad \text{with } i > 0 \quad . \tag{A.44}$$

A.2.2 Non-adiabatic Centrifugal Correction Function

Our limit-specified expression for the non-adiabatic centrifugal correction function have form:

$$q_{\mathrm{A}}(R) \;=\; q_0^{\mathrm{A}} \left(\frac{2{R_e}^p}{R^p + {R_e}^p} \right) + q_\infty \left(\frac{R^p - {R_e}^p}{R^p + {R_e}^p} \right) + \left(\frac{2{R_e}^p}{R^p + {R_e}^p} \right) \sum_{i=1} q_i^{\mathrm{A}} \left(\frac{R^p - {R_e}^p}{R^p + {R_e}^p} \right)^i \quad . \tag{A.45}$$

Hence its partial derivatives are:

$$\frac{\partial q_{\mathrm{A}}(R)}{\partial R_e} \;=\; \frac{2p\,{R_e}^{p-1}\,R^p}{(R^p + {R_e}^p)^2} \left[q_0^{\mathrm{A}} - q_\infty^{\mathrm{A}} + \sum_{i=1}^{N} q_i^{\mathrm{A}} \, \frac{(R^p - {R_e}^p)^{i-1}\,(R^p - {R_e}^p - 2i\,{R_e}^p)}{(R^p + {R_e}^p)^i} \right] \quad , \tag{A.46}$$

$$\frac{\partial q_{\mathrm{A}}(R)}{\partial q_0^{\mathrm{A}}} \;=\; \frac{2{R_e}^p}{R^p + {R_e}^p} \quad , \tag{A.47}$$

$$\frac{\partial q_{\mathrm{A}}(R)}{\partial q_\infty^{\mathrm{A}}} \;=\; \frac{R^p - {R_e}^p}{R^p + {R_e}^p} \quad , \tag{A.48}$$

$$\frac{\partial q_{\mathrm{A}}(R)}{\partial q_i^{\mathrm{A}}} \;=\; \frac{2{R_e}^p\,(R^p - {R_e}^p)^i}{(R^p + {R_e}^p)^{i+1}} \quad \text{with } i > 0 \quad . \tag{A.49}$$

A.3 Λ-doubling Radial Strength Function

The Λ-doubling radial strength function used here have the form:

$$f_\Lambda(R) \;=\; \sum_{i=0}^{N} l_i \, {y_p}^i \;=\; \sum_{i=0}^{N} l_i \left(\frac{R^p - {R_e}^p}{R^p + {R_e}^p} \right)^i \quad . \tag{A.50}$$

Its partial derivatives are

$$\frac{\partial f_\Lambda(R)}{\partial R_e} \;=\; -\frac{2p\,{R_e}^{p-1}\,R^p}{(R^p + {R_e}^p)^2} \sum_{i=0}^{N} l_i \, i \, \left(\frac{R^p - {R_e}^p}{R^p + {R_e}^p} \right)^{i-1} \quad , \tag{A.51}$$

$$\frac{\partial f_\Lambda(R)}{\partial l_i} \;=\; \left(\frac{R^p - {R_e}^p}{R^p + {R_e}^p} \right)^i \quad . \tag{A.52}$$

Appendix B

Partial Derivatives of Widths and Evaluation of Phase Integrals

The first-order semiclassical representation of tunneling predissociation line width Eq.(2.32) is expressed as

$$\Gamma(\omega, t_{vib}) \;=\; \frac{\hbar}{\tau} \;=\; \frac{\hbar\omega}{t_{vib}} \quad , \tag{B.1}$$

where t_{vib} is

$$t_{vib} \;=\; (2\mu) \int_{R_1}^{R_2} \frac{dR}{[E - V_J(R)]^{1/2}} \tag{B.2}$$

and ω is

$$\omega \;=\; \exp\left\{ -\frac{(8\mu)^{1/2}}{\hbar} \int_{R_2}^{R_3} [V_J(R) - E]^{1/2}\, dR \right\} \quad . \tag{B.3}$$

Application of the chain rule gives its partial derivatives with respect to potential parameters as:

$$\frac{\partial\Gamma(\omega, t_{vib})}{\partial P_k} \;=\; \frac{\hbar}{t_{vib}} \frac{\partial\omega}{\partial P_k} - \frac{\hbar\omega}{{t_{vib}}^2} \frac{\partial t_{vib}}{\partial P_k} \quad . \tag{B.4}$$

The expressions of t_{vib}, ω, $\partial\omega/\partial P_k$ and $\partial t_{vib}/\partial P_k$ involves the phase integral of the form:

$$I_k^n(R_a, R_b) \;=\; \oint_{\tau_{(R_a,R_b)}} \frac{(dV_J(R)/dP_k - dE/dP_k)^n}{[E - V_J(R)]^{k+1/2}}\, dR \quad , \tag{B.5}$$

where k and n are integers, $\tau_{(R_a,R_b)}$ is the contour in the complex plane surrounding a segment of the real line running between two turning points R_a and R_b, $dV_J(R)/dP_k$ is the partial derivative of the potential function with respect to its parameters, as defined in Appendix A, and the partial derivatives of the eigenvalue dE/dP_k can be evaluated by the Hellmann-Feynman theorem, as described in Section 2.4.2. If $k > 0$, the above phase integral has non-integrable singularities on the real line. Various methods to evaluate such phase integrals $I_k^n(R_a, R_b)$ have been reported [105, 106, 107, 108]; the Pajunen-Chebyshev quadrature method was used in this work [106].

Bibliography

[1] J.P. Burke Jr. and J.L. Bohn and B.D. Esry and C.H. Greene, Phys. Rev. Lett. **80**, 2097 (1998).

[2] N. Bouloufa and P. Cacciani and R. Vetter and A. Yiannopoulou, F. Martin and A. J. Ross, J. Chem. Phys. **114**, 8445 (2001).

[3] I. Russier, F. Martin, C. Linton, P. Crozet, A. J. Ross, R. Bacis, and S. Churassy, J. Mol. Spectrosc. **168**, 39 (1994).

[4] J. M. Standard and P. R. Certain, J. Chem. Phys. **83**, 3002 (1985).

[5] R. J. Le Roy, *DSParFit 2.0. A Computer Program for Fitting Multi-Isotopomer Diatomic Molecule Spectra*, University of Waterloo Chemical Physics Research Report CP-653 (2001). The source code and manual for this program may be obtained from the "Computer Programs" link on the www site *http://leroy.uwaterloo.ca*.

[6] R. J. Le Roy, *RKR1. A Computer Program Implementing the First-Order RKR Method for Determining Diatom Potential Energy Curves from Spectroscopic Constants*, University of Waterloo Chemical Physics Research Report CP-425 (1992). The source code and manual for this program are distributed freely through the www site *http://scienide.uwaterloo.ca/~leroy*.

[7] R. J. Le Roy, *LEVEL 7.4: A Computer Program for Solving the Radial Schrödinger Equation for Bound and Quasibound Levels*, University of Waterloo Chemical Physics Research Report

CP-642R[3] (2000). The source code and manual for this program may be obtained from the "Computer Programs" link on the www site *http://leroy.uwaterloo.ca* .

[8] P. G. Hajigeorgiou and R. J. Le Roy, J. Chem. Phys. **112**, 3949 (2000).

[9] J. Y. Seto, *Direct Fitting of Analytic Potential Functions to Diatomic Molecular Spectroscopic Data*, M. Sc. Thesis, University of Waterloo (2000).

[10] J. Y. Seto and R. J. L. Roy, J. Chem. Phys. **113**, 3067 (2000).

[11] J. A. Coxon and P. G. Hajigeorgiou, J. Mol. Spectrosc. **150**, 1 (1991).

[12] R. Brühl, J. Kapetanakis, and D. Zimmermann, J. Chem. Phys. **94**, 5865 (1991).

[13] H. G. Hedderich, M. Dulick, and P. F. Bernath, J. Chem. Phys. **99**, 8363 (1993).

[14] A. Šurkus, Chem. Phys. Lett. **279**, 236 (1997).

[15] J. Y. Seto, Z. Morbi, F. Charron, S. K. Lee, P. F. Bernath, and R. J. Le Roy, J. Chem. Phys. **110**, 11756 (1999).

[16] Program DSPotFit (Diatomic Singlet Potential Fits), by R. J. Le Roy, J. Y. Seto and Y. Huang, will be available on request from *leroy@UWaterloo.ca* in the near future.

[17] E. G. Lee, J. Y. Seto, T. Hirao, P. F. Bernath, and R. J. Le Roy, J. Mol. Spectrosc. **194**, 197 (1999).

[18] J. Y. Seto, R. J. Le Roy, J. Vergès, and C. Amiot, J. Chem. Phys. **113**, 3067 (2000).

[19] J. Tellinghuisen, J. Mol. Spectrosc. **173**, 223 (1995).

[20] F. L. Pilar, *Elementary Quantum Chemistry* (McGraw-Hill Publishing Company, Hightstown, NJ, 1990).

[21] P. F. Bernath, *Spectra of Atoms and Molecules* (Oxford University Press, Oxford, 1995).

[22] R. J. Le Roy and J. van Kranendonk, J. Chem. Phys. **61**, 4750 (1974).

[23] G. Herzberg, *Spectra of Diatomic Molecules* (Van Nostrand, Toronto, 1950).

[24] J. W. Tromp and R. J. Le Roy, J. Mol. Spectrosc. **109**, 352 (1985).

[25] J. L. Dunham, Phys. Rev. **41**, 721 (1932).

[26] H. Lefebvre-Brion and R. W. Field, *Perturbations in the Spectra of Diatomic Molecules* (Academic Press, New York, 1986).

[27] D. R. T. Appadoo, P. F. Bernath, and R. J. Le Roy, Can. J. Phys. **72**, 1265 (1994).

[28] D. Rapp, *Quantum Mechanics* (Holt, Rinehart and Winston, Inc., U.S.A, 1971).

[29] J. L. Dunham, Phys. Rev. **41**, 713 (1932).

[30] P. R. Bunker and R. E. Moss, Mol. Phys. **33**, 417 (1977).

[31] J. K. G. Watson, J. Mol. Spectrosc. **80**, 411 (1980).

[32] R. J. Le Roy, J. Mol. Spectrosc. **194**, 189 (1999).

[33] A) R. Rydberg, Z. Physik **73**, 376 (1931); b) O. Klein, Z. Physik **76**, 226 (1932); c) R. Rydberg, Z. Physik **80**, 514 (1933); d) A.L.G. Rees, Proc. Phys. Soc. (London) **59**, 998 (1947).

[34] R. J. Le Roy, in *Semiclassical Methods in Molecular Scattering and Spectroscopy*, edited by M. Child (D. Reidel, Dordrecht, 1980), vol. 53 of *Series C - Mathematical and Physical Sciences*, pp. 109–126.

[35] C. Schwartz and R. J. Le Roy, J. Chem. Phys. **81**, 3996 (1984).

[36] O. Klein, Z. Physik **76**, 226 (1932).

[37] J. M. Hutson, S. Gerstenkorn, P. Luc, and J. Sinzelle, J. Mol. Spectrosc. **96**, 266 (1982).

[38] R. A. Bernheim, L. P. Gold, P. B. Kelly, C. Tomczyk, and D. K. Veirs, J. Chem. Phys. **74**, 3249 (1981).

[39] S. Antonova, G. Lazarov, K. Urbanski, A. M. Lyyra, J. Chem. Phys. **112**, 7080 (2000).

[40] W. M. Kosman and J. Hinze, J. Mol. Spectrosc. **56**, 93 (1975).

[41] C. R. Vidal and H. Scheingraber, J. Mol. Spectrosc. **65**, 46 (1977).

[42] A. Pashov, W. Jastrzębski and P. Kowalczyk, J. Chem. Phys. **113**, 6624 (2000).

[43] Ch. Lisdat, O. Dulieu, H. Knöckel and E. Tiemann, Eur. Phys. J. D **17**, 319 (2001).

[44] A. Pashov, W. Jastrzębski and P. Kowalczyk, Computer Physics Communications **128**, 622 (2000).

[45] A. Pashov, I. Jackowska, W. Jastrzębski and P. Kowalczyk, Phys. Rev. A **58**, 1048 (1998).

[46] A. Pashov, W. Jastrzębski, W. Jaśniecki, V. Bednarska and P. Kowalczyk, J. Mol. Spectrosc. **203**, 264 (2000).

[47] F. Martin, P. Crozet, A. J. Ross and M. Aubert-Frécon, P. Kowalczyk, W. Jastrzębski and A. Pashov, J. Chem. Phys. **115**, 4118 (2001).

[48] J. A. Coxon, J. Mol. Spectrosc. **117**, 361 (1986).

[49] J. A. Coxon and P. G. Hajigeorgiou, Chem. Phys. **167**, 327 (1992).

[50] M. Molski, J. Chem. Phys. **103**, 5269 (1999).

[51] J. B. White, M. Dulick, and P. F. Bernath, J. Chem. Phys. **99**, 8371 (1993).

[52] J. M. Campbell, M. Dulick, D. Klapstein, J. B. White, and P. F. Bernath, J. Chem. Phys. **99**, 8379 (1993).

[53] A. A. Šurkus, R. J. Rakauskas, and A. B. Bolotin, Chem. Phys. Lett. **105**, 291 (1984).

[54] A. Šurkus, Chem. Phys. Lett. **126**, 356 (1986).

[55] J. A. Coxon and R. Colin, J. Mol. Spectrosc. **181**, 215 (1997).

[56] J. A. Coxon and P. G. Hajigeorgiou, J. Mol. Spectrosc. **193**, 306 (1999).

[57] R. J. Le Roy and R. B. Bernstein, J. Chem. Phys. **54**, 5114 (1971).

[58] R. J. Le Roy and W.-K. Liu, J. Chem. Phys. **69**, 3622 (1978).

[59] J. N. L. Connor and A. D. Smith, Mol. Phys. **43**, 397 (1981).

[60] G. Simons, R. G. Parr, and J. M. Finlan, J. Chem. Phys. **59**, 3229 (1973).

[61] A. J. Thakkar, J. Chem. Phys. **62**, 1693 (1975), Ajit's modified Dunham/SPF-like expansion potential.

[62] J. F. Ogilvie, Proc. Roy. Soc. (London) **A 378**, 287 (1981).

[63] P. M. Morse, Phys. Rev. **54**, 57 (1929).

[64] J. A. Coxon, J. Mol. Spectrosc. **152**, 274 (1992).

[65] J. O. Hirschfelder, C. F. Curtiss, and R. B. Bird, *Molecular Theory of Gases and Liquids* (Wiley, New York, 1964), .

[66] J. O. Hirschfelder and W. J. Meath, in *Intermolecular Forces*, edited by J. O. Hirschfelder (Interscience, New York, 1967), vol. 12 of *Adv. Chem. Phys.*, pp. 3–106.

[67] J. A. Coxon and P. Hajigeorgiou, J. Mol. Spectrosc. **203**, 49 (2000).

[68] C. Tsai, R. Freeland, J. Vogels, H. Boesten, B. Verhaar, and D. Heinzen, Phys. Rev. Lett. **79**, 1245 (1997).

[69] J. Hepburn, G. Scoles, and R. Penco, Chem. Phys. Lett. **36**, 451 (1975).

[70] A. Koide, W. J. Meath, and A. R. Allnatt, Chem. Phys. **58**, 105 (1981).

[71] K. T. Tang and J. P. Toennies, J. Chem. Phys. **80**, 3726 (1984).

[72] C. Douketis, J. M. Hutson, B. J. Orr and G. Scoles, Mol. Phys. **52**, 763 (1984).

[73] J. F. Ogilvie, J. Phys. B: At. Mol. Opt. Phys. **27**, 47 (1994).

[74] J. F. Ogilvie and S. C. Liao, Chem. Phys. Lett. **226**, 281 (1994).

[75] J. A. Coxon and S. C. Foster, J. Mol. Spectrosc. **91**, 243 (1982).

[76] D. K. Watson, C. J. Cerjan, S. Guberman and A. Dalgarno, Chem. Phys. Lett. **50**, 181 (1977).

[77] H.-K. Chung, K. Kirby, and J. F. Babb, Phys. Rev. A **60**, 2002 (1999).

[78] D. D. Konowalow and J. L. Fish, Chem. Phys. **84**, 463 (1984).

[79] D. D. Konowalow and J. L. Fish, Chem. Phys. **77**, 435 (1983).

[80] I. Schmidt-Mink, W. Müller and W. Meyer, Chem. Phys. **92**, 263 (1985).

[81] R. Poteau and F. Spiegelmann, J. Mol. Spectrosc. **171**, 299 (1995).

[82] K. Wurm, Z. Physik **58**, 562 (1929).

[83] A. Harvey and F. A. Jenkins, Phys. Rev. **34**, 1286 (1929).

[84] M. M. Hessel and C. R. Vidal, J. Chem. Phys. **70**, 4439 (1979).

[85] I. Russier, A. Yiannopoulou, P. Crozet, A. J. Ross, F. Martin, and C. Linton, J. Mol. Spectrosc. **184**, 129 (1997).

[86] G. Lazarov and A. M. Lyyra, J. Mol. Spectrosc. **191**, 387 (1998).

[87] V. S. Ivanov, V. B. Sovkov, L. Li, A. M. Lyyra, G. Lazarov, and J. Huennekens, J. Mol. Spectrosc. **194**, 147 (1999).

[88] R. J. Le Roy, J. Mol. Spectrosc. **191**, 223 (1998).

[89] P. S. Bagus, C. M. Moser, P. Goethals and G. Verhaegen, J. Chem. Phys. **58**, 1886 (1973).

[90] J. Gerratt and M. Raimondi, Proc. R. Soc. Lond. **A 371**, 525 (1980).

[91] D. L. Cooper, J. Chem. Phys. **80**, 1961 (1984).

[92] C. Henriet and G. Verhaegen, J. Mol. Structure **107**, 63 (1984).

[93] M. Larsson, J. Chem. Phys. **81**, 6409 (1984).

[94] W. W. Watson, Phys. Rev. **32**, 600 (1928).

[95] P. G. Koontz, Phys. Rev. **48**, 707 (1935).

[96] W. W. Watson and R. F. Humphreys, Phys. Rev. **52**, 318 (1937).

[97] R. Horne and R. Colin, Bull. Soc. Chim. **81**, 93 (1972).

[98] D. De Greef and R. Colin, J. Mol. Spectrosc. **53**, 455 (1974).

[99] R. Colin, C. Dreze and M. Steinhauer, Can. J. Phys. **61**, 641 (1983).

[100] C. Focsa, S. Firth, P. F. Bernath and R. Colin, J. Chem. Phys. **109**, 5795 (1998).

[101] C. Focsa, P. F. Bernath, R. Mitzner and R. Colin, J. Mol. Spectrosc. **192**, 348 (1998).

[102] R. Colin and D. De Greef, Can. J. Phys. **53**, 2142 (1975).

[103] C. Clerbaux and R. Colin, Mol. Phys. **72**, 471 (1991).

[104] Y. Huang and R. J. L. Roy, *Direct-Potential-Fit Determination of an Analytical Potential for the* $F\,^1\Sigma_g^+$ *"shelf" State of* Li_2, Paper RA03 at the 55^{th} International Symposium on Molecular Spectroscopy, Ohio State University (2000).

[105] M. Abramowitz and I. A. Stegun, *Handbook of Mathematical Functions* (Dover Publications, Inc., New York, 1970).

[106] M. G. Barwell, R. J. Le Roy, P. Pajunen, and M. S. Child, J. Chem. Phys. **71**, 2618 (1979).

[107] P. Pajunen, J. Chem. Phys. **73**, 6232 (1980).

[108] J. Luppi and P. Pajunen, J. Chem. Phys. **77**, 1505 (1982).